SANDIA REPORT

SAND2004-6005
Unlimited Release
Printed February 2005

Uniaxial and Triaxial Compression Tests of Silicon Carbide Ceramics under Quasi-static Loading Condition

Moo Y. Lee, Rebecca M. Brannon and David R. Bronowski

Prepared by
Sandia National Laboratories
Albuquerque, New Mexico 87185

Sandia is a multiprogram laboratory operated by Sandia Corporation,
a Lockheed Martin Company, for the United States Department of Energy's
National Nuclear Security Administration under Contract DE-AC04-94AL85000.

Issued by Sandia National Laboratories, operated for the United States Department of Energy by Sandia Corporation.

Available to DOE and DOE contractors from
U.S. Department of Energy
Office of Scientific and Technical Information
P.O. Box 62
Oak Ridge, TN 37831

Telephone: (865) 576-8401
Facsimile: (865) 576-5728
E-Mail: reports@adonis.osti.gov
Online ordering: http://www.doe.gov/bridge

Available to the public from
U.S. Department of Commerce
National Technical Information Service
5285 Port Royal Rd.
Springfield, VA 22161

Telephone: (800) 553-6847
Facsimile: (703) 605-6900
E-Mail: orders@ntis.fedworld.gov
Online order: http://www.ntis.gov/help/ordermethods.asp?loc=7-4-0#online

SAND 2004-6005
Unlimited Release
Printed February 2005

Uniaxial and Triaxial Compression Tests of Silicon Carbide Ceramics under Quasi-static Loading Condition

Moo Y. Lee, Rebecca M. Brannon, and David R. Bronowski

Geomechanics Department
Sandia National Laboratories
P.O. Box 5800
Albuquerque, NM 87185-0751

ABSTRACT

To establish mechanical properties and failure criteria of silicon carbide (SiC-N) ceramics, a series of quasi-static compression tests has been completed using a high-pressure vessel and a unique sample alignment jig. This report summarizes the test methods, set-up, relevant observations, and results from the constitutive experimental efforts. Results from the uniaxial and triaxial compression tests established the failure threshold for the SiC-N ceramics in terms of stress invariants (I_1 and J_2) over the range $1246<I_1<2405$. In this range, results are fitted to the following limit function (Fossum and Brannon, 2004), $\sqrt{J_2}(MPa) = a_1 - a_3 e^{-a_2 \frac{I_1}{3}} + a_4 \frac{I_1}{3}$, where a_1=10181 MPa, $a_2=4.2\times10^{-4}$, a_3=11372 MPa, and a_4=1.046. Combining these quasistatic triaxial compression strength measurements with existing data at higher pressures naturally results in different values for the least-squares fit to this function, appropriate over a broader pressure range. These triaxial compression tests are significant because they constitute the first successful measurements of SiC-N compressive strength under quasistatic conditions. Having an unconfined compressive strength of ~3800 MPa, SiC-N has been heretofore tested only under dynamic conditions to achieve a sufficiently large load to induce failure. Obtaining reliable quasi-static strength measurements has required design of a special alignment jig and load-spreader assembly, as well as redundant gages to ensure alignment. When considered in combination with existing dynamic strength measurements, these data significantly advance the characterization of pressure-dependence of strength, which is important for penetration simulations where failed regions are often at lower pressures than intact regions.

ACKNOWLEDGEMENTS

Funding for this work under the Program Executive Office-Ground Combat Systems (PM-Combat Systems, Mr. John Rowe) is gratefully acknowledged. The authors appreciate the support of M. Normandia of the U.S. Army Research Laboratory and T. Holmquist of the Army High Performance Computing Research Center for providing us valuable information on the properties of SiC-N ceramics. Diane Meier assisted in data mining to identify existing published properties for the silicon carbide material. The authors also thank Larry Costin for his managerial support.

Table of Contents

Figures

Table

1. Introduction

Sandia is currently working to enhance the ALEGRA (Arbitrary Lagrangian Eulerian General Research Application) code (Budge and Peery, 1993; Summers *et al.*, 1997, Wong *et al.*, 2001) to simulate the mechanical and thermomechanical responses of Silicon Carbide (SiC) for applications in the area of hypervelocity penetration of metal clad armor. Concurrent with constitutive model development, laboratory experiments have been conducted under quasi-static conditions to provide the experimental data needed to parameterize the models to be used in ALEGRA as well as to give insight into the failure phenomena under different loading conditions.

This report describes the experimental characterization of the mechanical properties of SiC-N ceramics manufactured by CERCOM, Inc. SiC-N is an improved grade of SiC-B with higher flexural strength and fracture toughness (Appendix D). Both grades are so-called "PAD" (Pressure Assisted Densified) Silicon Carbide (Cercom, 2003) produced by hot pressing powders with an organic binder (Dandekar and Bartkowski, 2001). A proprietary milling process is used to achieve a high homogeneity in grain size distributions. Figures 1 and 2 show SEM (Scanning Electron Microscope) pictures of a SiC-N specimen prepared for testing. The grain size varies from 1 to 8 μm with an average value of 4 μm (Bartkowski and Spletzer, 2001). The pore spaces (dark areas) have an average dimension of approximately 2 μm.

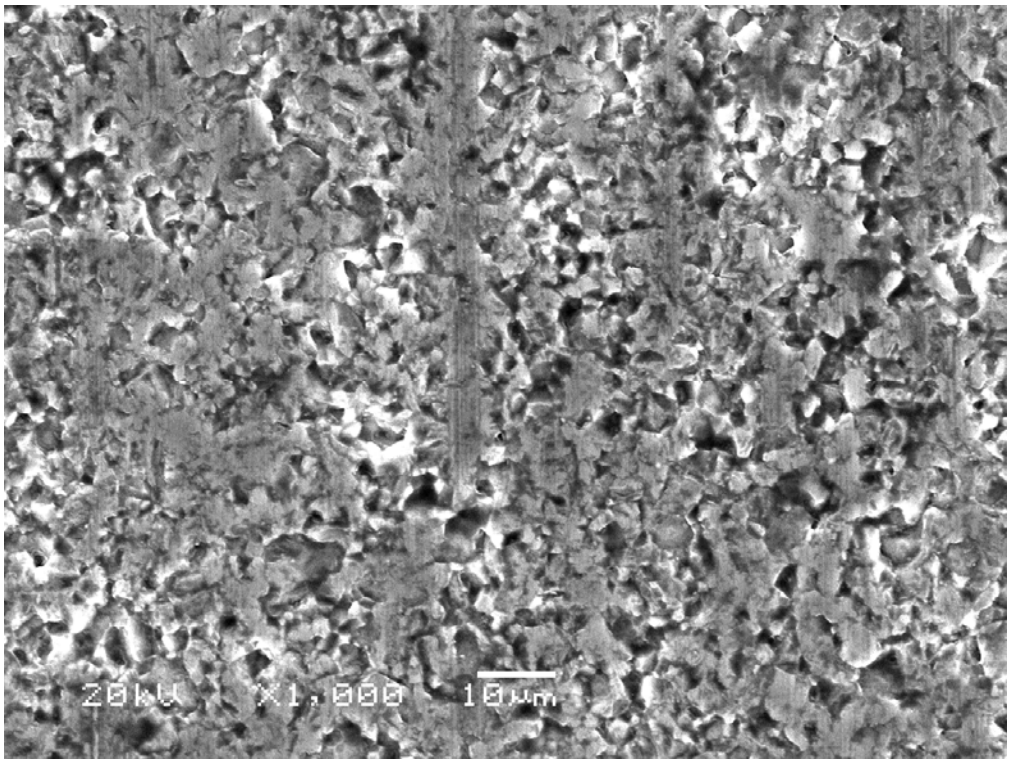

Figure 1. SEM micrograph of the surface of a SiC-N specimen prepared for mechanical testing. Grain and pore sizes are distributed uniformly. Also shown are the shaded grooves created from surface grinding of the specimen (Micrograph by S. J. Glass).

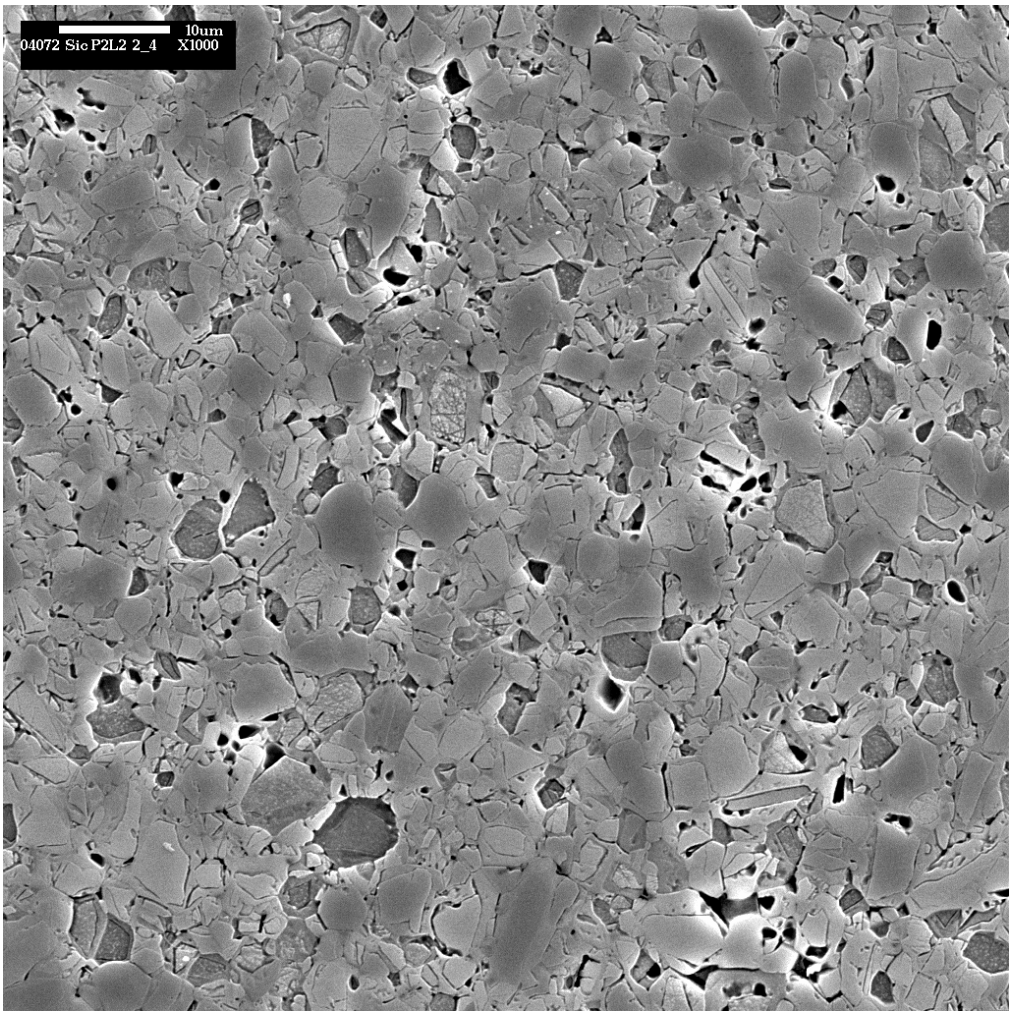

Figure 2. SEM micrograph of the polished and etched surface of a SiC-N specimen revealing grain boundaries and pore spaces (Micrograph by S. J. Glass).

The objective of this experimental study was to obtain the mechanical calibration properties of the SiC-N ceramics under quasi-static compressive loading conditions so that the constitutive model and host code could be validated under different loading conditions. The experimental program consists of uniaxial compression and triaxial compression tests of the SiC-N ceramics. The uniaxial compression tests have been conducted up to a failure stress to provide the unconfined uniaxial compressive strength and elastic constants, Young's modulus E and Poisson's ratio ν. The triaxial compression tests determine the low pressure part of the shear failure envelope represented in terms of stress invariants.

2. Sample Preparation

The SiC-N specimens were obtained from the manufacturer (CERCOM Inc.) in the form of right circular cylinders. The specified dimensions required for mechanical testing were 12.70 (±0.025) mm in diameter and 25.40 (±0.025) mm in length. The dimensions fall within the range of suggested length-to-diameter ratio (2 to 2.5) recommended for uniaxial or triaxial compression tests (eg. ASTM D4543 "Standard Practice for Preparing Rock Core Specimens and Determining Dimensional and Shape Tolerances"). The ends of the specimen were ground flat to be parallel each other within 0.0025 mm tolerance.

Before testing, randomly selected specimens were visually inspected under SEM for any significant surface flaws of the specimen. Figure 3 shows SEM micrographs of a typical SiC-N specimen. The condition of the edge of the cylindrical specimen is shown in two different magnifications (×40 and ×1000). Two pairs of strain gage rosettes, consisting of axial, lateral, and oblique strain gages, were mounted on opposite sides of the specimen (180° apart) at mid-height of the specimen. For each rosette, the axial strain gage (oriented in parallel with the long axis of the specimen) and the lateral strain gage (perpendicular to the axial gage) were used to measure axial (ε_a) and lateral (ε_l) strains, respectively.

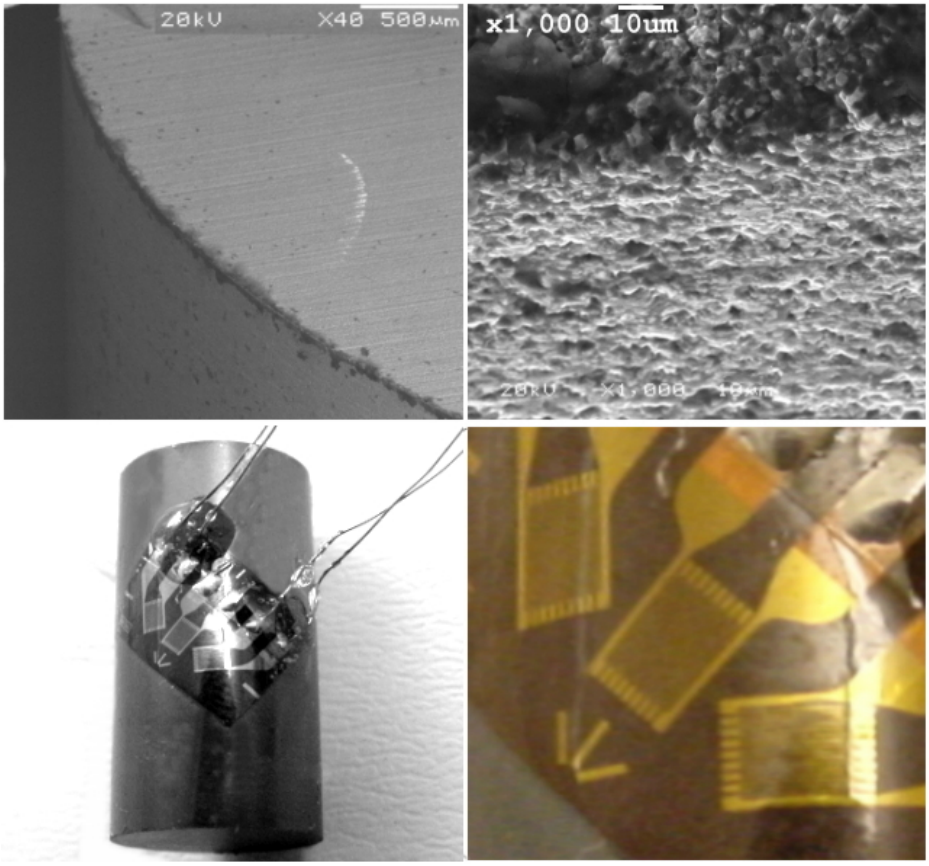

Figure 3. A SiC-N specimen prepared in the form of a right circular cylinder. Two SEM micrographs (×40-left and ×1000-right) show the magnified edge of the cylinder using SEM. The strain rosettes measure axial and lateral strains (Micrographs by S. J. Glass).

3. Experimental Set-up

Because of the extremely high mean strength (~5GPa) and the high Young's modulus (~460 GPa) of the SiC-N ceramics (see Appendix D), precise alignment of the specimen with respect to the loading axis is critical in achieving uniform loading conditions to the specimen. Any minor deviations in parallelism in the pistons of a test vessel, end-caps (or load-spreaders), and end surfaces of the specimen contribute to premature failures of the specimen or the loading apparatus. Figure 4 shows two examples of explosive failures of the Tungsten Carbide (WC) end-caps before the axial stress, σ_a, reached the compressive strengths of the end-caps (6 GPa) or the SiC-N specimens.

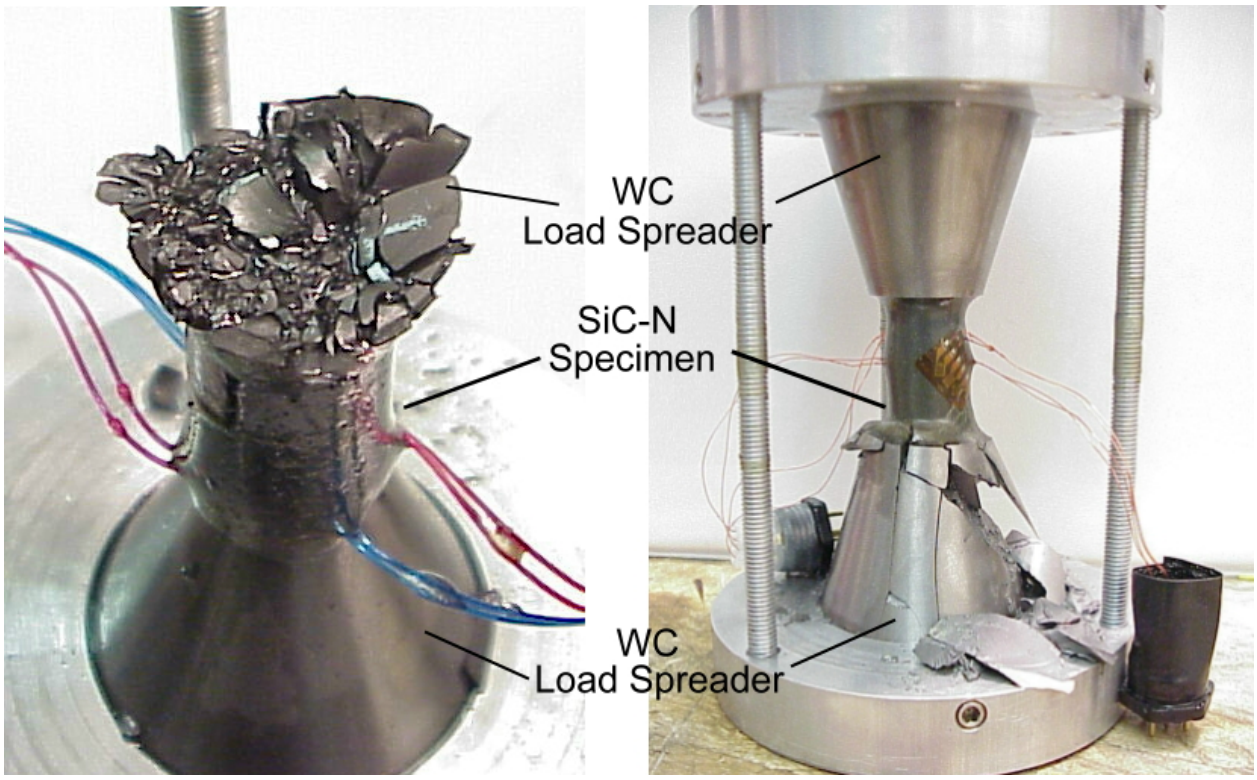

(a) **(b)**

Figure 4. Premature failures of the Tungsten Carbide (WC) end-caps used as load spreaders before the failure of SiC-N specimens. (a) SiCN-TA03 specimen under the confining pressure, P=200 MPa and the axial stress, σ_a =2.3 GPa. (b) SiCN-TA08 specimen under the confining pressure, P=100 MPa and the axial stress σ_a =3.5 GPa.

To minimize nonuniform loading applied to the specimens and also to the end-caps, a sample alignment jig was designed and fabricated (Figure 5). It consists of a pair of centering rings, WC end-caps, and guided threaded rods connecting centering rings coaxially. The specimen was placed between the upper and the lower end-caps. The threaded rods were holding the specimen under compression between two end-caps. To reduce the stresses applied to the pistons (or push-rods) of the test vessel, the end-caps were designed in the shape of truncated right cone. The

smaller ends of the cone, in contact with the specimen, have the same diameter (12.70 ± 0.025 mm) as the SiC-N specimen. The other end of the cone has the larger diameter (38.10 ± 0.025) mm. The larger contact area with the piston reduces the stresses applied to the pistons below the yield strength of the weaker piston material. The setscrews in the centering rings adjust the minor misalignment between the specimen and the end-caps. After the specimen was secured between the tungsten carbide end-caps, an approximately 1 mm thick impervious polyurethane membrane was coated on the specimen assembly (see Figure 5). The flexible membrane allows the confining pressure to be applied hydrostatically on the specimen and at the same time prevents the confining fluid from infiltrating into pore spaces of the specimen. To maintain uniform thickness of the membrane during curing, the alignment jig with the specimen was turned on a lathe along the axial centerline of the assembly.

After the flexible membrane was cured the instrumented specimen assembly was placed in the triaxial test vessel capable of operating at confining pressures up to 400 MPa. The pressure vessel is also equipped with 12 coaxial feed-through connectors for transmitting data from the strain gages to the external data acquisition system. The inside diameter of the circular centering ring matches the outside diameter of the test vessel piston assuring a coaxial alignment of the sample jig to the axis of the loading pistons. To provide uniform contact forces to the end-caps, a thin copper (or aluminum) shim disk (0.2 mm in thickness) is inserted between the piston and the tungsten carbide end-cap. Figure 5 shows a schematic of the sample alignment jig and the gaged SiC-N specimen mounted in the triaxial pressure vessel.

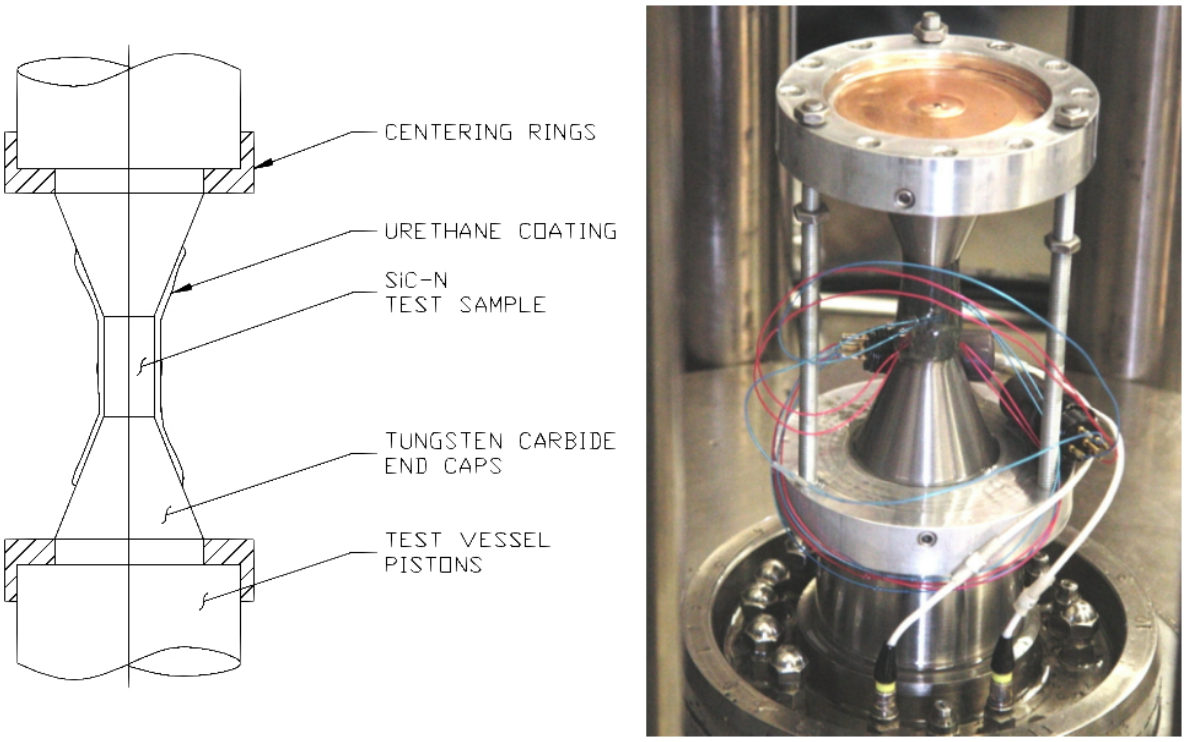

Figure 5. Sample alignment jig designed for coaxial alignment of different components of the test set-up. The strain gaged SiC-N specimen coated with flexible polyurethane membrane is also shown. The strain gage signal was transmitted to the data acquisition system through the high-pressure coaxial feed-through connectors.

The hydraulic pressure was applied to each predetermined level of confining pressure, P, at a rate of 0.5 MPa/s. The servo-controller maintained the pressure level ($\sigma_1=\sigma_2=\sigma_3=P$; where σ_1, σ_2, and σ_3 are the maximum, intermediate and minimum principal stresses, respectively). After the confining pressure was stabilized, the specimen was axially loaded using the 4.5 MN servo-controlled loading machine (Figure 6). The axial compression of the specimen was carried out at a strain rate of $\sim 2 \times 10^{-5}$ /s.

The confining pressure was measured with the pressure transducer connected to the triaxial pressure vessel and axial and lateral strains were measured with the strain gage rosettes mounted on the specimen (see Figure 3). Eight channels of data including time, confining pressure, axial load, axial stroke of the piston, two axial strains and two lateral strains from the strain rosettes, were recorded using DATAVG, an event-triggered data acquisition program (Hardy, 1993).

Figure 6. Compression test set-up with 4.5 MN load-frame and 400 MPa pressure vessel.

4. Uniaxial Compression Test of SiC-N Ceramics

Unconfined uniaxial compression tests have been conducted on three SiC-N specimens (all other tests employed lateral confining pressure). The experimental apparatus used for the compression tests meets or exceeds the requirements of ASTM D2938 ("Standard Test Method for Unconfined Compressive Strength of Intact Rock Core Specimens"). Specimens were loaded at a constant axial strain rate of 2×10^{-5} /s until the peak stress was reached and the specimen failed in an explosive manner. Figure 7 shows a typical stress-strain plot obtained from an unconfined uniaxial compression test. The axial stress (σ_a) is plotted against axial (ε_a) and lateral (ε_l) strains, respectively. The volumetric strain, calculated as ($\varepsilon_v = \varepsilon_a + 2\varepsilon_l$), is also shown in the plot. The unconfined uniaxial compressive strength of the SiC-N ceramics was calculated from:

$$C_0=P_u/\pi r^2$$

where C_0 is the unconfined uniaxial compressive strength in MPa; P_u is the peak load in N; and r is the radius of the specimen in mm.

The unconfined compressive strength of the SiC-N specimens using the above equation was 3,872 ± 126 MPa. This strength, obtained under quasi-static loading, is significantly smaller than the dynamic strength of the SiC-N specimens (~6,500 MPa at ~10^3/s strain rate) reported by Wang and Ramesh (2004), illustrating rate dependence of impulsive fracture stress for brittle materials (Grady and Lipkin, 1980). The strength increase for the smaller samples used by Wang and Ramesh may be attributed additionally to a Weibull-like dependence of strength on sample volume (by being more likely to contain critically large or favorably oriented flaws, large samples are weaker, on average, than small samples).

Results from the uniaxial compression tests of SiC-N specimens are summarized in Table 1. Stress-strain plots from all three tests are given in Appendix A. The specimen responds with remarkably *linear* elasticity until failure, with no evidence of hardening or progressive softening. The peak stress in each plot is the strength of the specimen.

The linear-elastic response of the specimen can also be seen from the unloading-reloading cycle in Figures 7 and 8. At about 880 MPa of axial stress in the specimen, the stress was reduced to 220 MPa and reloaded again. Since the response of the SiC-N specimen to the unloading-reloading cycle is close to perfect linear-elastic behavior, the unloading and reloading loop is barely discernable from the initial loading curves shown in Figures 7 and 8.

Figure 9 shows high-speed photographs of the SiCN-UC02 specimen subjected to uniaxial unconfined compressive loading. To observe brittle fragmentation, we used a high-speed camera that can capture images at the rate of 27,000 frames/s. The resulting time interval between the neighboring frames was approximately 37 μs. As shown in the first frame, both ends of the specimen, making contact with the load-spreaders, were chipped prematurely. This was caused probably by a stress concentration at the contact surface due to the mismatch of the material properties of the SiC-N specimen and the WC end-caps. The second frame shows a development of axially oriented micro-cracks and their coalescence through the inclined shear micro-cracks.

The peak stress (σ_1=3988 MPa) was reached about 37 μs later and the specimen explodes into small powder-like fragments. The third and the fourth frames show emission of visible light coming out of the specimen. It appears that the emission of the light resembles the phenomenon of triboluminescence that converts the mechanical shock energy into light.

The failure mode and the processes observed in the quasi-static uniaxial compression tests were similar to the ones obtained from the dynamic stress condition using the Kolsky bar (Wang and Ramesh, 2004). Regardless of the difference in strain rates (~2×10^{-5}/s vs. ~10^{3}/s) used for testing, the common mode of failure can be described as the coalescence of longitudinal cracks before the axial splitting of the specimens.

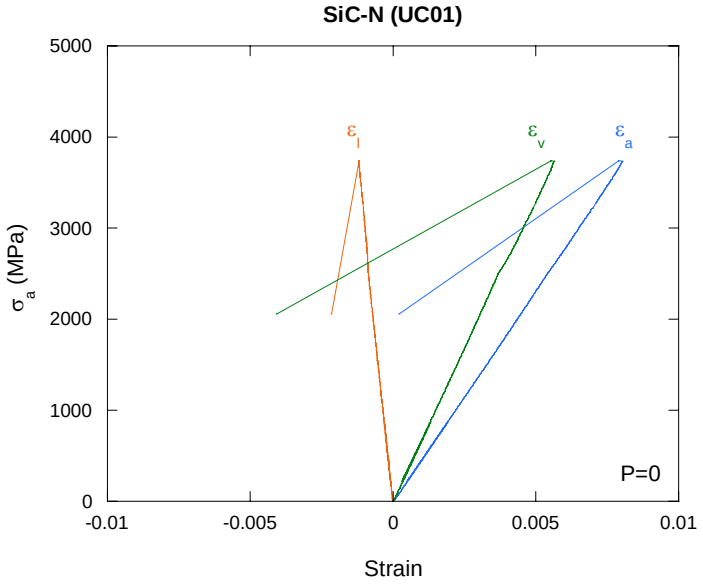

Figure 7. Stress-strain plot for the uniaxial compression test of specimen SiCN-UC01. ε_a, ε_l, and ε_v are axial, lateral, and volumetric strains, respectively. P is the confining pressure.

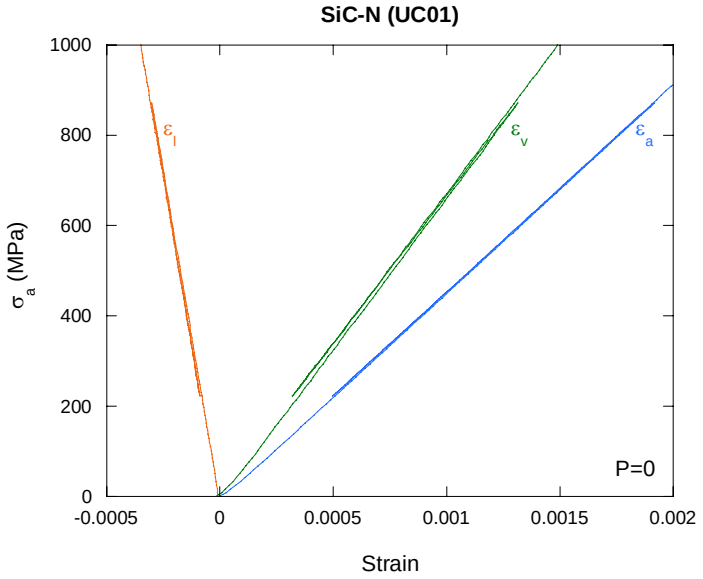

Figure 8. Zoomed-in unloading-reloading cycle for the uniaxial compression test of specimen SiCN-UC01 shown in Figure 7. ε_a, ε_l, and ε_v are axial, lateral, and volumetric strains, respectively. P is the confining pressure.

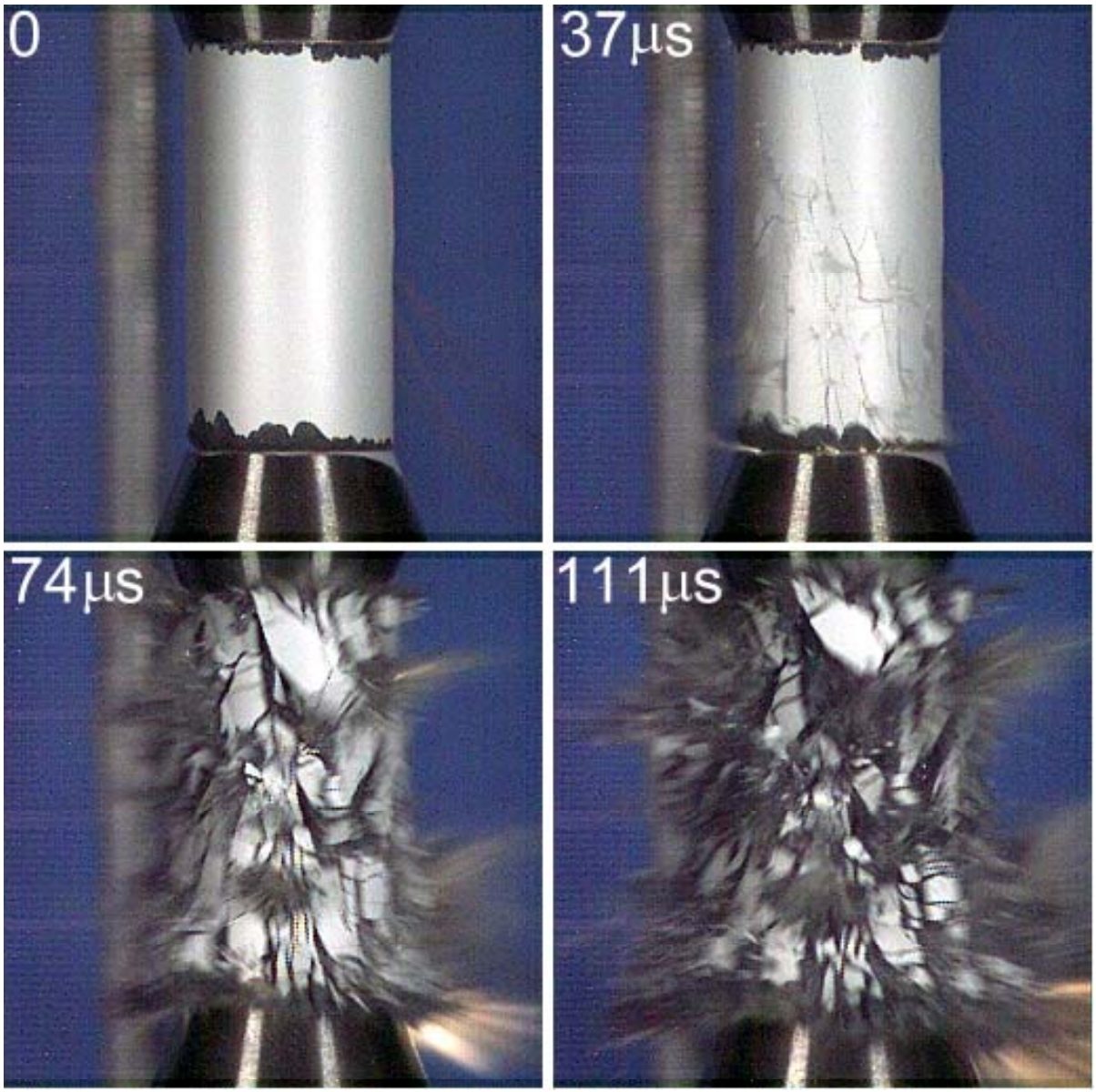

Figure 9. Explosive failure of the SICN-UC02 specimen (12.7 mm in diameter and 25.4 mm in length) subjected to the unconfined uniaxial compressive stress condition (σ_1=3988 MPa at failure and σ_2= σ_3=0).

Table 1. Summary of uniaxial and triaxial compression tests for SiC-N specimens.

Specimen no.	Diameter (mm)	Length (mm)	P (MPa)	σ_f (MPa)	E (GPa)	ν	I_1 (MPa)	$\frac{I_1}{3}$ (MPa)	$\sqrt{J_2}$ (MPa)
SiCN-UC01	12.7	25.4	0	3738	464	0.156	3738	1246	2158
SiCN-UC02	12.7	25.4	0	3988	463	0.153	3988	1329	2302
SiCN-UC03	12.7	25.4	0	3890	467	0.154	3890	1297	2246
SiCN-TA01*	12.7	25.4	200	6326	NA	NA	6726	2242	3537
SiCN-TA02	12.7	25.4	350	5948	466	0.161	6648	2216	3232
SiCN-TA03**	12.7	25.4	200	NA**	442***	NA	NA**	NA**	NA**
SiCN-TA04	12.7	25.4	100	5508	480	0.167	5708	1903	3122
SiCN-TA05	12.7	25.4	200	6120	480	0.169	6520	2173	3418
SiCN-TA06	12.7	25.4	350	6422	484	0.172	7122	2374	3506
SiCN-TA07	12.7	25.4	350	6514	482	0.173	7214	2405	3559
SiCN-TA08**	12.7	25.4	100	NA**	474***	0.159***	NA**	NA**	NA**
SiCN-TA09	12.7	25.4	100	5283	478	0.166	5483	1828	2992

P ($=\sigma_2=\sigma_3$) = lateral confining pressure

σ_f = failure stress (maximum σ_1)

E = Young's modulus

ν = Poisson's ratio

$I_1 = \sigma_1+\sigma_2+\sigma_3$ at failure $= \sigma_f+2P$

$\frac{I_1}{3}$ = mean stress

$$\sqrt{J_2} = \frac{\sigma_f - P}{\sqrt{3}}$$

* - Strains were not measured.

** - Premature failure of the tungsten carbide end-caps at 2284 MPa for SiCN-TA03 and 3477 MPa for SiCN-TA08

*** - Uncertain value due to premature failure of the WC end-caps

5. Mechanical properties of SiC-N ceramics

Young's modulus, E, is the proportionality constant between stress and strain in the elastic portion of the uniaxial compression test:

$$E = |\sigma_a / \varepsilon_a|$$

where σ_a is the axial stress and ε_a is the axial strain. Young's modulus was determined using least squares linear regression. Figure 10 shows linear segments of the stress-stain plots and the fitted straight lines of all three uniaxial compression tests (SiCN-UC01, 02, and 03). The average value of the Young's modulus was E=465 ± 2 GPa. Table 1 also shows the effect of a confining pressure on E. As the confining pressure was increased, Young's modulus also increased. The rate of increase in E was about 14 GPa per 100 MPa increase in the confining pressure up to 100 MPa. This rate was reduced to about 1.6 GPa over the range of the confining pressure, 100 MPa <P<350 MPa. The results are summarized in Table 1 and all three plots used for the determination of E are listed in Appendix B, independently.

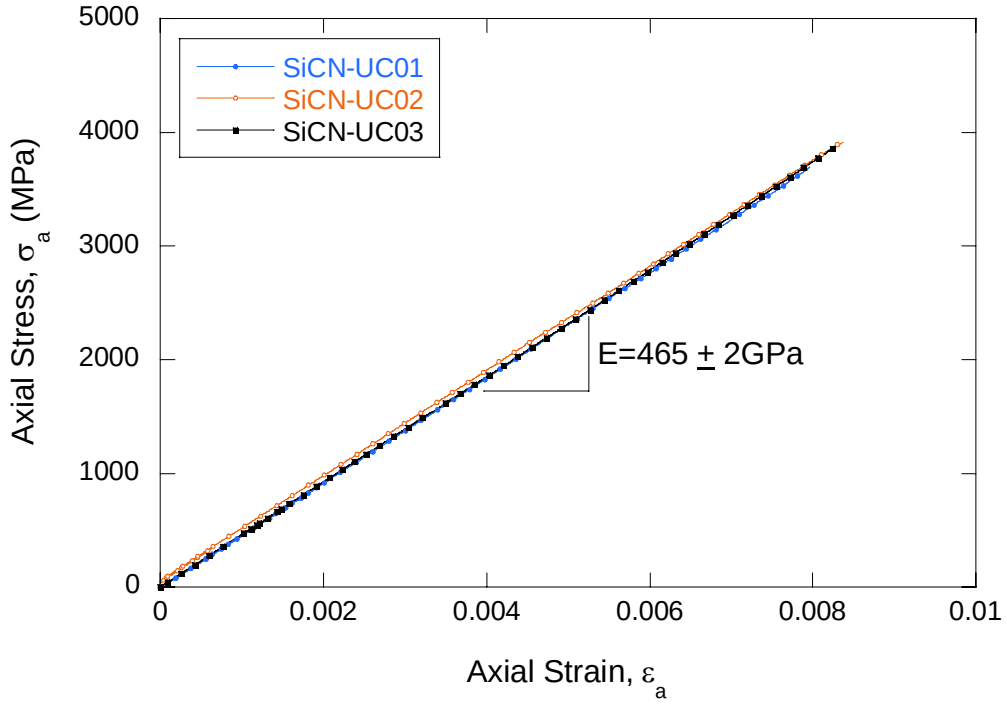

Figure 10. Linear segments of the axial stress (σ_a) - axial strain (ε_a) plot obtained during the unconfined compression tests for the SiC-N specimens. The Young's modulus, E, was obtained as the slope of the best-fit straight line.

Poisson's ratio, ν, was obtained from the ε_a-ε_l plot of each test. The linear elastic segment of the stress-strain plot was isolated and the lateral strain is plotted against the axial stress within the isolated range. The slope of the best-fit line was obtained to represent ν.

$$\nu = |\varepsilon_l \ / \ \varepsilon_a|$$

Figure 11 shows the linear-elastic segments of the ε_a-ε_l plot for the SiC-N specimens obtained from all three uniaxial compression tests (SiCN-UC01, 02, and 03) used previously for the determination of E. The average slope from all three tests is considered as a representative value of the Poisson's ratio, $\nu=0.15 \pm 0.002$. The ε_a-ε_l plot and the fitted straight line for all uniaxial compression tests are given in Appendix C. The determined Poisson's ratios from all three uniaxial compression tests of the SiC-N specimens are summarized in Table 1.

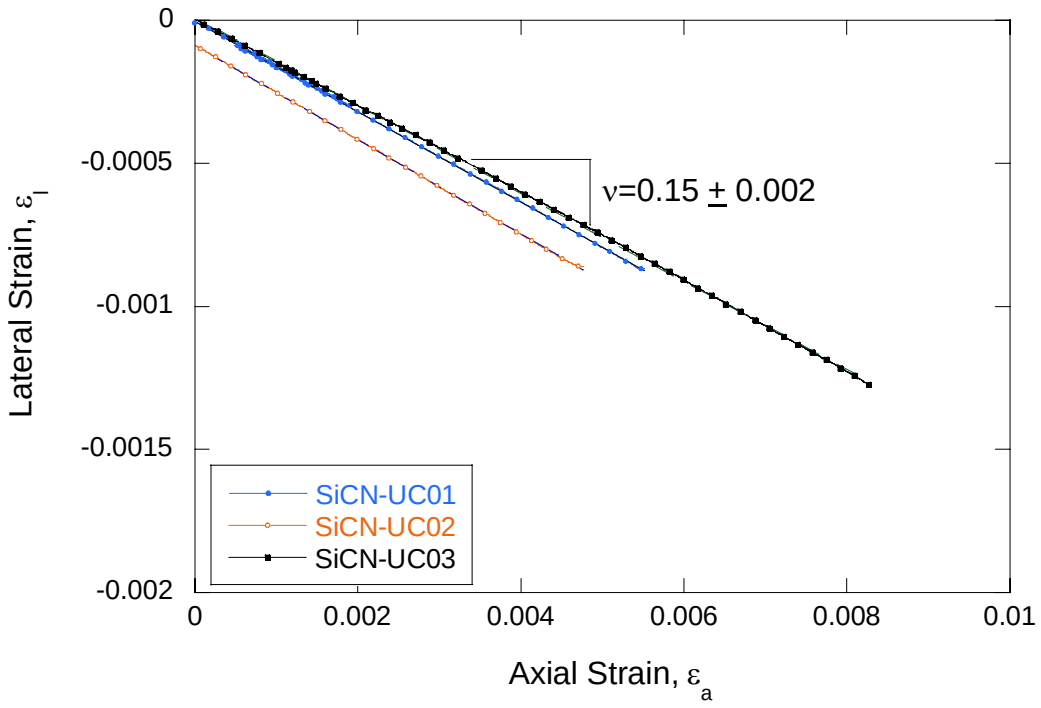

Figure 11. Linear segments of the lateral strain (ε_l)-axial strain (ε_a) plot obtained during the unconfined compression tests for the SiC-N specimens. The Poisson's ratio, ν, is obtained as the absolute value of the slope for the best-fit straight line.

6. Triaxial Compression Test of SiC-N ceramics

Triaxial compression experiments have been conducted on nine SiC-N specimens. The specimens were loaded until peak load was reached at failure. The compressive strength of the specimen subjected to a triaxial loading condition (σ_1 $\sigma_2=\sigma_3$) was calculated based on the same equation used for obtaining the uniaxial compressive strength of the SiC-N ceramics (see Chapter 4).

A typical stress-strain plot obtained during the triaxial compression test of the SiCN-TA07 specimen subjected to 350 MPa confining pressure is shown in Figure 12. Typically, the stress-strain plot for a SiC-N specimen is composed of three segments. The first segment is the hydrostatic compression of the specimen up to the predetermined confining pressure, P (=350 MPa in Figure 12). The next segment is the triaxial linear-elastic response, maintained until the peak stress is achieved. The last short segment is the sudden failure of the specimen accompanied by precursory acoustic emission from the propagating fractures in the specimen. The volumetric strain ($\varepsilon_v = \varepsilon_a + 2\varepsilon_l$) is shown in each plot. The results from the triaxial compression tests of SiC-N specimens are summarized in Table 1. Stress-strain plots from all nine tests are given in Appendix D.

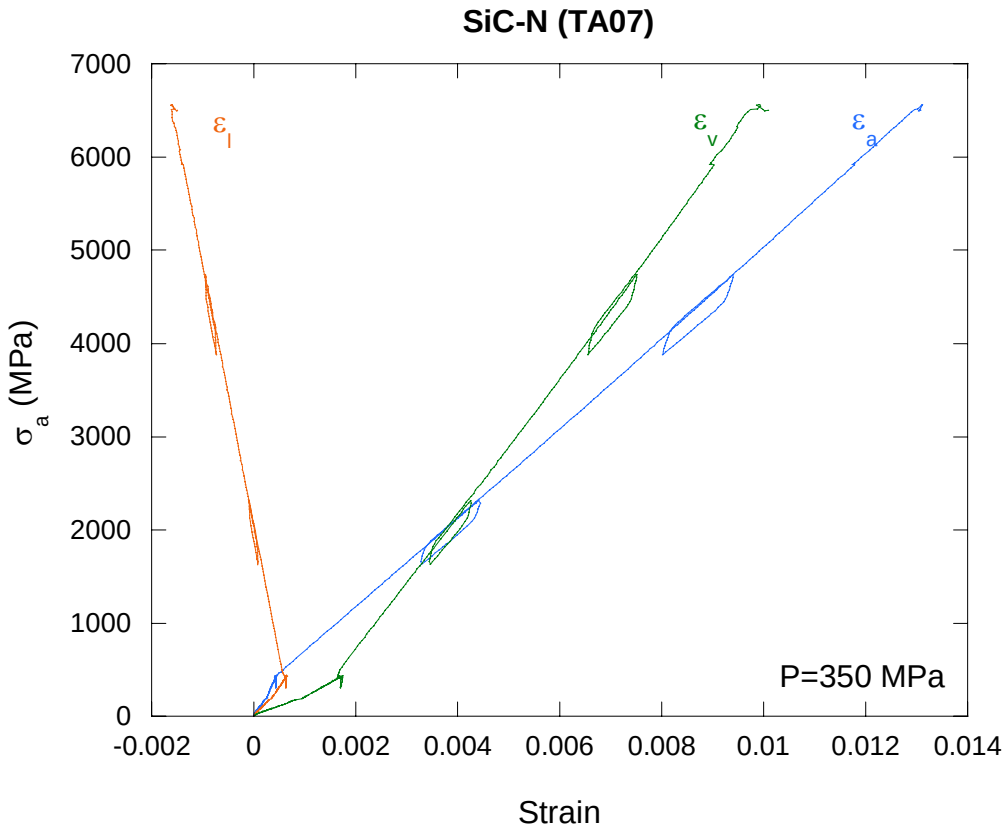

Figure 12. Stress-strain plot obtained during a triaxial compression test of specimen SiCN-TA07 subjected to the confining pressure of P=350 MPa. The axial stress (σ_a) is plotted against axial (ε_a), lateral (ε_l), and volumetric (ε_v) strains, respectively. The volumetric strain was calculated from the axial and lateral strains ($\varepsilon_v = \varepsilon_a + 2\varepsilon_l$). Also shown are the unloading and reloading loops.

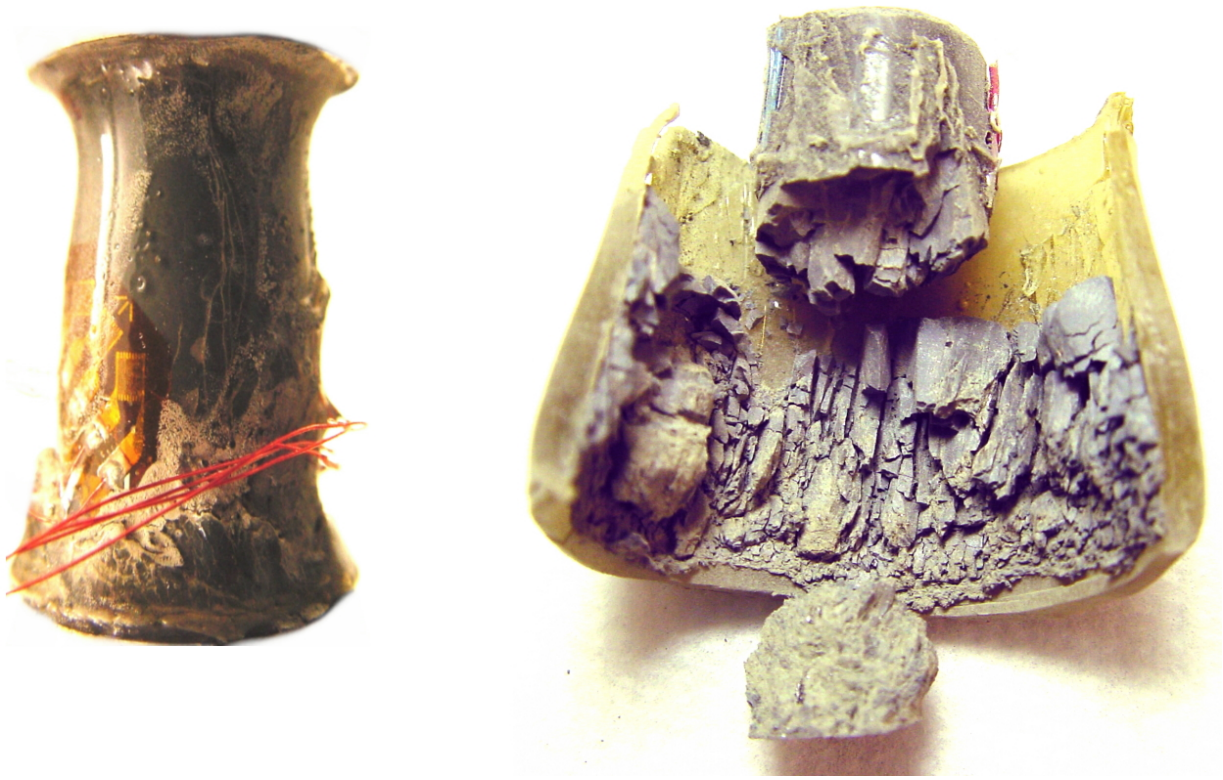

(a) **(b)**

Figure 13. Failed SiC-N specimens subjected to triaxial compressive loading. (a) SiCN-TA07 specimen subjected to the confining pressure of P=350 MPa and the axial stress of σ_a=6514 MPa (b) Unwrapped SiCN-TA01 specimen subjected to the confining pressure of P=200 MPa and the axial stress of σ_a =6326 MPa.

Figure 13 shows typical fracture networks found in the failed SiC-N specimens under the triaxial stress condition. The fractures are oriented predominantly in axial direction. However, the network of axial fractures connected each other through shear fractures between them leaving two semi-conical intact pieces shown in Figure 13 (b).

Figure 14 shows an SEM micrograph of the failed SiCN-TA04 specimen under the triaxial stress condition (σ_1=5508 MPa at failure and P=σ_2= σ_3=100 MPa). This picture is taken in a polished plane parallel to the circular end face of the specimen. It appears that micro-cracks are branched and coalesced with each other. Along the open micro-cracks, we can observe the disintegrated grains due to stress relief. Accumulation and coalescence of the micro-cracks and disintegration of the grains led to the macroscopic failure of the specimen recorded as peak stresses shown in Appendix D.

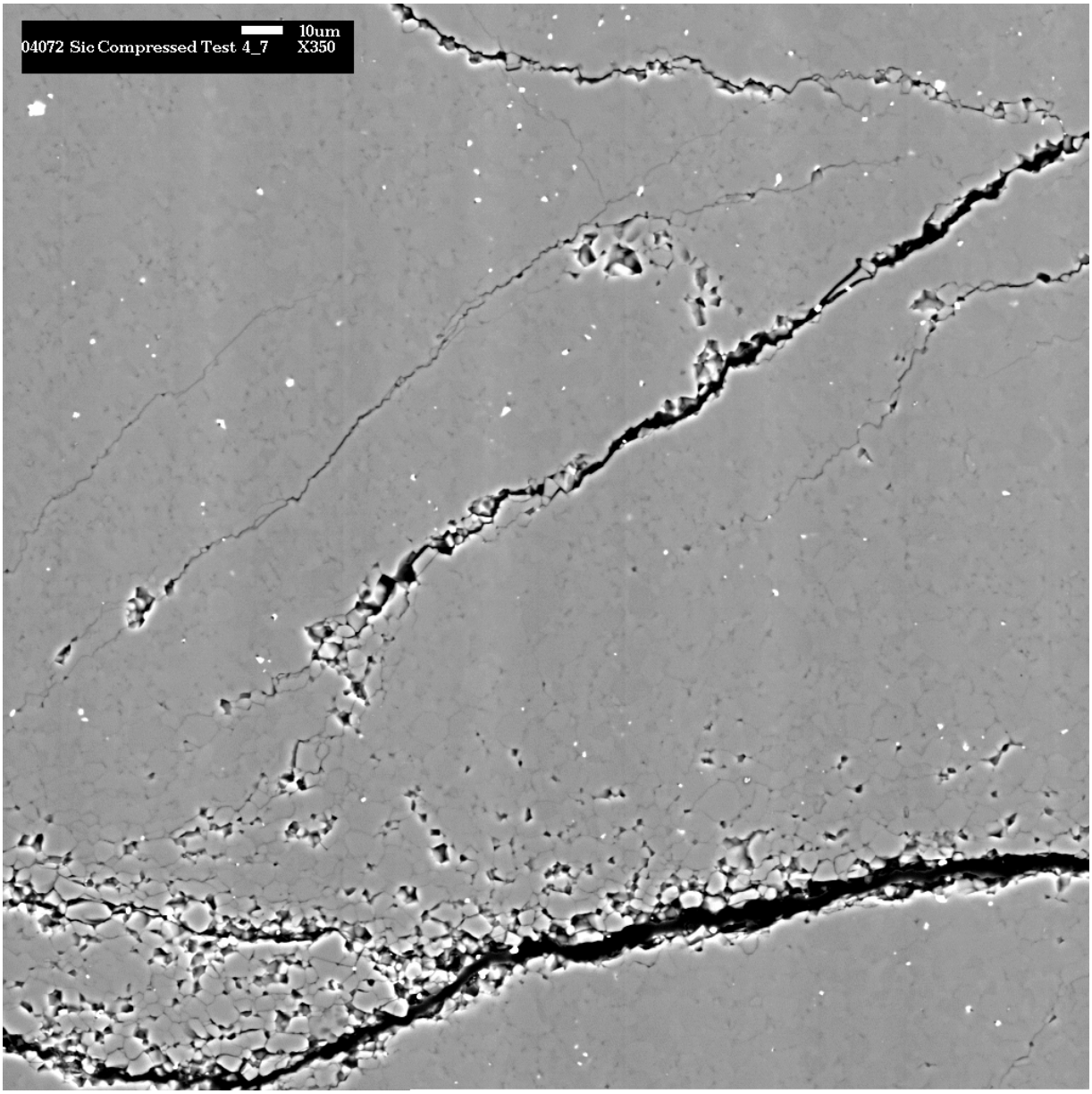

Figure 14. The SEM micrograph of the failed SiCN-TA04 specimen under the triaxial stress condition (σ_1=5508 MPa at failure and P=σ_2= σ_3=100 MPa).

7. Shear Failure Criteria of SiC-N Ceramics

For rocks and rock-like materials (e.g. concrete) having non-negligible porosity, variation of shear stresses at failure with respect to mean stresses can be described using a cap model (Sandler and Rubin, 1979 and Fossum *et al*., 1995). For ceramics like SiC, having porosity less than 0.2%, the cap feature in such models is unnecessary, but the limit function (Fossum and Brannon, 2004) that describes the peak attainable stresses in terms of all three stress invariants seems appropriate. Triaxial testing determines the part of the limit surface corresponding to a fixed Lode angle of 30 °. Thus, at this fixed Lode angle, the shear strength may be expressed as a function of the first stress invariant (trace of the stress, I_1).

In triaxial compression tests, the axial stress is the major principal stress, σ_1, and the confining pressure, P, is simultaneously the intermediate and minimum principal stress, σ_2 and σ_3. In this case, the first stress invariant, I_1, and the square root of the deviator invariant, J_2, at failure ($\sigma_1=\sigma_f$) are

$$I_1 = \sigma_1 + \sigma_2 + \sigma_3 = \sigma_f + 2P$$

$$\sqrt{J_2} = \sqrt{\frac{(\sigma_1-\sigma_2)^2 + (\sigma_2-\sigma_3)^2 + (\sigma_3-\sigma_1)^2}{6}} = \frac{\sigma_f - P}{\sqrt{3}}$$

Values of I_1, mean stress $I_1/3$, and $\sqrt{J_2}$ for different confining pressures are listed in Table 1. During the shear failure of the specimens, the state of stress can be represented as a shear failure criterion represented empirically by the following limit function (Fossum and Brannon, 2004; modified after Sandler and Rubin, 1979 and Fossum *et al*., 1995).

$$\sqrt{J_2} = a_1 - a_3 e^{-a_2 I_1} + a_4 I_1$$

where the a_k are empirical parameters to be determined for the SiC-N ceramic from uniaxial and triaxial compression tests at different mean stresses.

We used a nonlinear regression analysis to determine the unknown parameters, which minimized the sum of the squares of errors between the model-predicted values and the observed $\sqrt{J_2}$ values for different $I_1/3$ values (Figure 15). For the SiC-N ceramics the shear failure criterion is best represented *within the range of pressures for the triaxial testing* as follows:

$$\sqrt{J_2} = 10181 - 11372 \cdot e^{-0.00042\frac{I_1}{3}} + 1.046\frac{I_1}{3}$$

Figure 16 shows an expansion of the quasi-static failure criterion by including the plate-impact test data (Vogler *et al*, 2004) on the SiC-N specimens. The best-fit shear failure surface for the SiC-N ceramic specimens can be represented as follows:

$$\sqrt{J_2} = 3477 - 6294 \cdot e^{-0.0011\frac{I_1}{3}} + 0.21\frac{I_1}{3}$$

As the mean stress ($I_1/3$) increases, the value of $\sqrt{J_2}$ at failure increases rapidly in the region of quasi-static strain rate. However, the $\sqrt{J_2}$ approaches an asymptotic level of 6,129 MPa as the mean stress approaches 30,000 MPa.

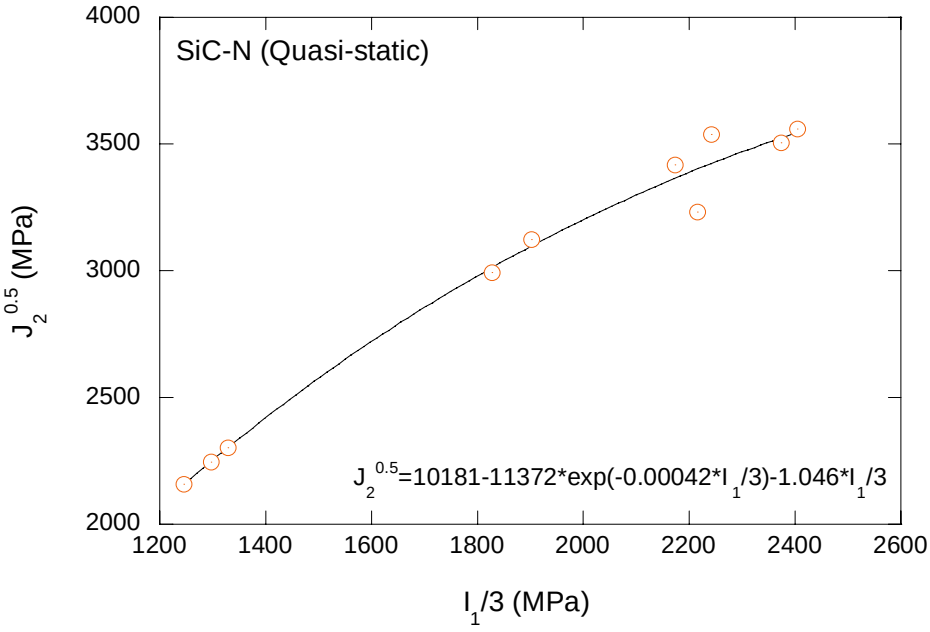

Figure 15. Shear failure criterion determined by the least square fit of the triaxial compression data for the SiC-N ceramics to the exponential shear yield surface of the cap model.

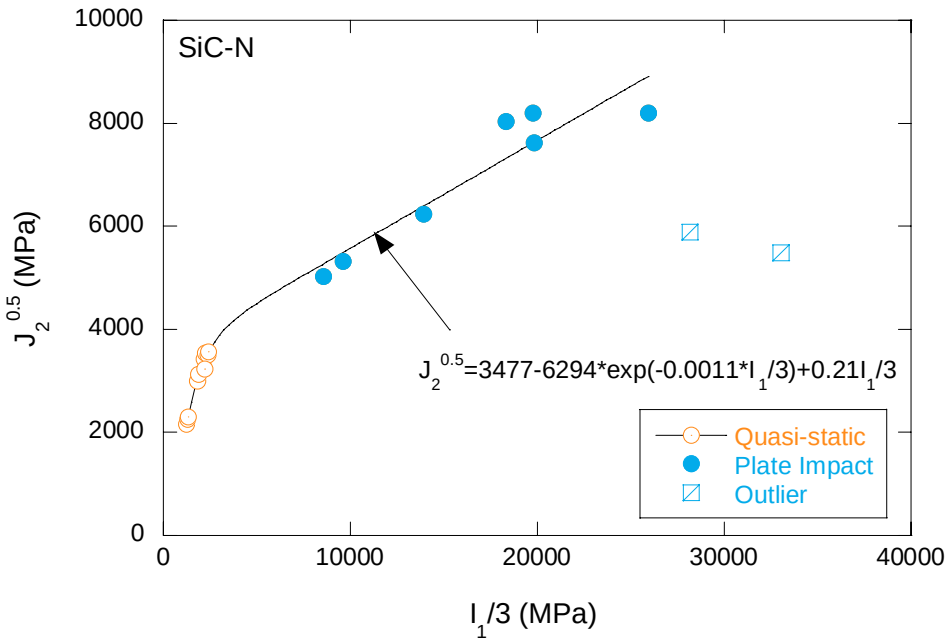

Figure 16. Failure criterion determined by the least square fit of the triaxial compression data (this report) and the shock experiment data (Vogler *et al.*, 2004) for the SiC-N ceramics.

8. Conclusions

To establish the mechanical properties and the failure criteria of the silicon carbide ceramics (SiC-N), a series of quasi-static compression tests has been completed using a high-pressure triaxial pressure vessel and the unique sample alignment jig. The results from laboratory constitutive experiments can be summarized as follows:

- The uniaxial unconfined compressive strength of SiC-N was 3872 ± 126 MPa.
- The elastic properties for the SiC-N were determined based on three unconfined compression tests:

  Young's modulus E=465 ± 2 GPa
  Poisson's ratio ν=0.16 ± 0.006

- Results from the uniaxial and the triaxial compression tests were used to obtain the failure criteria of SiC-N ceramics using the cap plasticity model. For quasi-static data, the failure criterion is represented as follows:

$$\sqrt{J_2} = 10181 - 11372 \cdot e^{-0.00042\frac{I_1}{3}} + 1.046\frac{I_1}{3}$$

  For quasi-static data and the plate impact test data provided by Vogler *et al*. (2004), the failure criterion is represented as follows:

$$\sqrt{J_2} = 3477 - 6294 \cdot e^{-0.0011\frac{I_1}{3}} + 0.21\frac{I_1}{3}$$

where I_1 and $\sqrt{J_2}$ are values in MPa.

The dependence of quasi-static failure strength of SiC-N ceramics on the confining pressures has been determined for the first time. Comparing and integrating these results with Kolsky bar data (e.g. Wang and Ramesh, 2004) and VISAR data (Vogler *et al.*, 2004) significantly advances progress toward calibration of ceramics models for penetration applications.

APPENDIX A

Stress-strain plots obtained from the uniaxial / triaxial compression tests of SiC-N specimens (σ_a-axial stress, ε_a-axial strain, ε_l-lateral strain, ε_v-volumetric strain, and P-confining pressure)

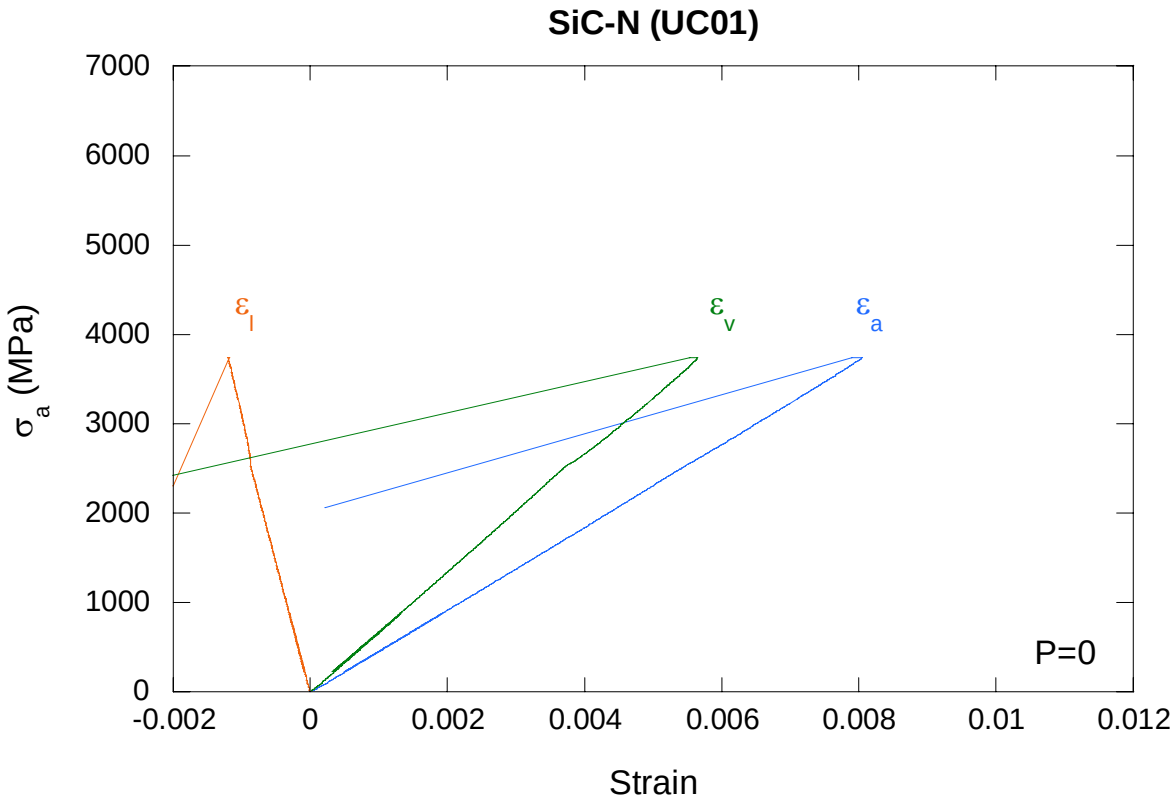
SiC-N (UC01)
7000
6000
5000
4000
3000
2000
1000
0
σa (MPa)
εl
εv
εa
P=0
-0.002
0
0.002
0.004
0.006
0.008
0.01
0.012
Strain

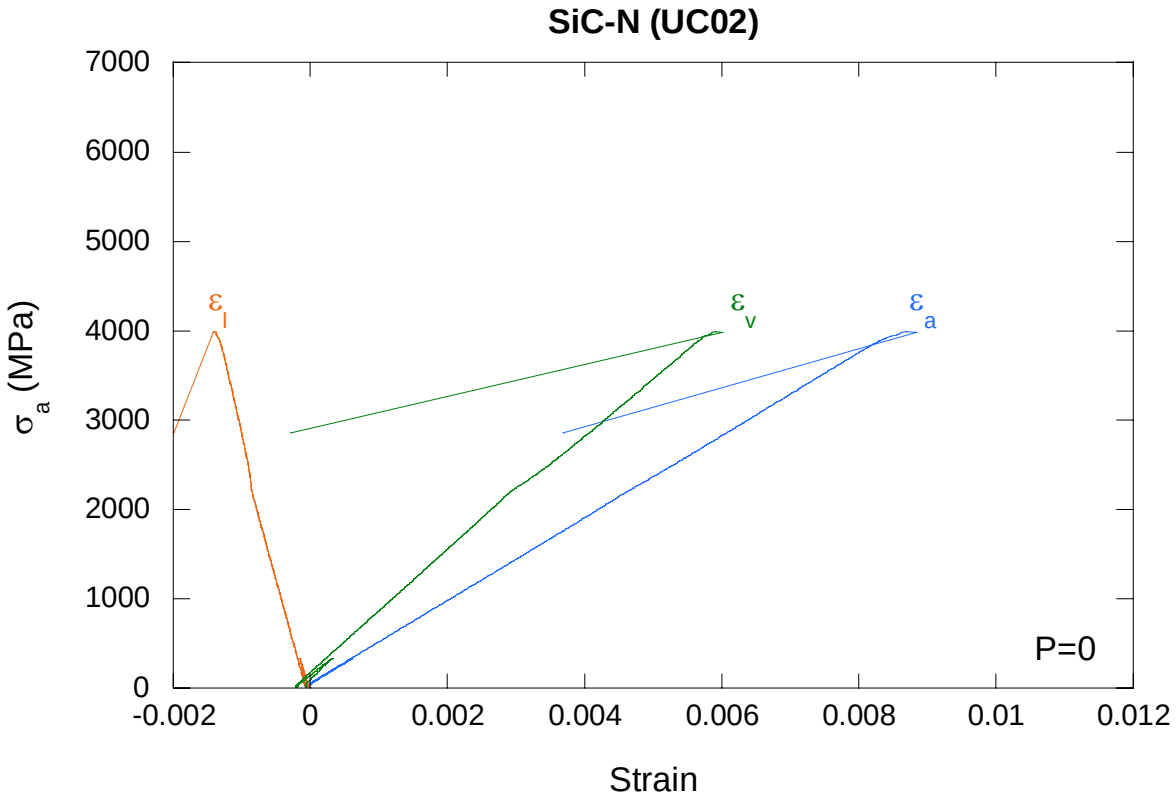
SiC-N (UC02)
7000
6000
5000
4000
3000
2000
1000
0
σa (MPa)
εl
εv
εa
P=0
-0.002
0
0.002
0.004
0.006
0.008
0.01
0.012
Strain

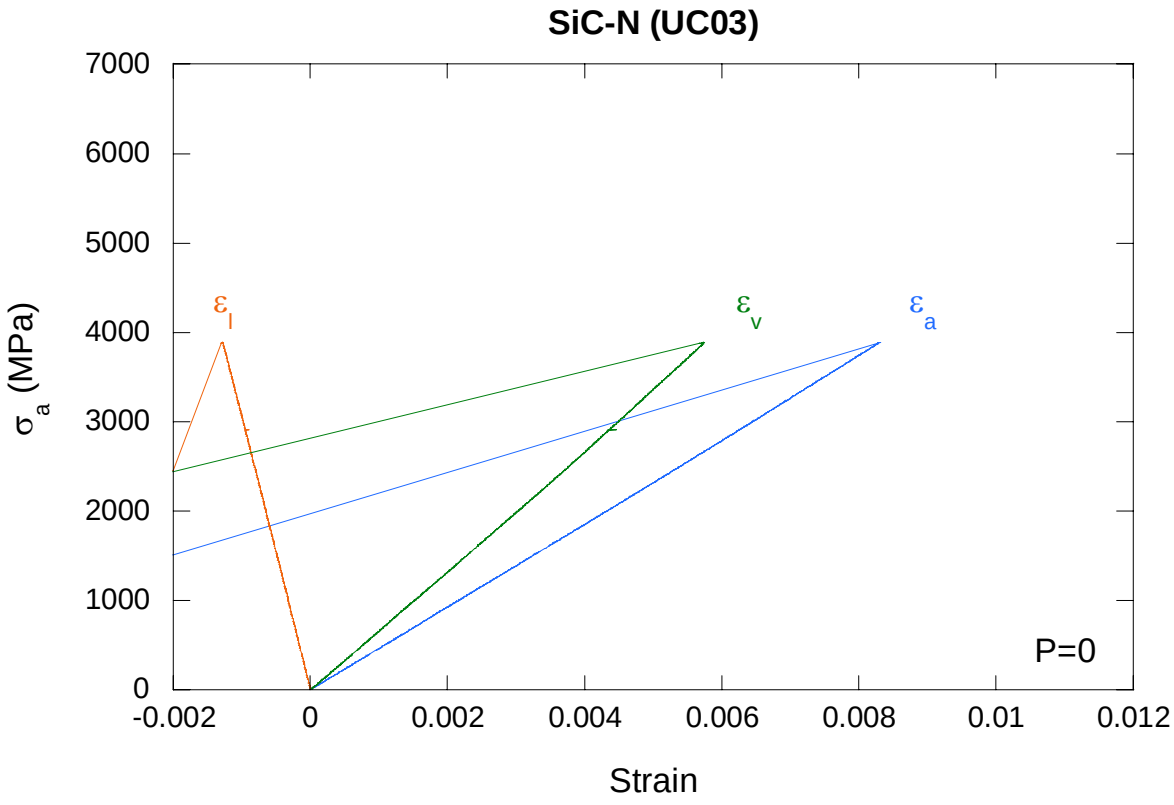
SiC-N (UC03)
7000
6000
5000
4000
3000
2000
1000
0
σa (MPa)
εl
εv
εa
P=0
-0.002
0
0.002
0.004
0.006
0.008
0.01
0.012
Strain

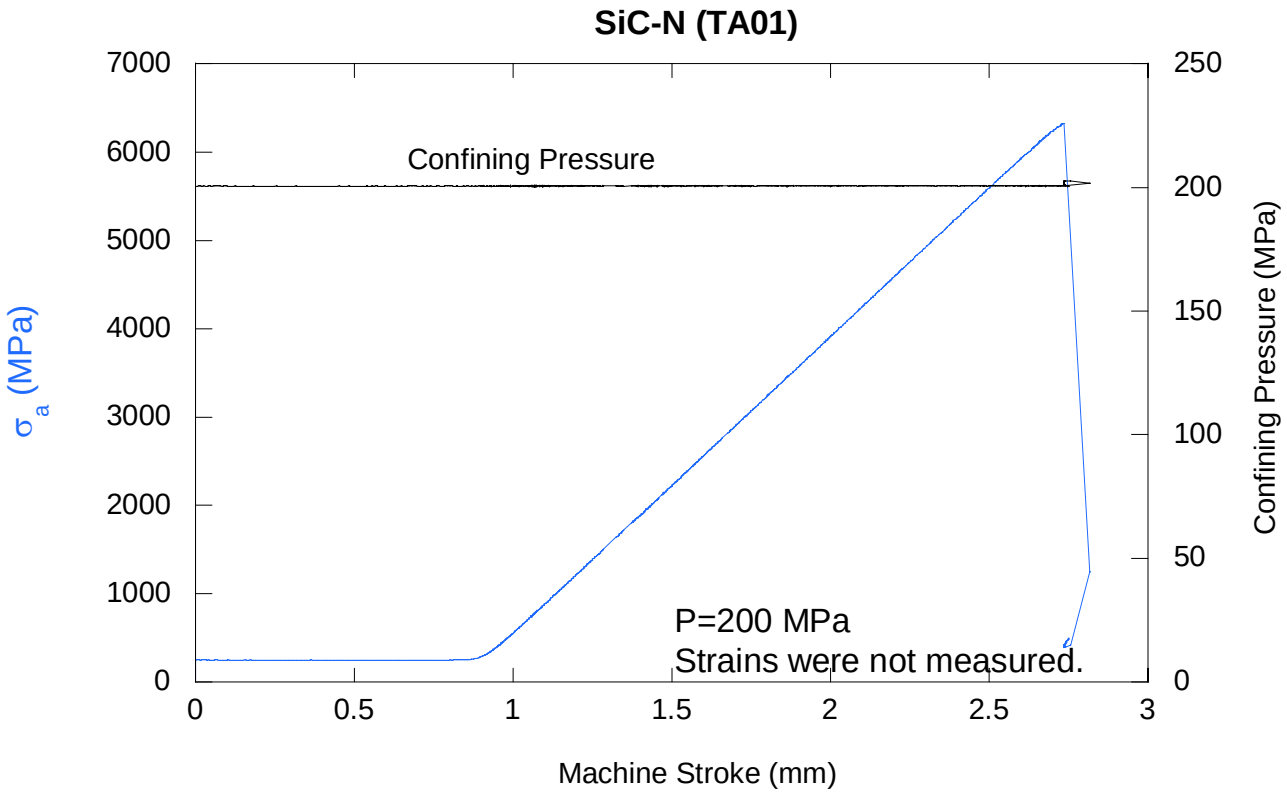
SiC-N (TA01)
7000
6000
5000
4000
3000
2000
1000
0
σa (MPa)
Confining Pressure
P=200 MPa
Strains were not measured.
250
200
150
100
50
0
Confining Pressure (MPa)
0
0.5
1
1.5
2
2.5
3
Machine Stroke (mm)

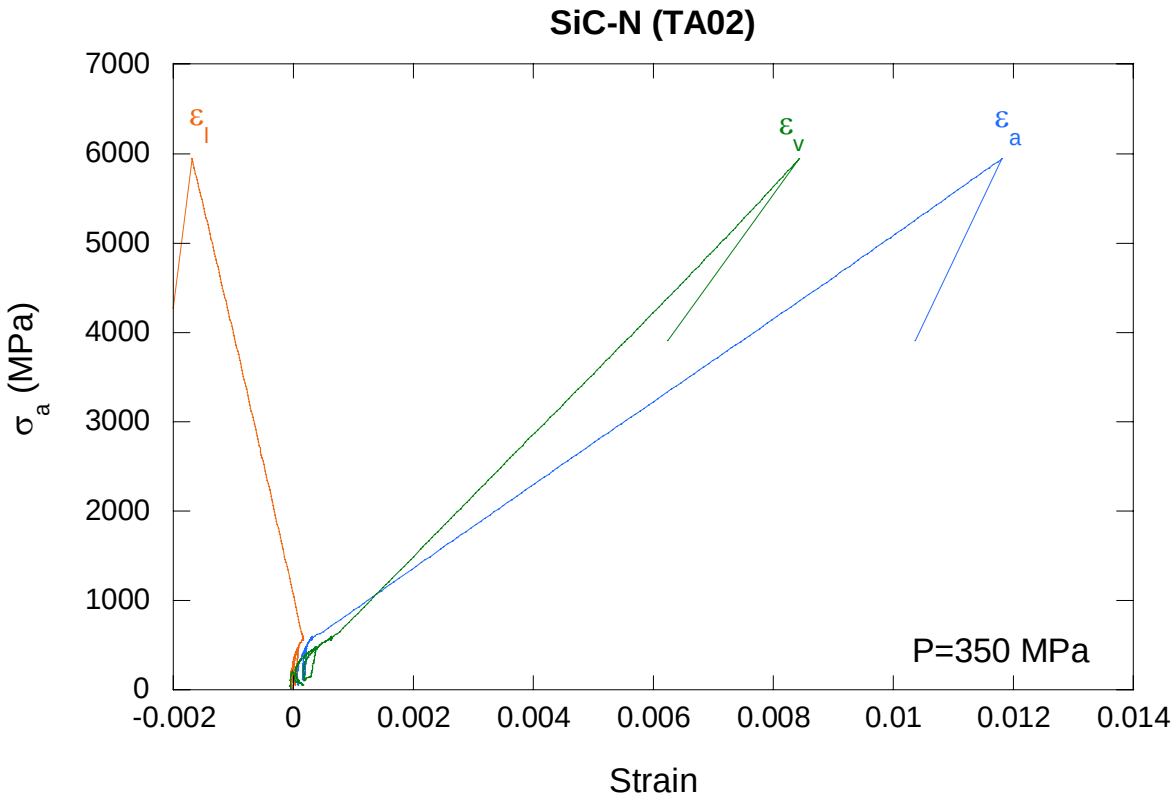
SiC-N (TA02)
7000
6000
5000
4000
3000
2000
1000
0
σa (MPa)
εl
εv
εa
P=350 MPa
-0.002
0
0.002
0.004
0.006
0.008
0.01
0.012
0.014
Strain

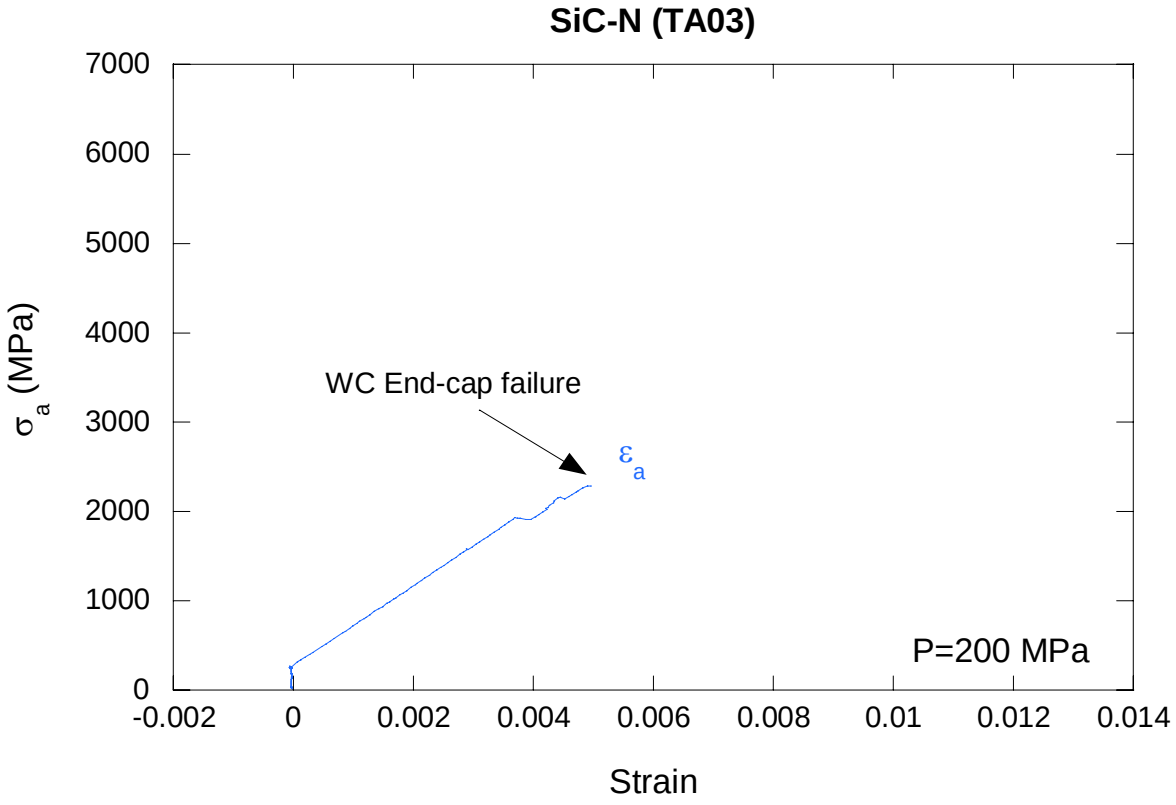
SiC-N (TA03)
7000
6000
5000
4000
3000
2000
1000
0
σa (MPa)
WC End-cap failure
εa
P=200 MPa
-0.002
0
0.002
0.004
0.006
0.008
0.01
0.012
0.014
Strain

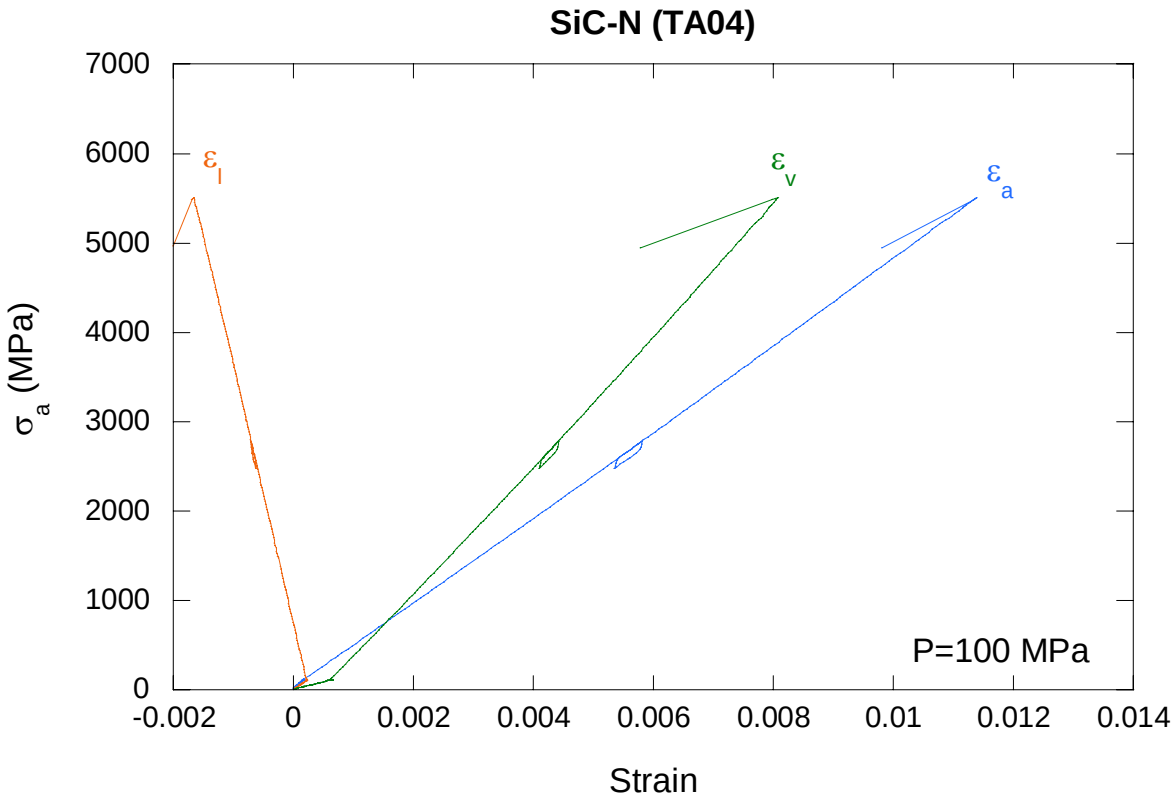
SiC-N (TA04)
7000
6000
5000
4000
3000
2000
1000
0
σa (MPa)
εl
εv
εa
P=100 MPa
-0.002
0
0.002
0.004
0.006
0.008
0.01
0.012
0.014
Strain

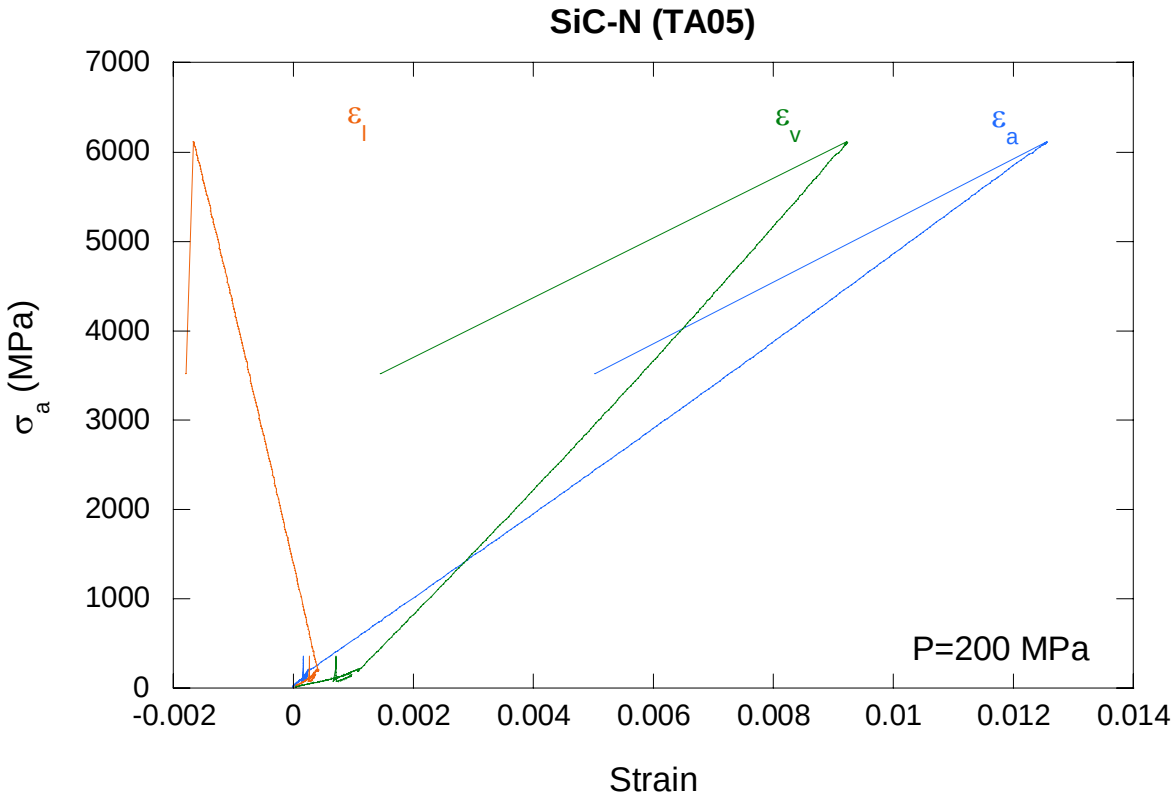
SiC-N (TA05)
7000
6000
5000
4000
3000
2000
1000
0
σa (MPa)
εl
εv
εa
P=200 MPa
-0.002
0
0.002
0.004
0.006
0.008
0.01
0.012
0.014
Strain

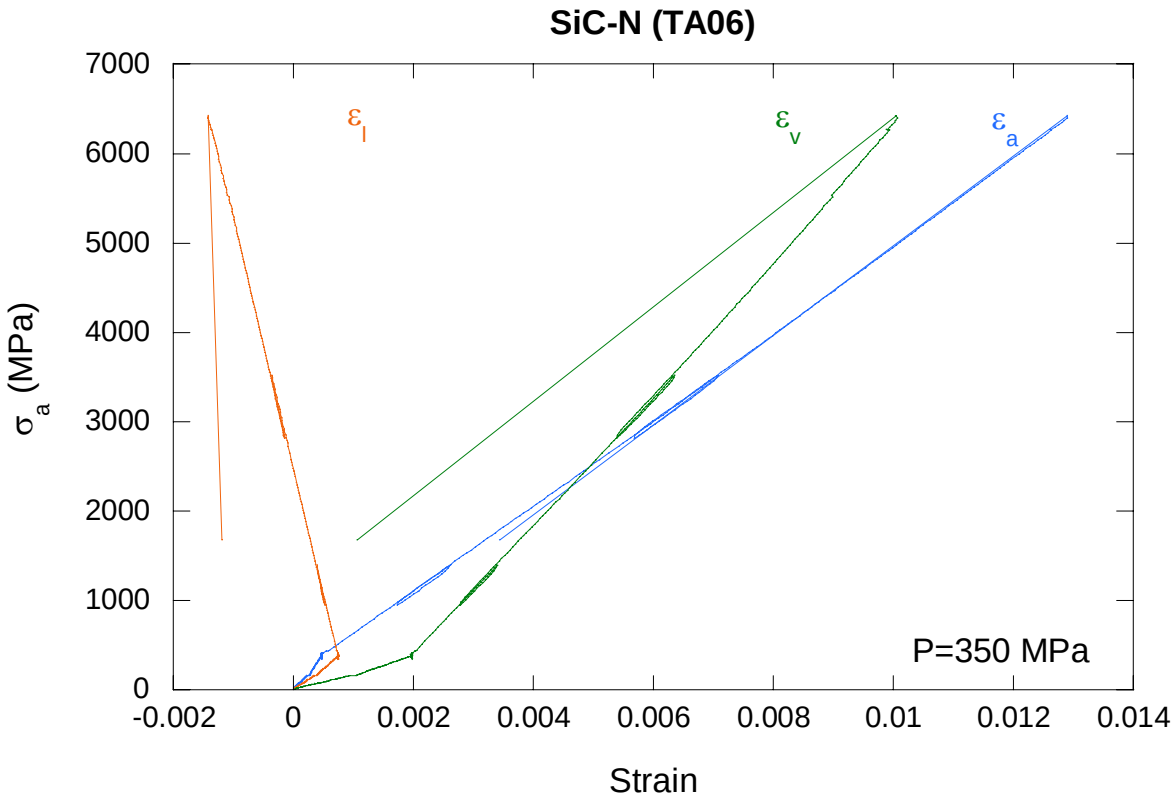
SiC-N (TA06)
7000
6000
5000
4000
3000
2000
1000
0
σa (MPa)
εl
εv
εa
P=350 MPa
-0.002
0
0.002
0.004
0.006
0.008
0.01
0.012
0.014
Strain

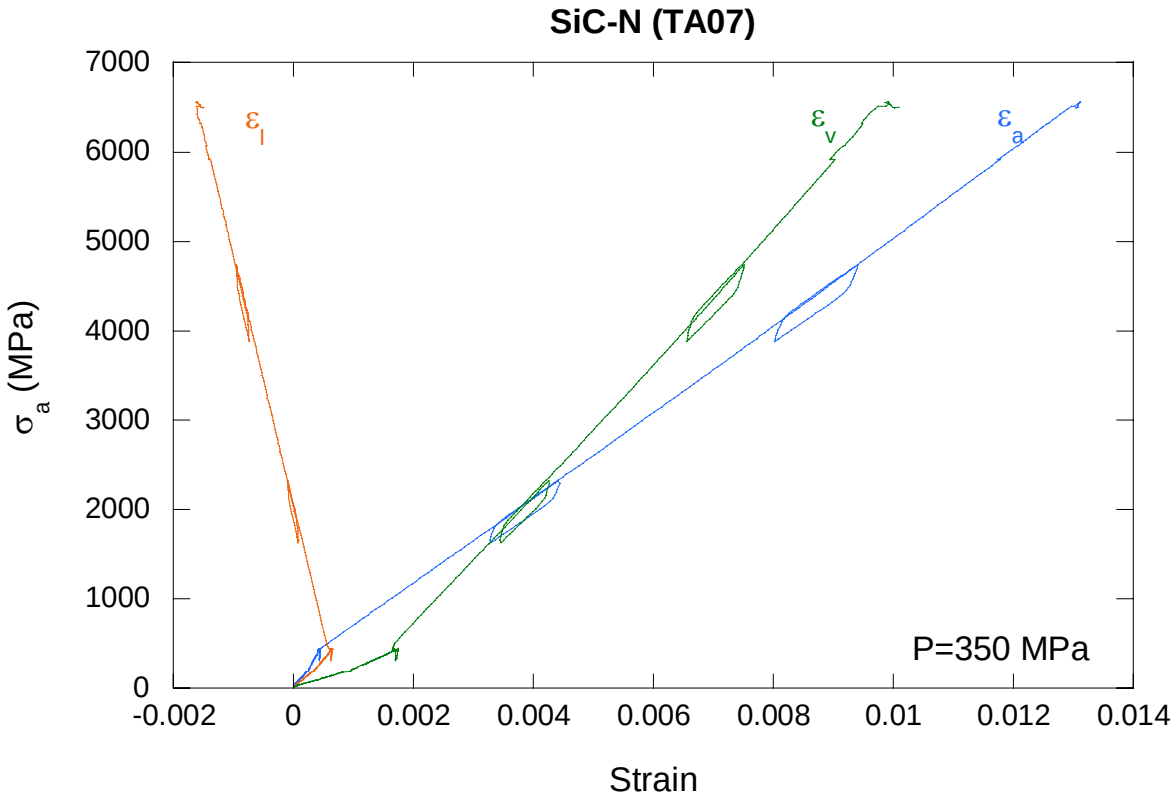
SiC-N (TA07)
7000
6000
5000
4000
3000
2000
1000
0
σa (MPa)
εl
εv
εa
P=350 MPa
-0.002
0
0.002
0.004
0.006
0.008
0.01
0.012
0.014
Strain

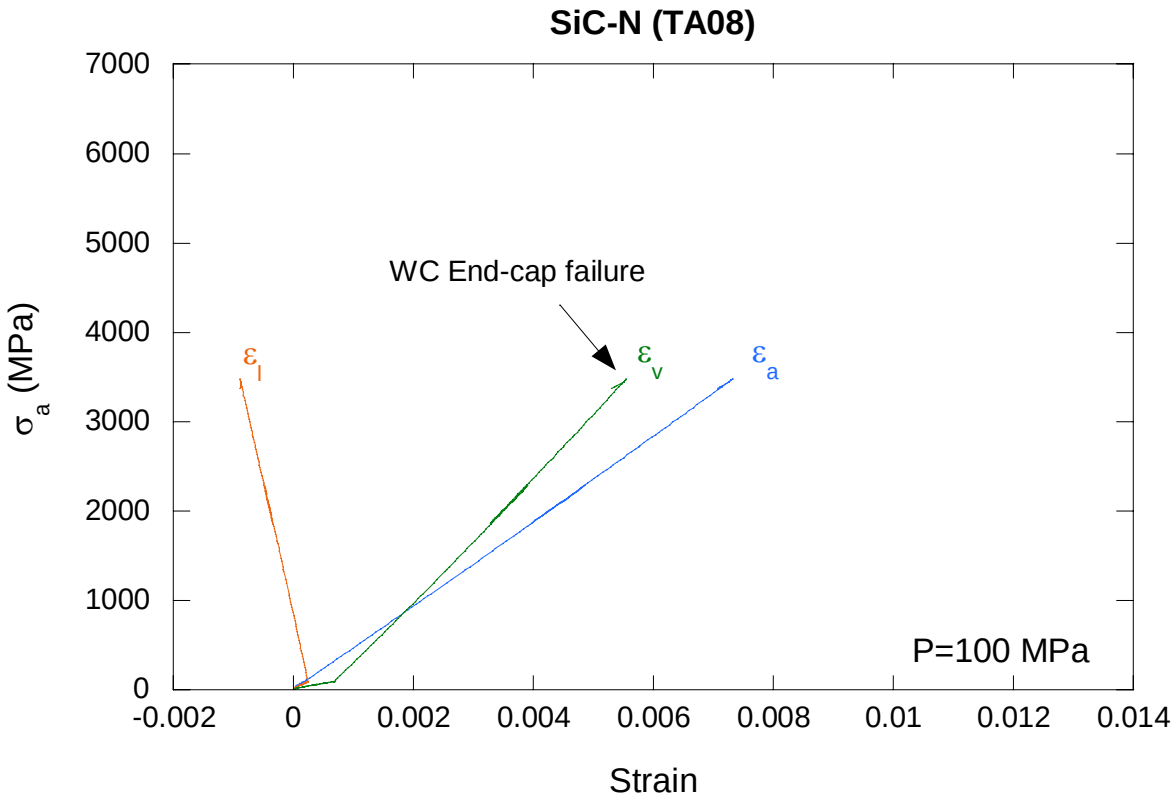
SiC-N (TA08)
7000
6000
5000
4000
3000
2000
1000
0
σa (MPa)
WC End-cap failure
εl
εv
εa
P=100 MPa
-0.002
0
0.002
0.004
0.006
0.008
0.01
0.012
0.014
Strain

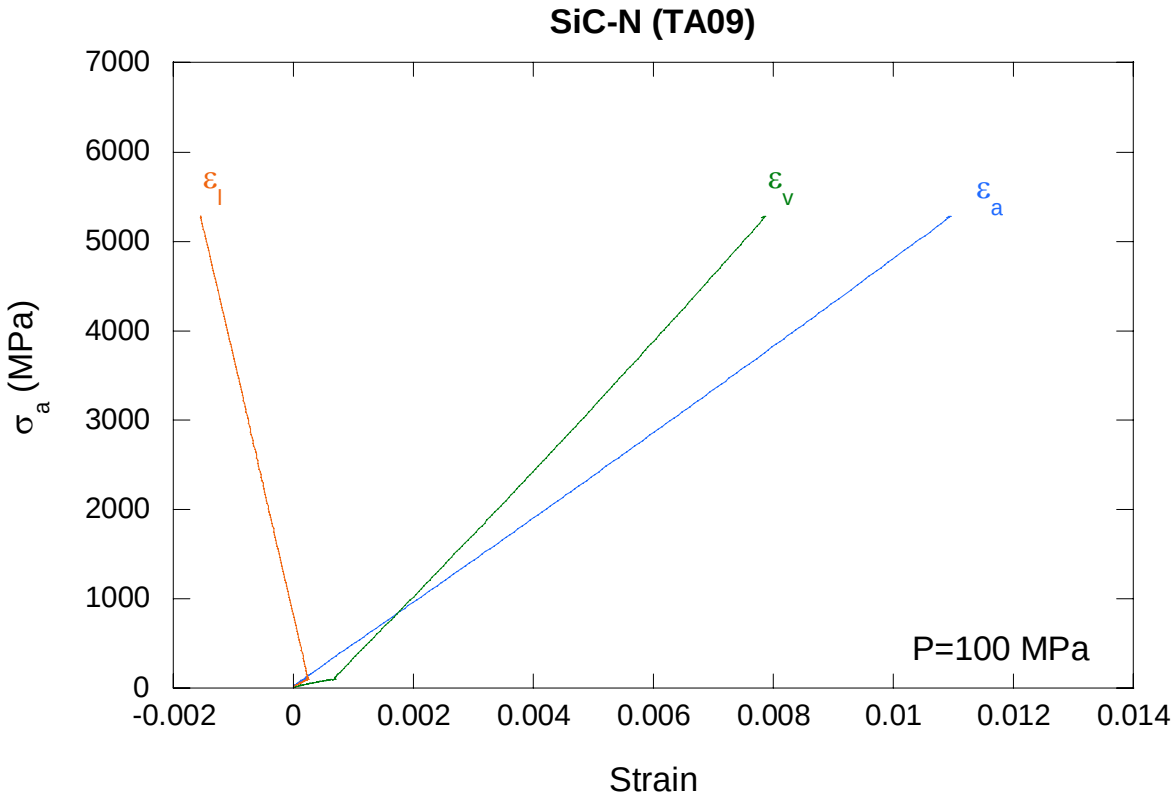
SiC-N (TA09)
7000
6000
5000
4000
3000
2000
1000
0
σa (MPa)
εl
εv
εa
P=100 MPa
-0.002
0
0.002
0.004
0.006
0.008
0.01
0.012
0.014
Strain

APPENDIX B

Young's modulus, E, determined from the uniaxial / triaxial compression tests of SiC-N specimens (σ_a-axial stress, ε_a-axial strain, and P-confining pressure)

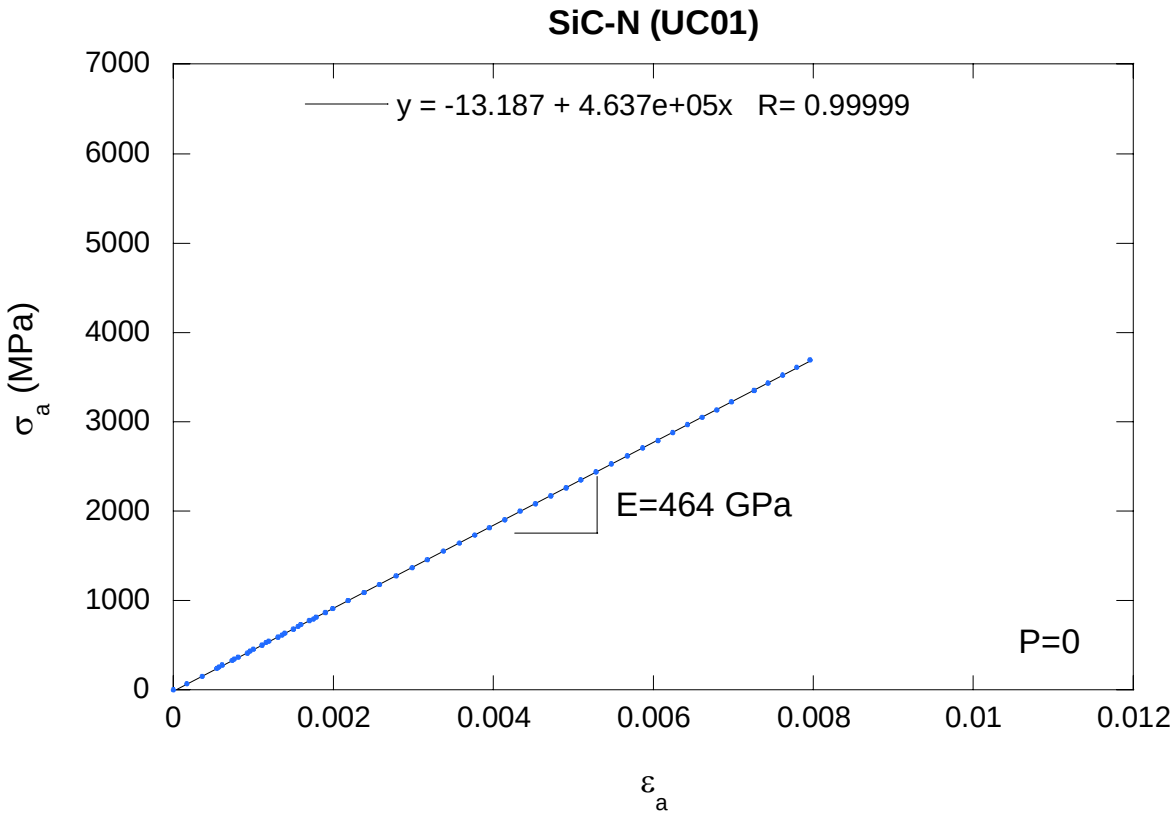
SiC-N (UC01)
y = -13.187 + 4.637e+05x R= 0.99999
E=464 GPa
P=0
σa (MPa)
εa
0
1000
2000
3000
4000
5000
6000
7000
0
0.002
0.004
0.006
0.008
0.01
0.012

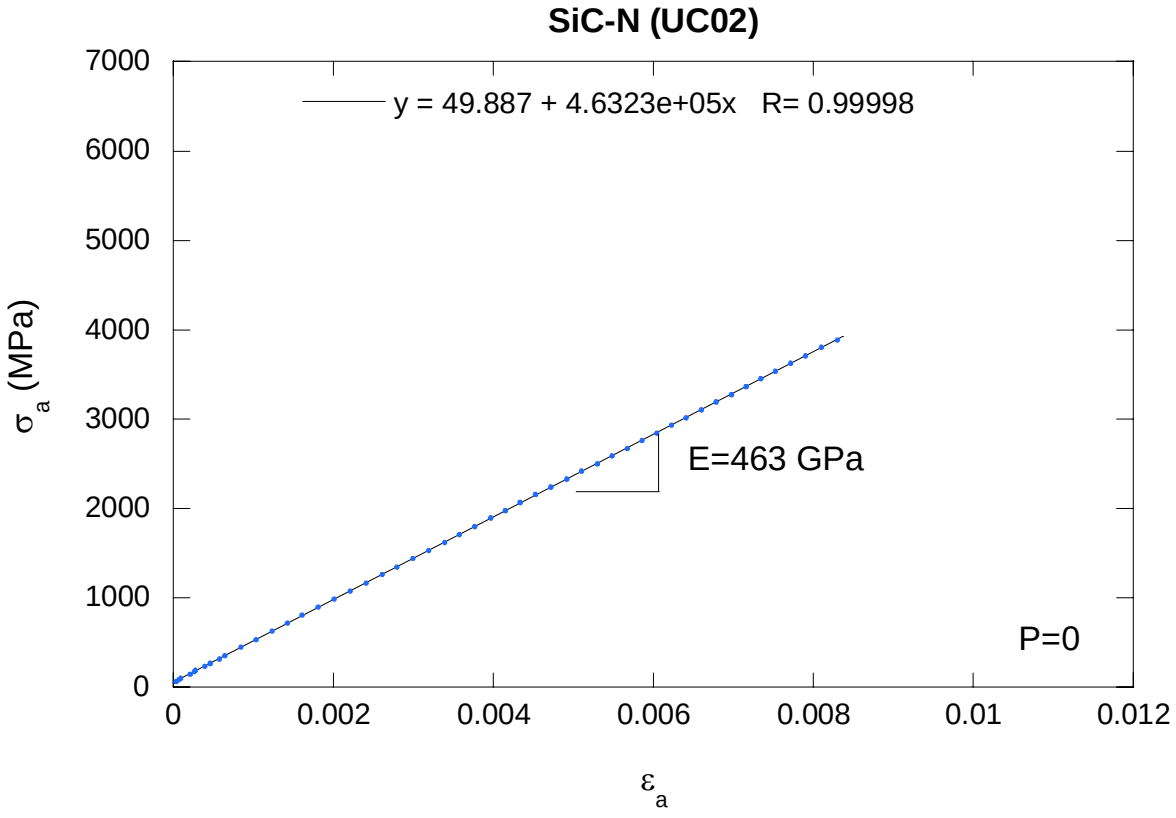
SiC-N (UC02)
y = 49.887 + 4.6323e+05x R= 0.99998
E=463 GPa
P=0
σa (MPa)
εa
0
1000
2000
3000
4000
5000
6000
7000
0
0.002
0.004
0.006
0.008
0.01
0.012

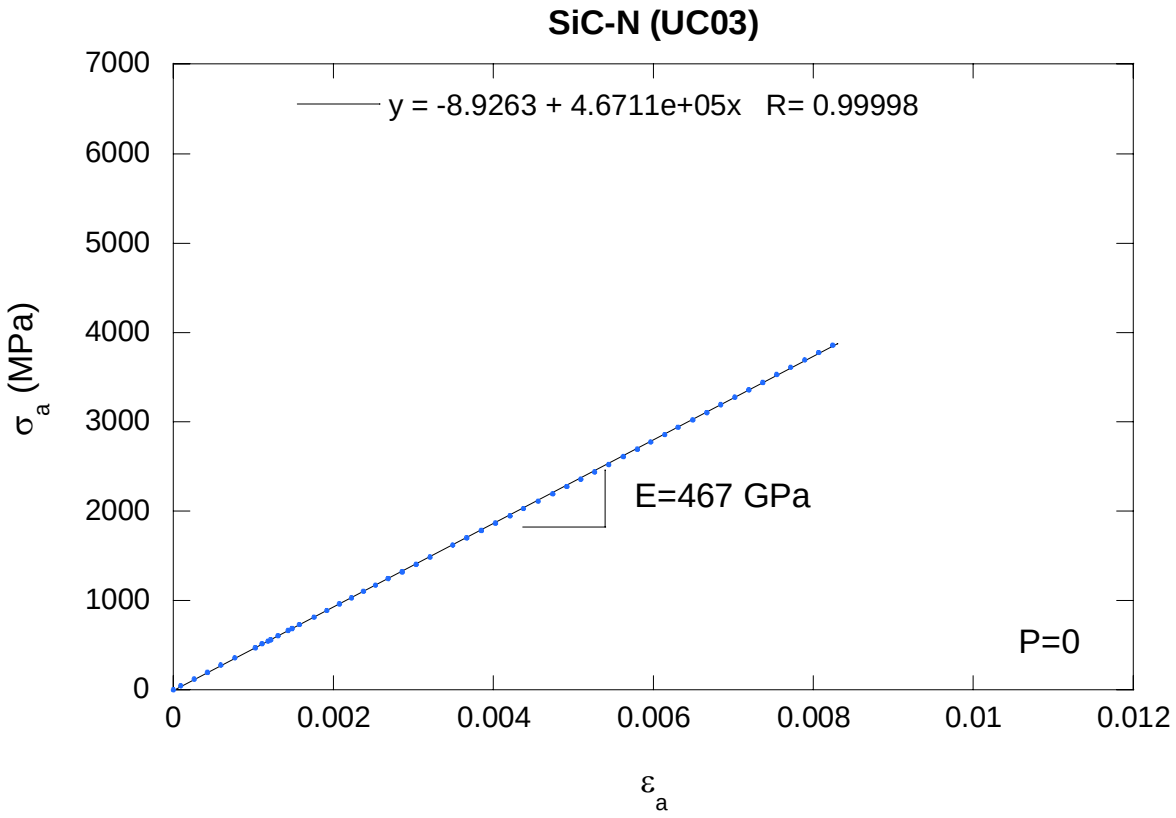
SiC-N (UC03)
y = -8.9263 + 4.6711e+05x R= 0.99998
E=467 GPa
P=0
σa (MPa)
εa
0
1000
2000
3000
4000
5000
6000
7000
0
0.002
0.004
0.006
0.008
0.01
0.012

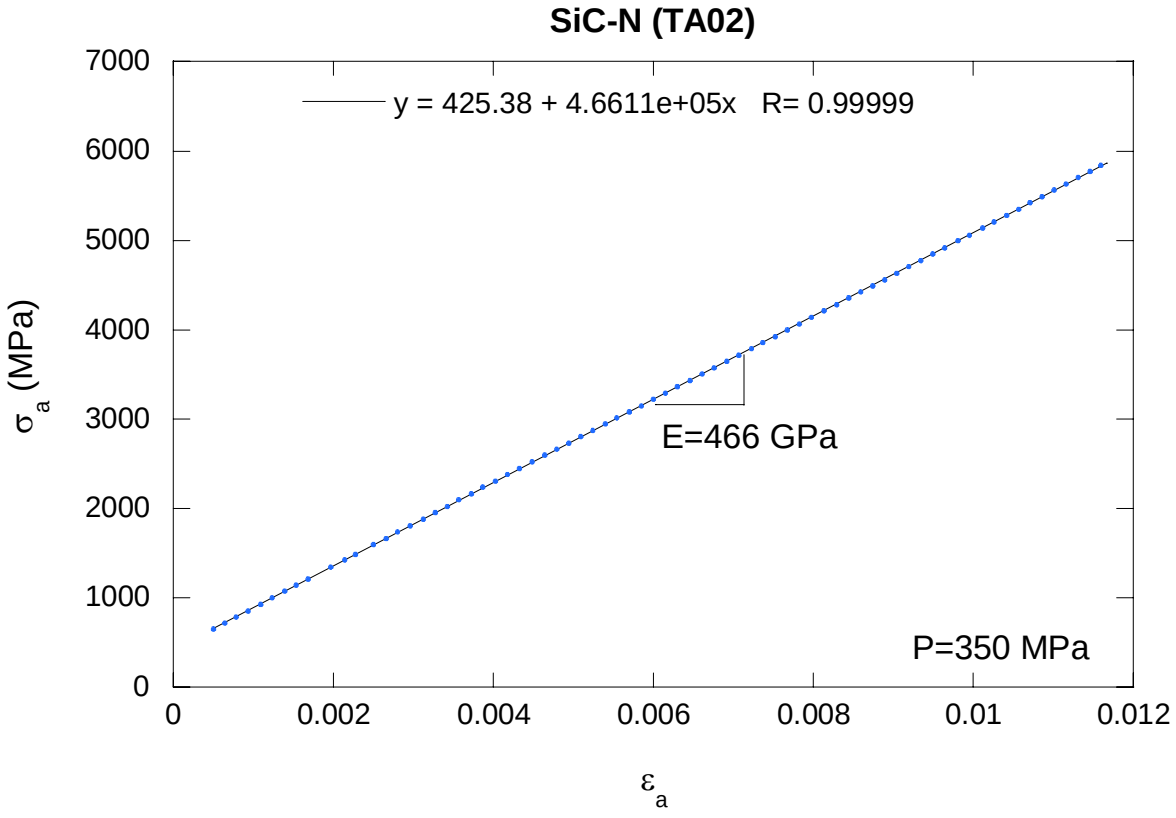
SiC-N (TA02)
y = 425.38 + 4.6611e+05x R= 0.99999
E=466 GPa
P=350 MPa
σa (MPa)
εa
0
1000
2000
3000
4000
5000
6000
7000
0
0.002
0.004
0.006
0.008
0.01
0.012

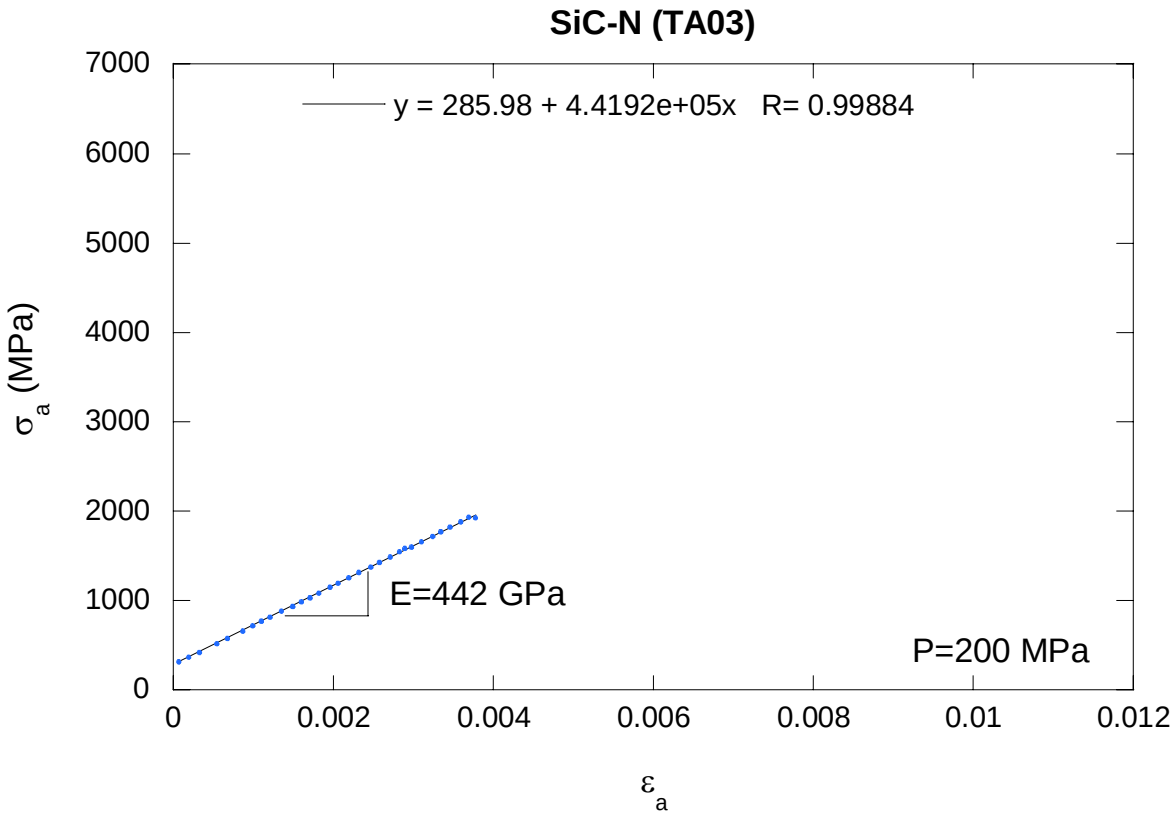
SiC-N (TA03)
y = 285.98 + 4.4192e+05x R= 0.99884
E=442 GPa
P=200 MPa
σa (MPa)
εa
0
1000
2000
3000
4000
5000
6000
7000
0.002
0.004
0.006
0.008
0.01
0.012

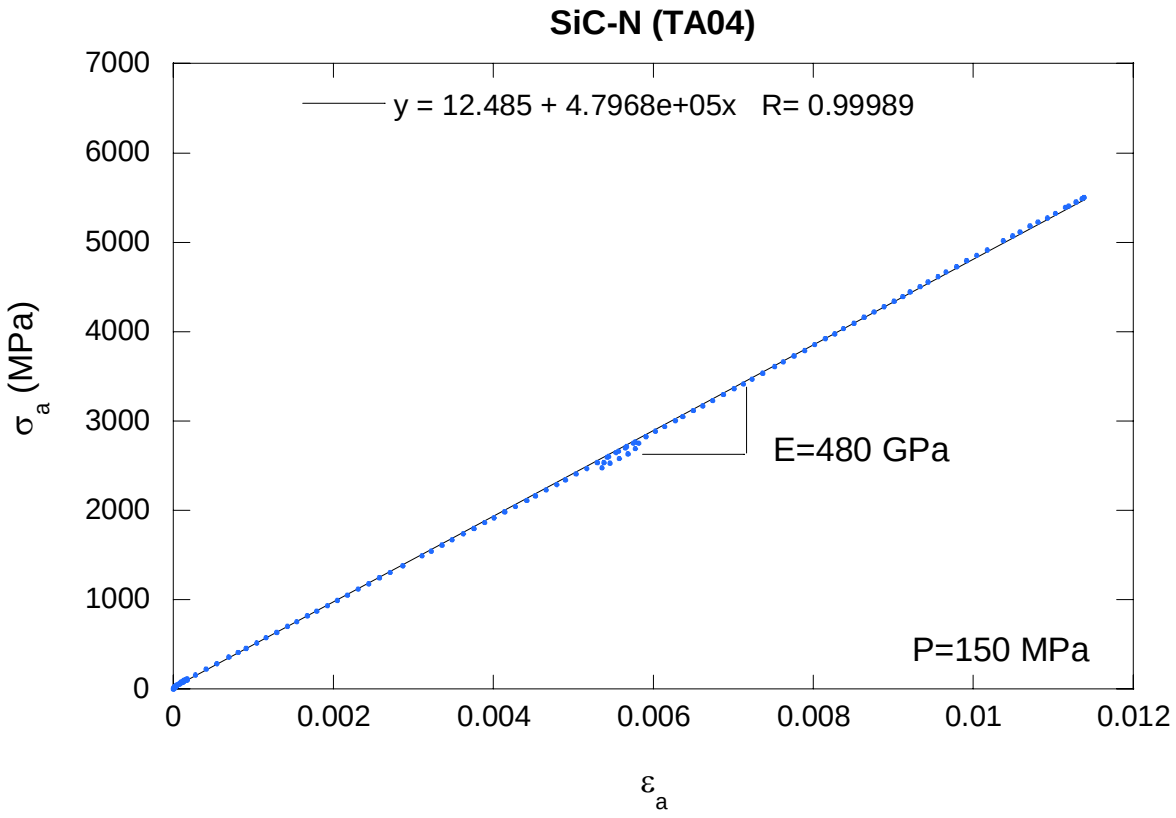
SiC-N (TA04)
y = 12.485 + 4.7968e+05x R= 0.99989
E=480 GPa
P=150 MPa
σa (MPa)
εa
0
1000
2000
3000
4000
5000
6000
7000
0.002
0.004
0.006
0.008
0.01
0.012

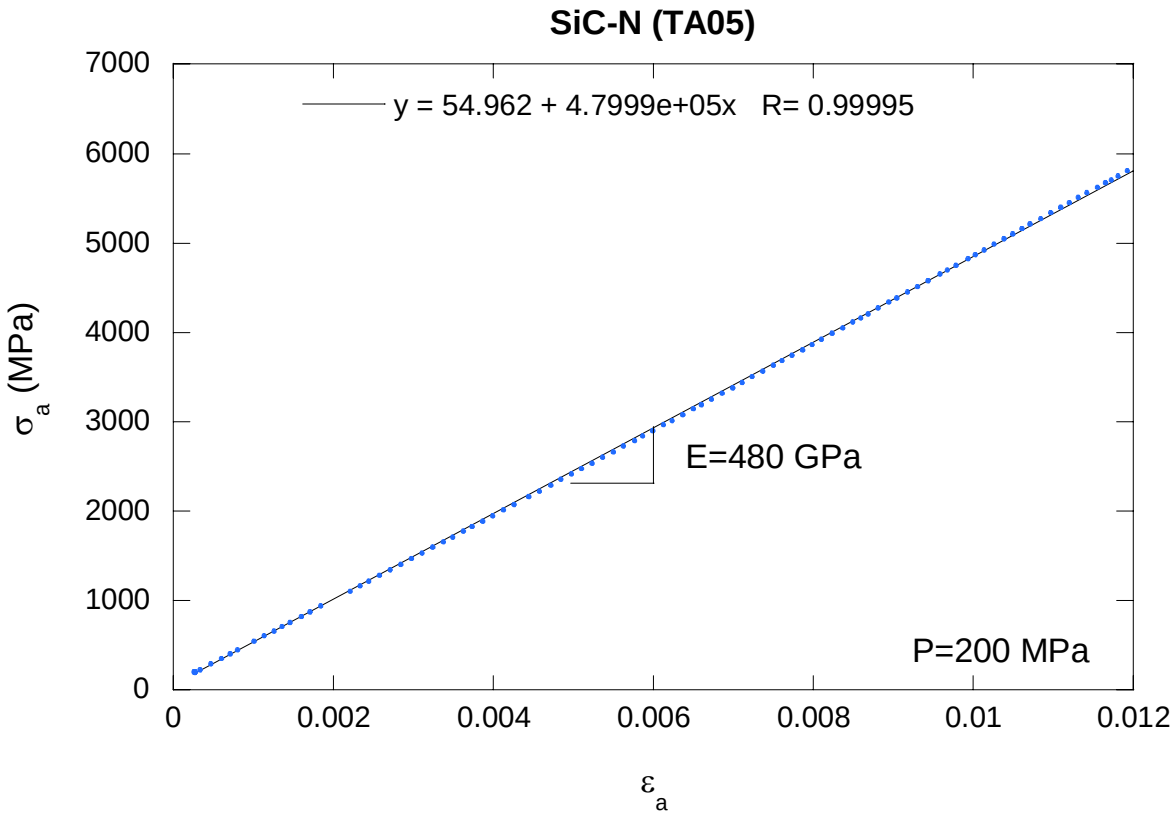
SiC-N (TA05)
y = 54.962 + 4.7999e+05x R= 0.99995
E=480 GPa
P=200 MPa
σa (MPa)
εa
0
1000
2000
3000
4000
5000
6000
7000
0
0.002
0.004
0.006
0.008
0.01
0.012

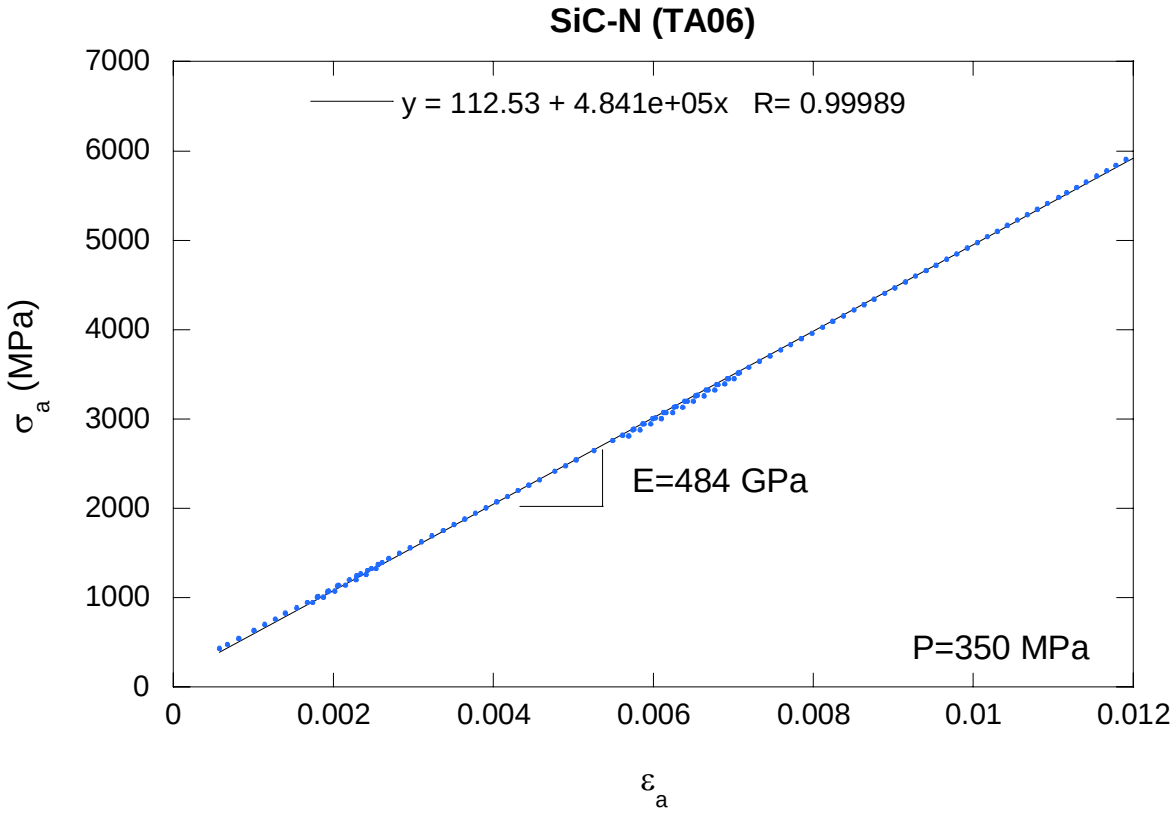
SiC-N (TA06)
y = 112.53 + 4.841e+05x R= 0.99989
E=484 GPa
P=350 MPa
σa (MPa)
εa
0
1000
2000
3000
4000
5000
6000
7000
0
0.002
0.004
0.006
0.008
0.01
0.012

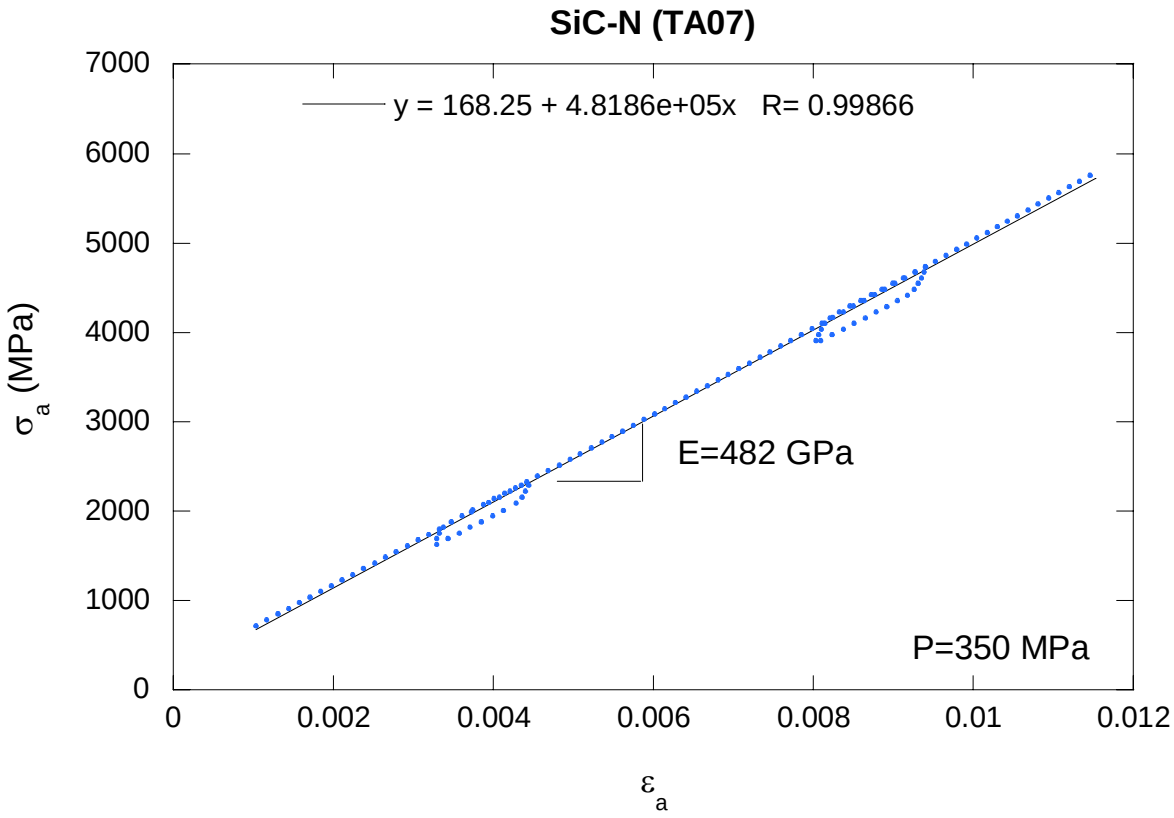
SiC-N (TA07)
y = 168.25 + 4.8186e+05x R= 0.99866
E=482 GPa
P=350 MPa
σa (MPa)
εa
0
1000
2000
3000
4000
5000
6000
7000
0
0.002
0.004
0.006
0.008
0.01
0.012

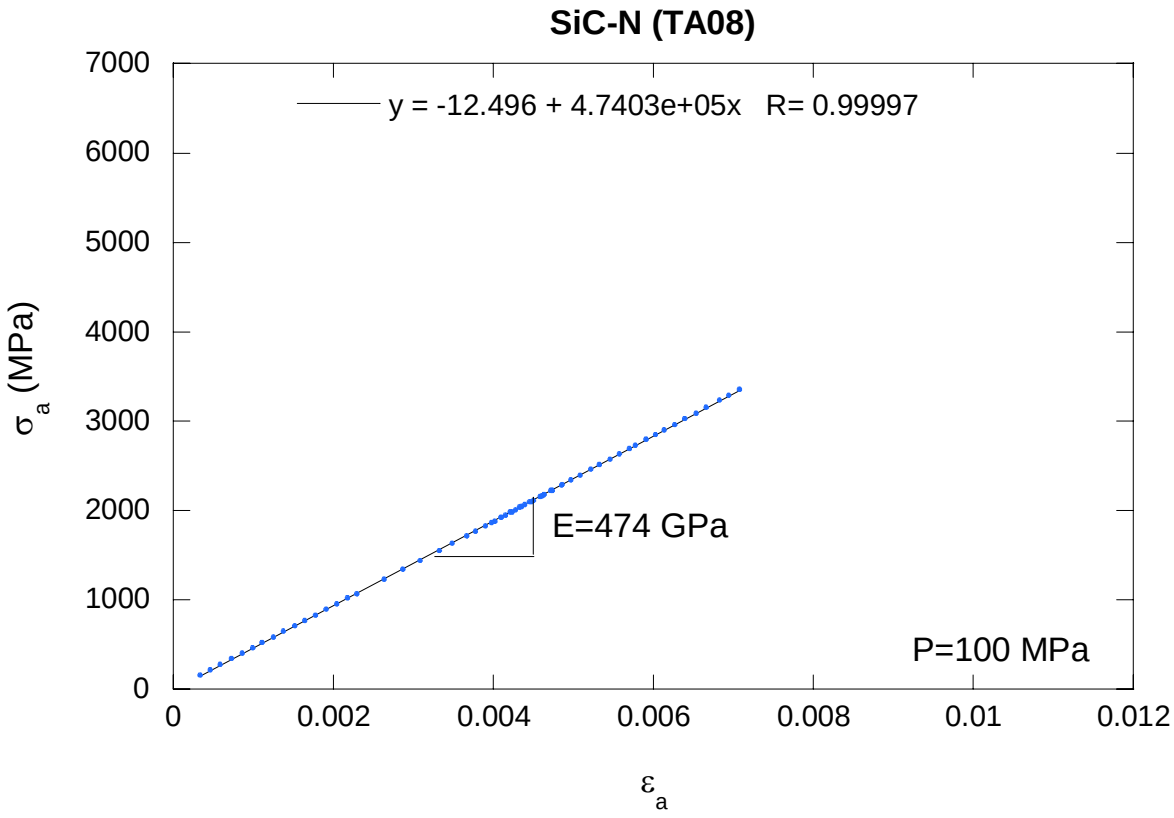
SiC-N (TA08)
y = -12.496 + 4.7403e+05x R= 0.99997
E=474 GPa
P=100 MPa
σa (MPa)
εa
0
1000
2000
3000
4000
5000
6000
7000
0
0.002
0.004
0.006
0.008
0.01
0.012

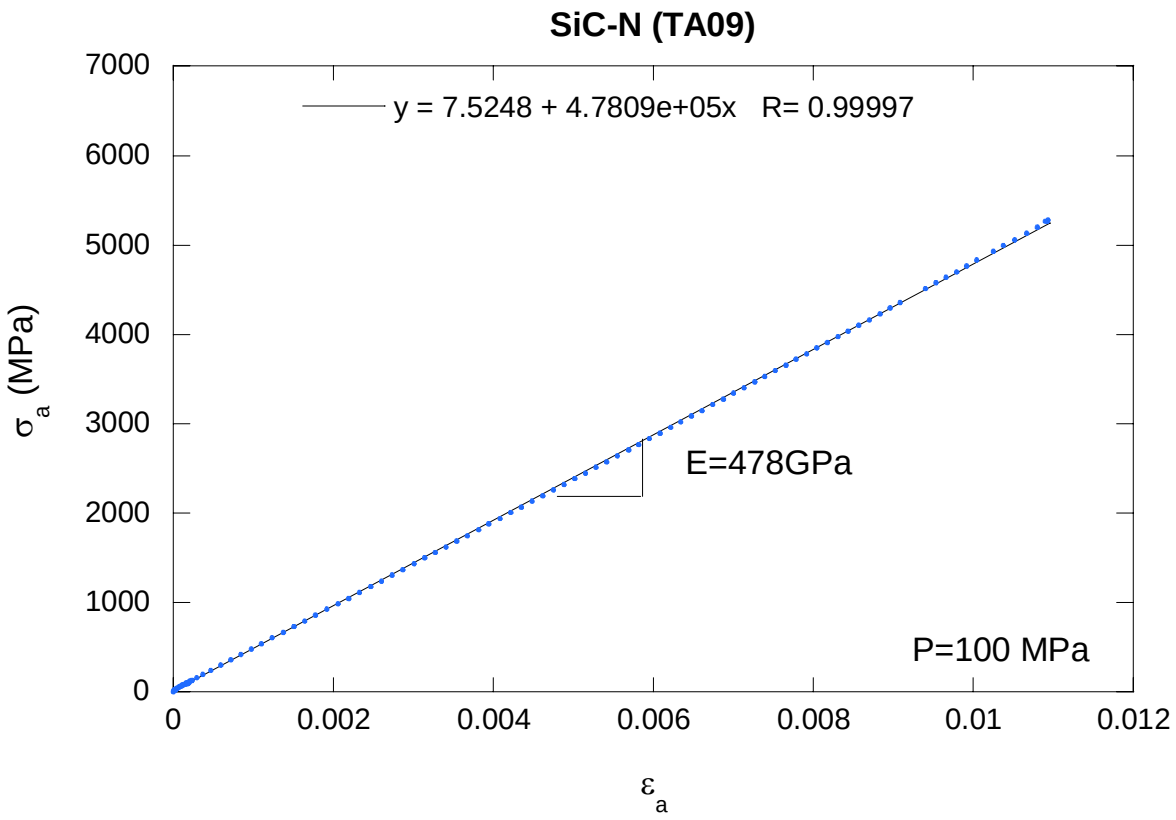
SiC-N (TA09)
y = 7.5248 + 4.7809e+05x R= 0.99997
E=478GPa
P=100 MPa
σa (MPa)
εa
7000
6000
5000
4000
3000
2000
1000
0
0
0.002
0.004
0.006
0.008
0.01
0.012

APPENDIX C

Poisson's ratio, ν, determined from the uniaxial compression tests of SiC-N specimens (ε_a-axial strain, ε_l-lateral strain, and P-confining pressure)

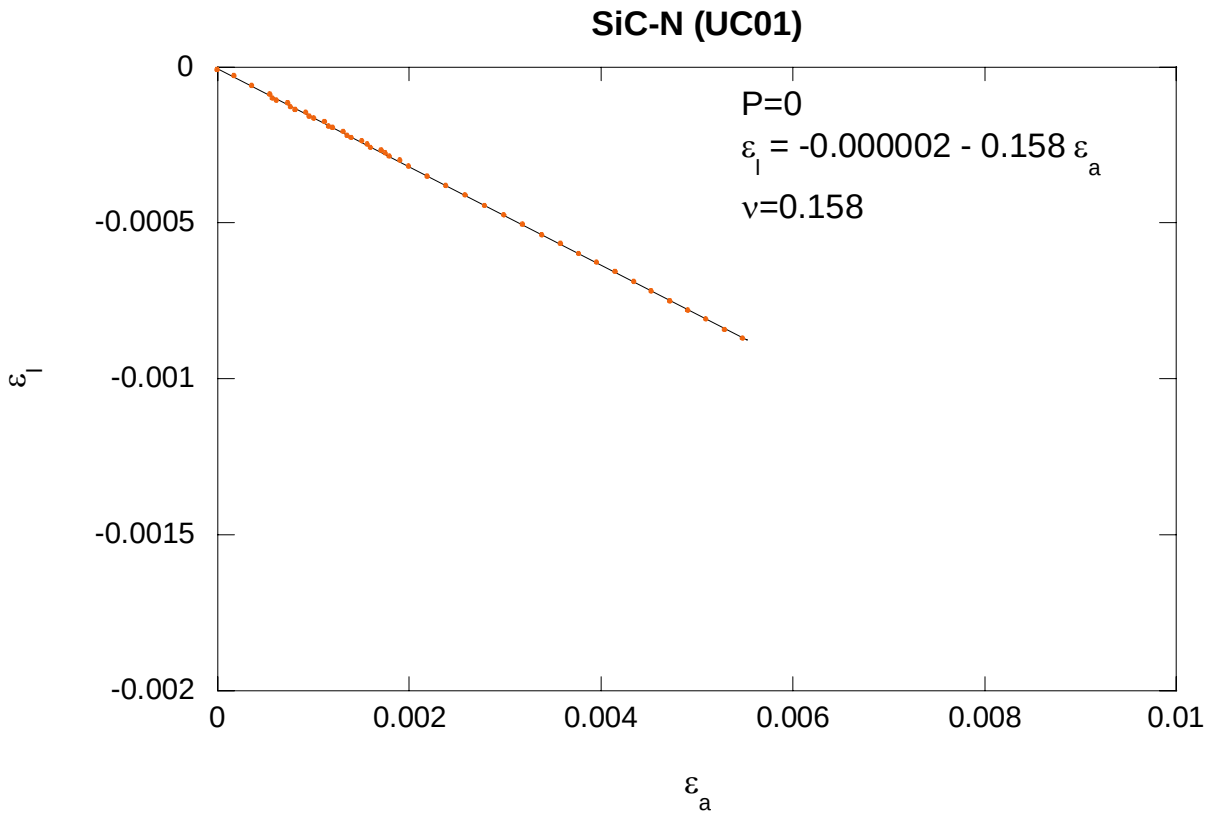
SiC-N (UC01)
P=0
$\varepsilon_l = -0.000002 - 0.158\,\varepsilon_a$
ν=0.158
0
-0.0005
-0.001
-0.0015
-0.002
0
0.002
0.004
0.006
0.008
0.01
ε_l
ε_a

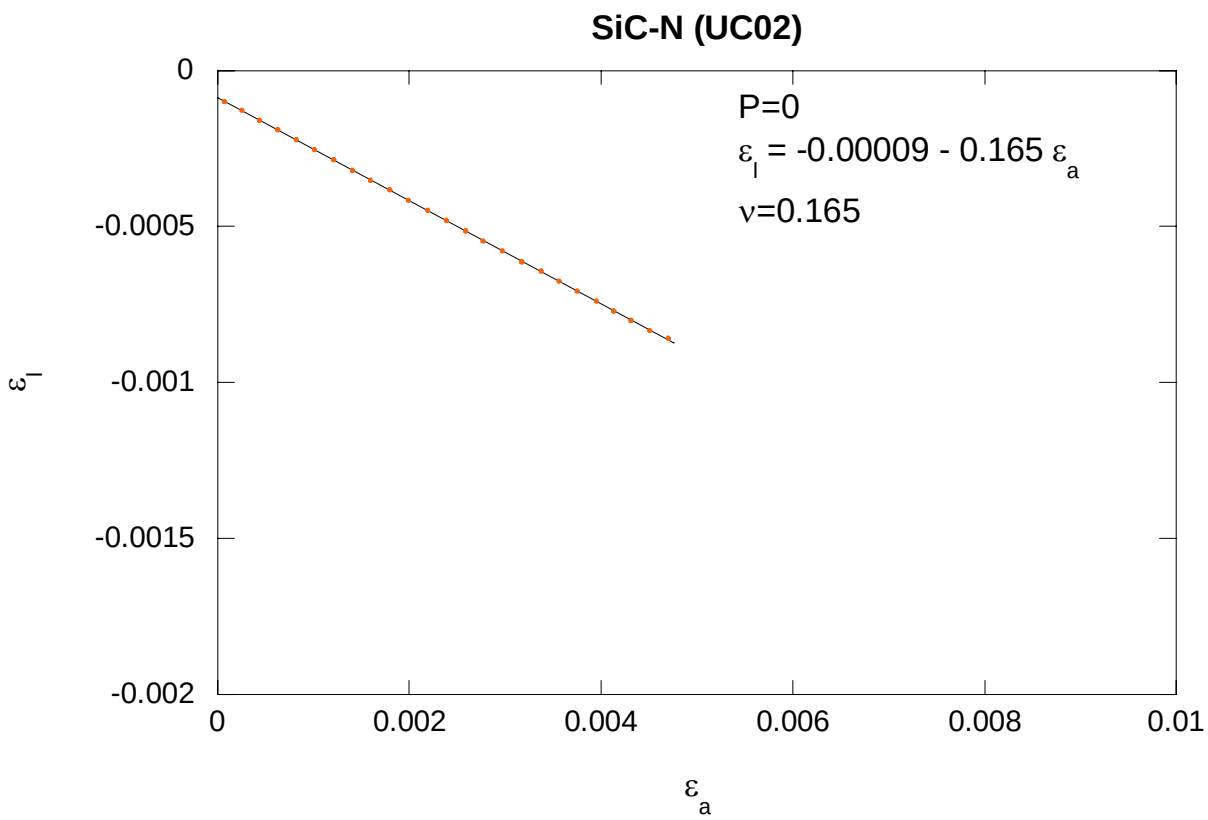
SiC-N (UC02)
P=0
$\varepsilon_l = -0.00009 - 0.165\,\varepsilon_a$
ν=0.165
0
-0.0005
-0.001
-0.0015
-0.002
0
0.002
0.004
0.006
0.008
0.01
ε_l
ε_a

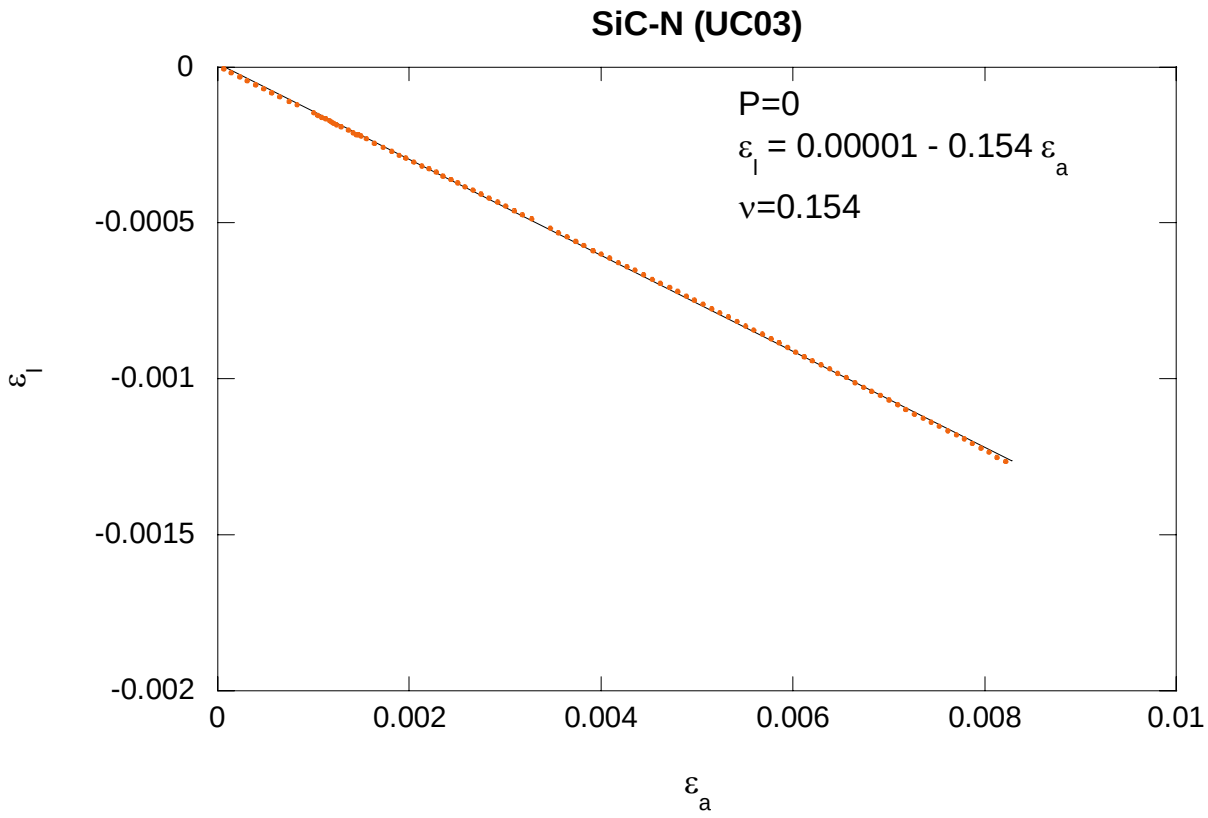
SiC-N (UC03)
P=0
$\varepsilon_l = 0.00001 - 0.154\ \varepsilon_a$
ν=0.154
ε_l
ε_a
0
-0.0005
-0.001
-0.0015
-0.002
0
0.002
0.004
0.006
0.008
0.01

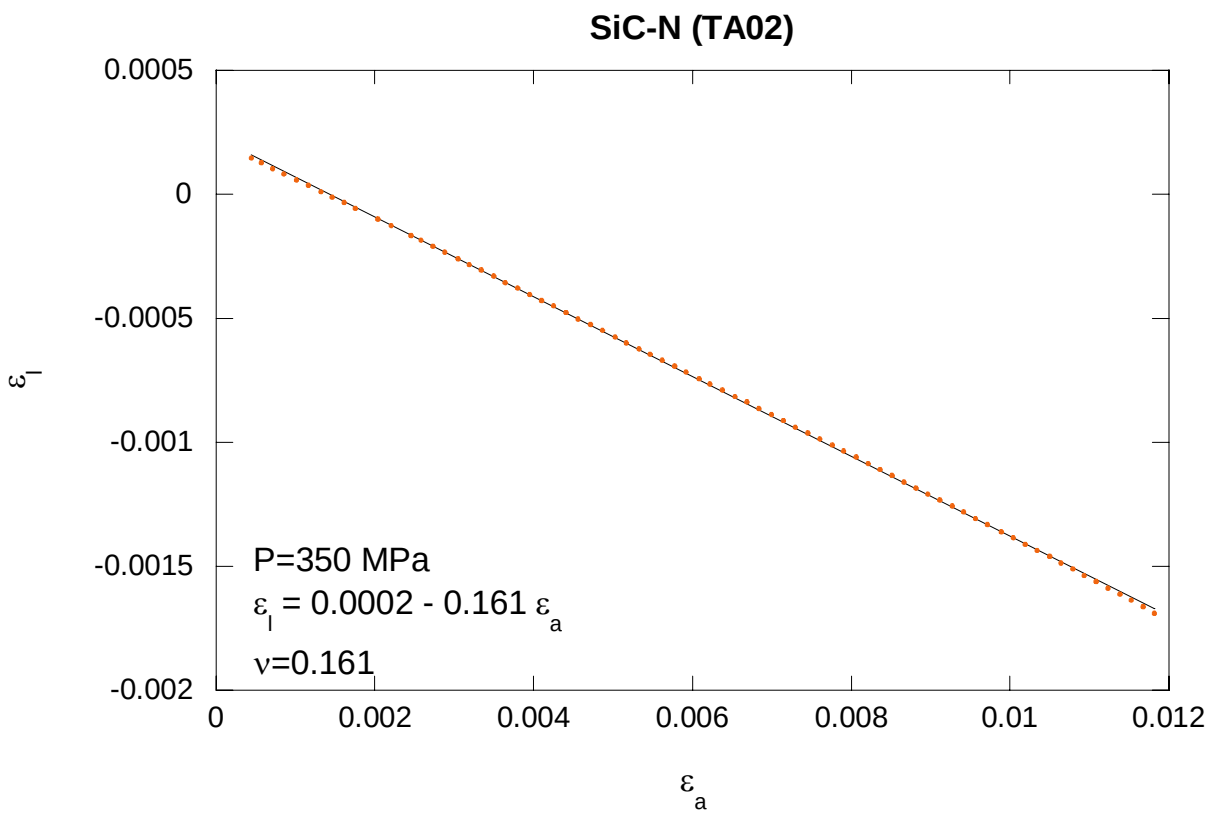
SiC-N (TA02)
P=350 MPa
$\varepsilon_l = 0.0002 - 0.161\ \varepsilon_a$
ν=0.161
ε_l
ε_a
0.0005
0
-0.0005
-0.001
-0.0015
-0.002
0
0.002
0.004
0.006
0.008
0.01
0.012

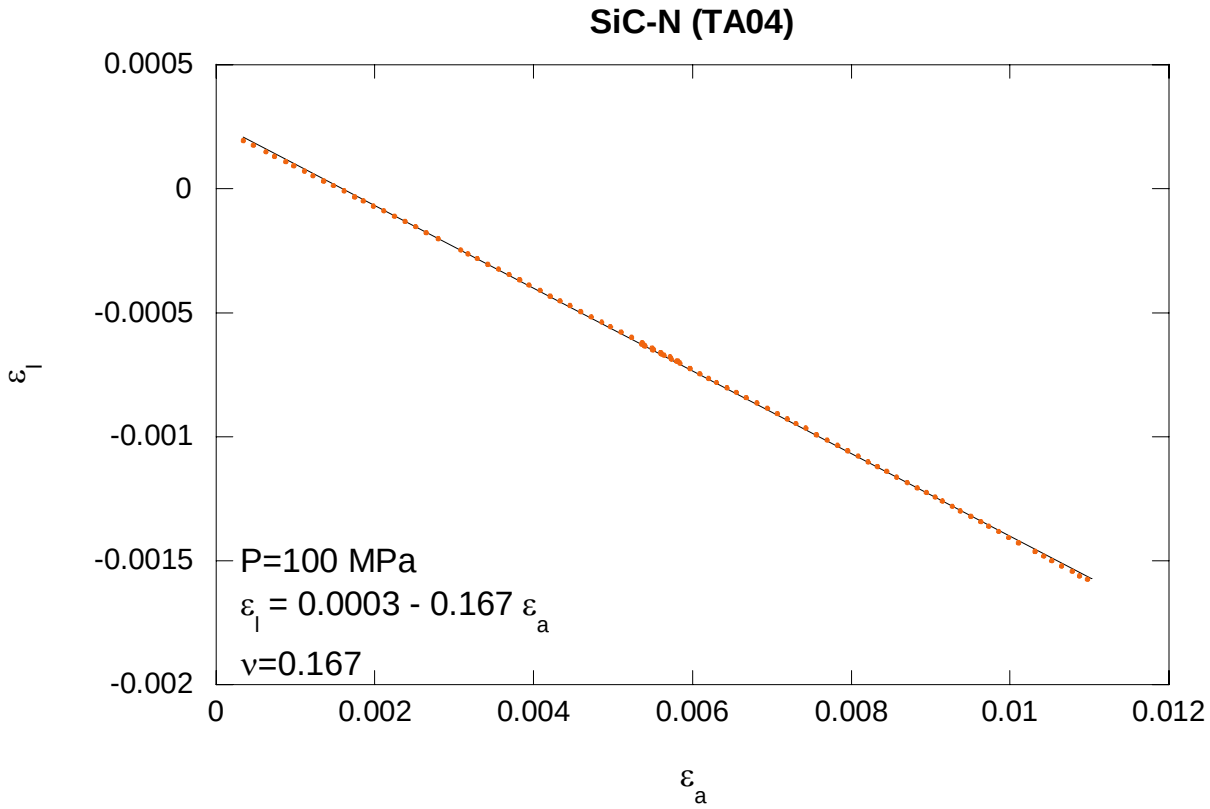
SiC-N (TA04)
0.0005
0
-0.0005
-0.001
-0.0015
-0.002
0
0.002
0.004
0.006
0.008
0.01
0.012
ε_l
ε_a
P=100 MPa
$\varepsilon_l = 0.0003 - 0.167\ \varepsilon_a$
ν=0.167

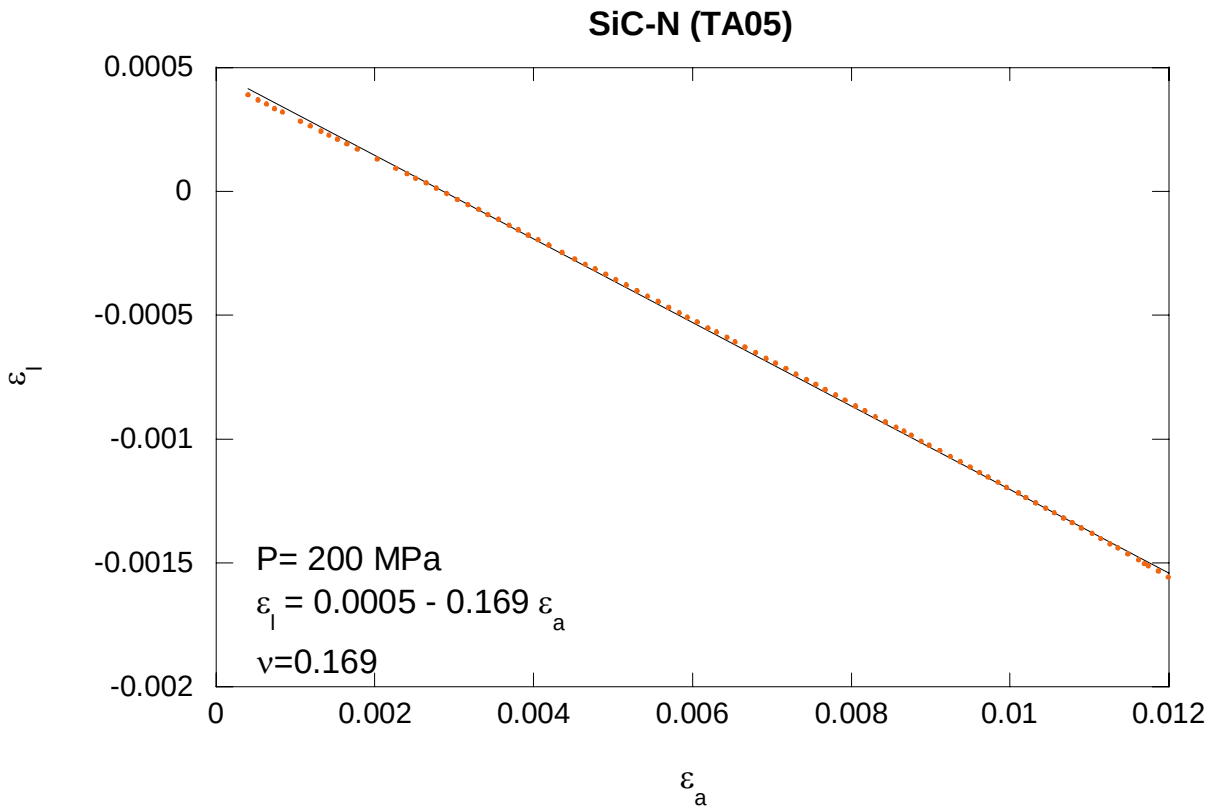
SiC-N (TA05)
0.0005
0
-0.0005
-0.001
-0.0015
-0.002
0
0.002
0.004
0.006
0.008
0.01
0.012
ε_l
ε_a
P= 200 MPa
$\varepsilon_l = 0.0005 - 0.169\ \varepsilon_a$
ν=0.169

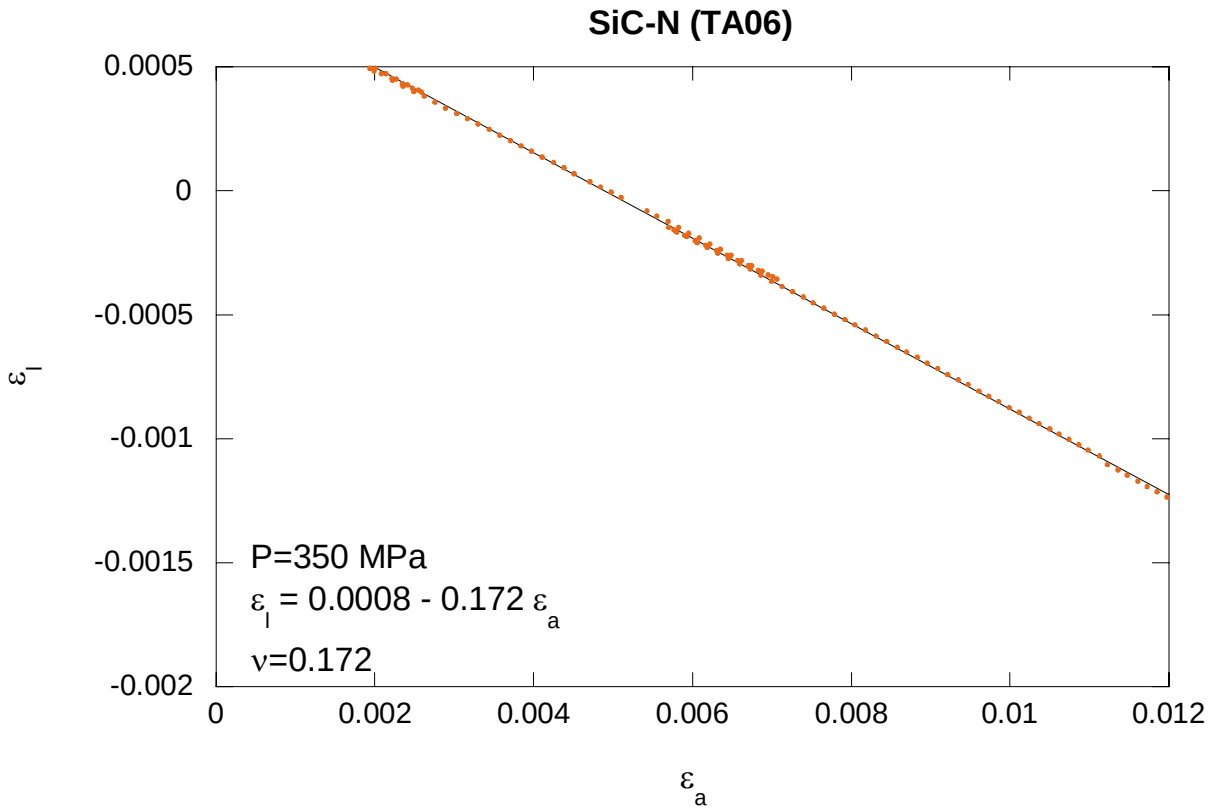
SiC-N (TA06)
0.0005
0
-0.0005
-0.001
-0.0015
-0.002
ε_l
P=350 MPa
$\varepsilon_l = 0.0008 - 0.172\ \varepsilon_a$
ν=0.172
0
0.002
0.004
0.006
0.008
0.01
0.012
ε_a

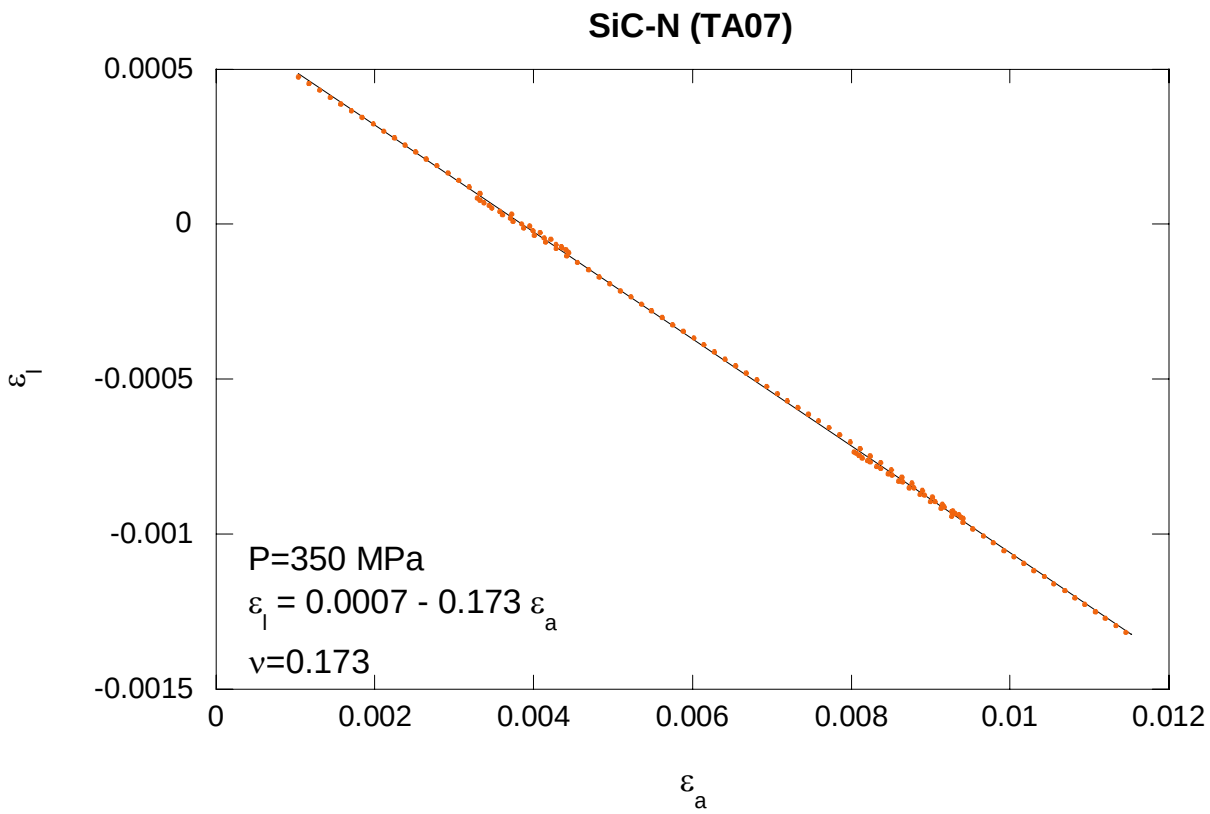
SiC-N (TA07)
0.0005
0
-0.0005
-0.001
-0.0015
ε_l
P=350 MPa
$\varepsilon_l = 0.0007 - 0.173\ \varepsilon_a$
ν=0.173
0
0.002
0.004
0.006
0.008
0.01
0.012
ε_a

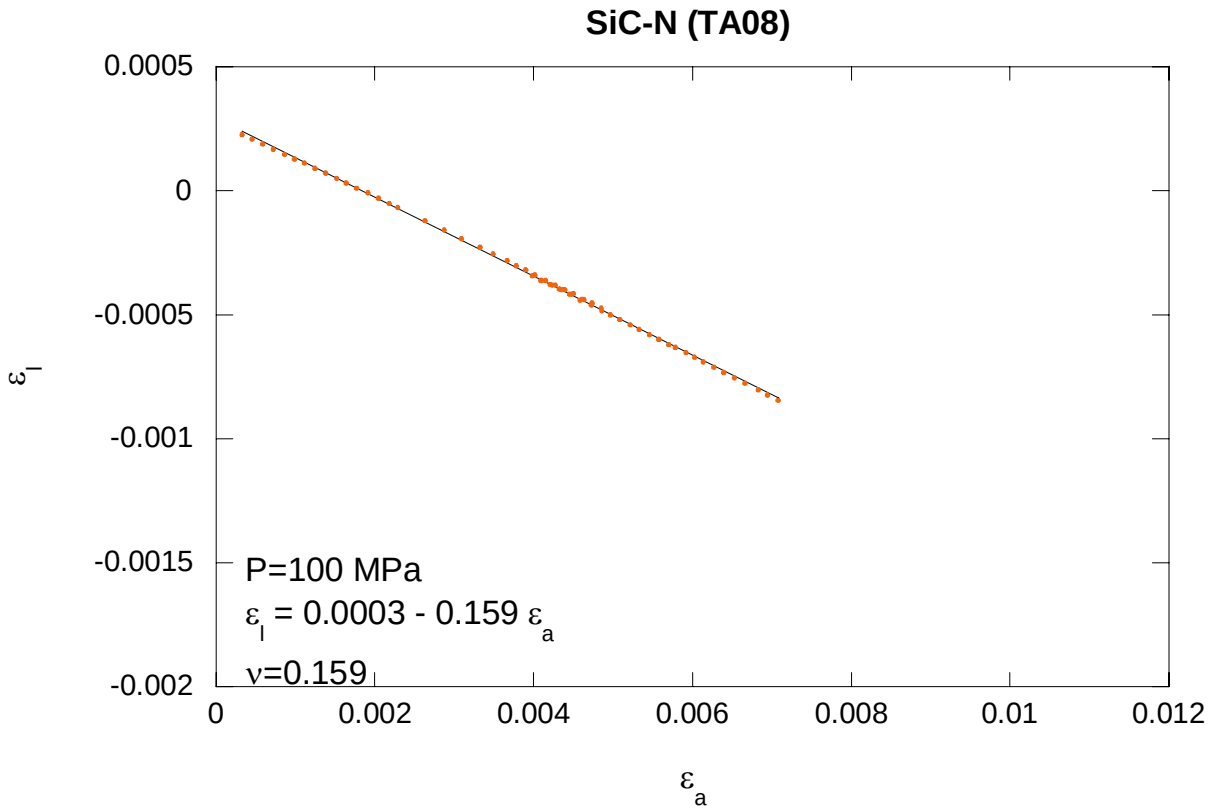
SiC-N (TA08)
0.0005
0
-0.0005
-0.001
-0.0015
-0.002
ε_l
P=100 MPa
ε_l = 0.0003 - 0.159 ε_a
ν=0.159
0
0.002
0.004
0.006
0.008
0.01
0.012
ε_a

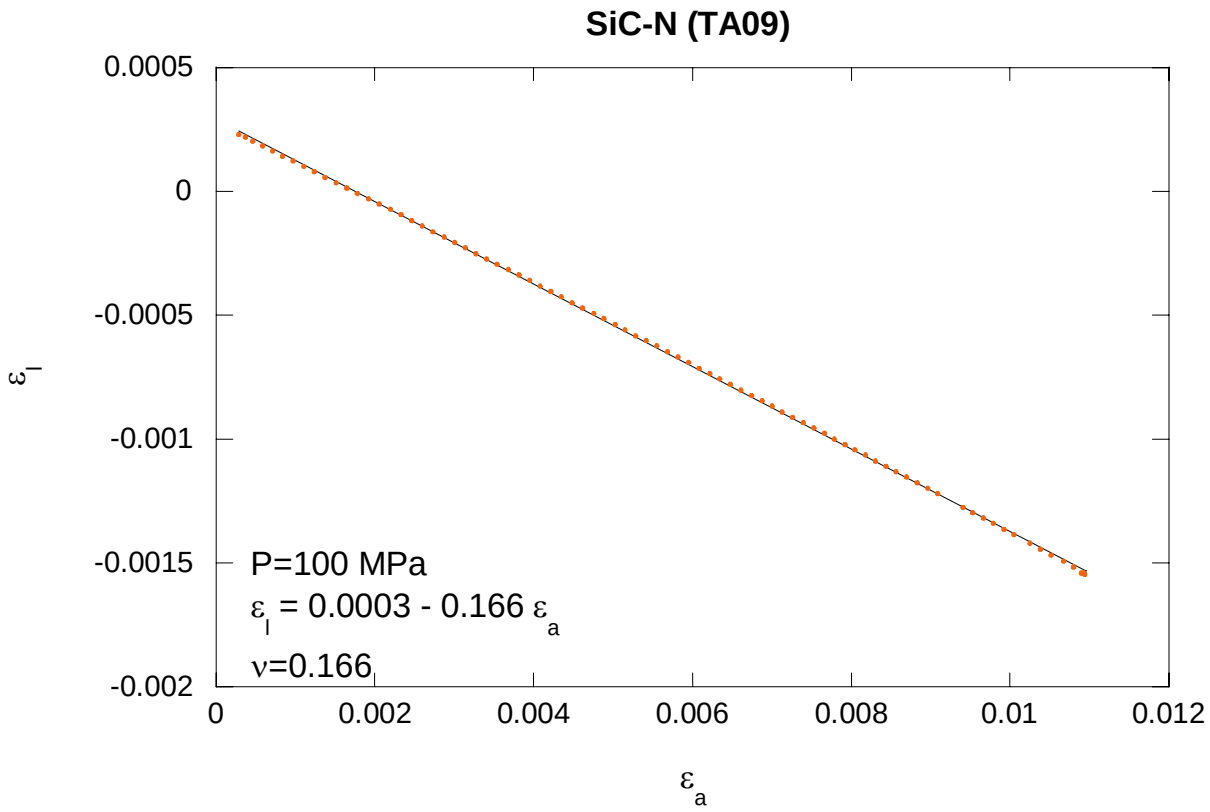
SiC-N (TA09)
0.0005
0
-0.0005
-0.001
-0.0015
-0.002
ε_l
P=100 MPa
ε_l = 0.0003 - 0.166 ε_a
ν=0.166
0
0.002
0.004
0.006
0.008
0.01
0.012
ε_a

APPENDIX D

A review of published data for SiC

Information in this appendix is taken from a memo (dated 12/14/2004) from Diane Meier to Moo Lee, entitled "Results of the data mining for SiC".

Despite the fact that many people are interested in silicon carbide (SiC) and despite the fact that the material has many useful applications, it is lacking data to determine many of its mechanical properties. This appendix presents the reader with an overview of data that has already been collected for the Cercom material, SiC-N. This appendix also includes data for Cercom SiC-B, since it is similar to SiC-N in many respects. SiC-N is a refined product of SiC-B that uses an organic binder. Table E-1 shows properties listed by Cercom for both SiC-B and SiC-N.

Table E-1. Typical properties of SiC-B and SiC-N (Cercom, 2003).

	SiC-B	SiC-N
Bulk Density (g/cm^3)	3.20	3.20
Average grain size (m)	3-5	3-5
Flexural Strength, Ksi (4-Pt MOR) MPa	70 560	85 580
Characteristic Strength (MPa)	595	600
Weibull Modulus (m)	11	17
Elastic Modulus (E) (GPa)	460	460
Poisson's Ratio (ν)	0.16	0.16
Hardness (kg/mm^2)(Knoop 0.3kg)	2450	2450
Fracture Toughness ($MPa\text{-}m^{1/2}$) (Chevron Notch)	4.4	4.7
Thermal Expansion (10^{-6}/C) (RT-1000 C)	4.5	4.5
Thermal Conductivity (W/m-K) @ RT	130	130
Electrical Resistivity (W-cm)	$>10^4$	$>10^4$

Table E-2 presents the data collected from three experiments. In each experiment, work was done to determine key properties, such as density, in addition to key mechanical properties. The table contains information for both SiC-B and SiC-N. The TARDEC report contained information for 18 different silicon carbide materials. Of the eighteen there were three separate SiC-B materials, which are included in Table E-2. The only noted differences are in the grain size and the density (Note: There are other differences between the materials, but the differences are in strength measurements and those differences are believed to be a function of the density differences).

Table E-2. Collection of data from various experiments, showing the properties of SiC.

TARDEC Technical Report, Holmquist *et al.* (1999)					Bartkowski and Spletzer (2001)		Dandekar and Bartkowski (2002)	
Description	SiC-B	SiC-B	SiC-B	SiC-N	SiC-N	SiC-B	SiC-B	SiC-N
Average Grain Size (m)	2	4	5	4	5.0	2.8		
Density (/cm^3)	3.220	3.150	3.180		3.215	3.227	3.215 ±0.002	3.22 ±0.001
Longitudinal Velocity (km/s)		12.220	12.250				12.198 ±0.026	12.262 ±0.001
Shear Velocity (km/s)		7620	7765				7.747 ±0.018	7.77 ±0.005
Bulk Velocity (km/s)		8480	8350				8.29 ±0.03	8.354 ±0.006
Young's Modulus, E (GPa)	427	433	427		448	454	448.4 ±2.1	454.0 ±0.6
Shear Modulus, G (GPa)		183	195		193	195	193 ±0.9	195 ±0.2
Bulk Modulus K (GPa)		227	223		221	225	221.1 ±1.8	225.2 ±0.3
Poisson Ratio		0.182	0.14		0.162	0.164	0.162 ±0.003	0.164 ±0.001
Compressive Strength (GPa)			3.41					
Pore Size (m)					2.3	1.9		
Pore Volume Fraction							0.002	

Hydrostatic Compression

Strössner *et al*. (1987), Aleksandrov *et al*. (1992), Bassett et *al*. (1993), and Yoshida *et al*. (1993) have reported results for hydrostatic compression of 6H-SiC. In the paper written by Dandekar (2002), it was found that 6H-Sic is manufactured by Cercom and is marketed as SiC-B, so the data for 6H-SiC has been included in this data report. Table E-3 has the bulk modulus data for 6H-SiC, as reported by Dandekar (2002). The data in Dandekar's paper comes from two separate experiments: Bassett *et al*. (1993) and Yoshida *et al*. (1993) B_0 represents the bulk modulus, B_0' is the pressure derivative of the bulk modulus and P_{max} is the maximum pressure to which the experiments were carried out (Dandekar, 2002). Bassett et *al*. (1993) and Yoshida *et al*. (1993) confined the SiC material in a mixture of sodium chloride and gold, and methanol, ethanol and water respectively, to produce a hydrostatic pressure environment in their samples (Dandekar, 2002).

Table E-3. Data from various static pressure investigations for SiC (Dandekar, 2002).

	B_0 (GPa)	B_0'	P_{max} (GPa)	Reference
6H-SiC	230 ± 4	4.0 (assumed)	68	Bassett *et al.* (1993)
6H-SiC	260 ± 9	2.9 ± 0.3	95	Yoshida *et al*. (1993)

Figure E-1 shows the mean volumetric compression of 6H-SiC from the studies completed by Bassett *et al.* (1993) and Yoshida *et al*. (1993). The pressure values were calculated at various volumetric compressions, using a series of equations not included in their report.

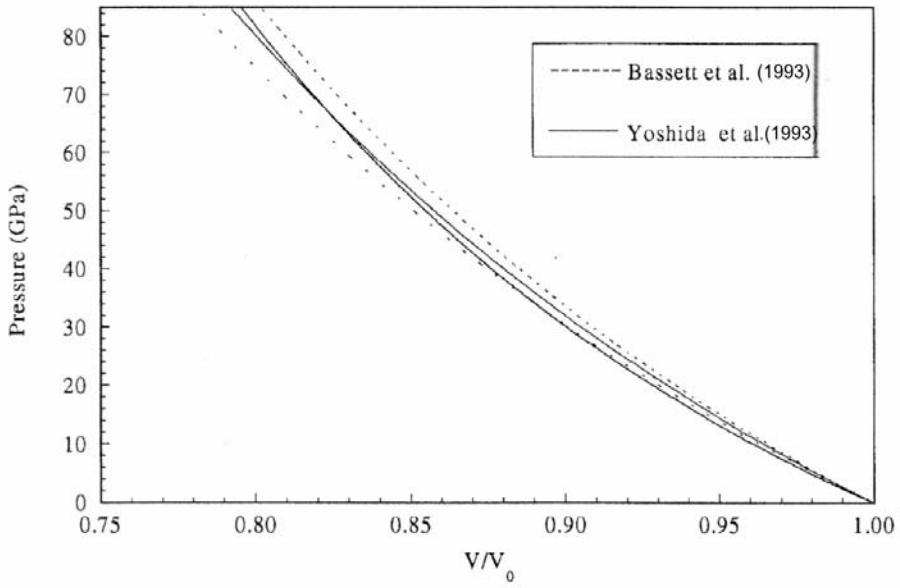

Figure E-1. Compression values of 6H-SiC from high-pressure x-ray diffraction data (Dandekar, 2002).

Hydrodynamic (Shock) compression

Sekine and Kobayashi (1997, 1998) measured the shock compression of 6H-SiC to 160 GPa, using the 6H-SiC (SiC-B) material manufactured by Cercom. The hydrodynamic compression of SiC-B is represented by the bulk modulus and the pressure derivative of the bulk modulus; this is information is summarized in Table E-4. The information in this table was reported by Dandekar (2002) and was collected from two studies completed by Sekine and Kobayashi (1997, 1998). In Table E-4, HEL represents the Hugoniot Elastic Limit.

Table E-4. Density, HEL, B_o, B_o' for 6H-SiC used in the shock compressions completed by Sekine and Kobayashi (1997, 1998).

	$_0$ (Mg/m3)	HEL (GPa)	B_0 (GPa)	B_0'	P_{max} (GPa)
6H-SiC	3.22	18.0 ± 0.7	230**	4.6	105

**Sekine and Kobayashi (1997, 1998) took this value from the work done by Bassett *et al.* (1993) for their analyses (Dandekar, 2002).
Figure E-2 shows a plot of shock compression data for various forms of SiC, generated by various investigators. Only Sekine and Kobayashi performed shock compression tests on the SiC-B material. The data points from their investigations are highlighted in red, yellow and green. In this figure, the data points denoted by HEL are at or below the HEL; PL1 indicates the inelastic deformation of SiC, and PL2 indicates the transformed phase of SiC (Dandekar, 2002). The curve in Figure E-2 represents the compression of 6H-SiC (SiC-B) obtained by using the values of bulk modulus and its pressure derivative given in Table E-4 (Dandekar, 2002).

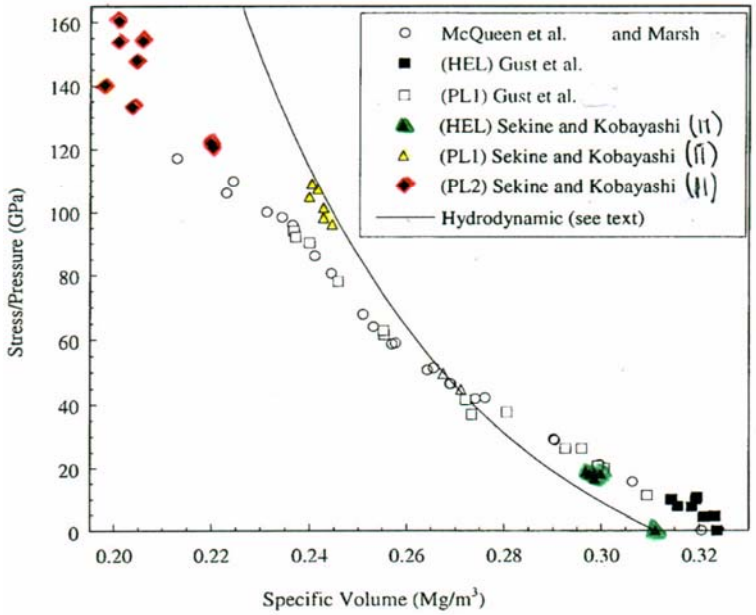

Figure E-2. Shock compression data for SiC (Dandekar, 2002).

Shear Strength

Bourne *et al.* (1997) and Feng *et al.* (1998) measured the shear strength of SiC-B under shock compression. The shock compression was measured through the simultaneous measurements of longitudinal and lateral stress. Dandekar (2002) also calculate the values of shear stress using a system of equations not included in his report. These calculated values were then compared to the values obtained by measurements done by Bourne *et al.* (1997) and Feng *et al.* (1998). The calculated and measured values are summarized in Table E-5. On the table, is defined as $((V_0/V)-1)$. There are four separate studies represented in this table: Feng *et al.* (1996, 1998), Grady and Kipp (1993) and Bourne *et al.* (1997).

Table E-5. Measured and calculated values of shear stress as reported in Dandekar (2002). Values were obtained under plane shock wave compression.

Experiment No.	Stress (GPa)				Calculated (GPa)	
	Longitudinal	Lateral	Shear		Pressure	Shear
Feng *et al*. (1998)						
1	10.20	1.84	4.18	0.0209	4.80	4.05
2	12.90	2.34	5.28	0.0264	6.12	5.09
3	15.00	3.40	5.80	0.0312	7.29	5.78
4	16.00	3.60	6.20	0.0336	7.89	6.09
5	18.80	5.10	6.85	0.0412	9.80	6.75
6	20.90	6.94	6.98	0.0479	11.53	7.03
7	24.20	10.40	6.90	0.0610	15.03	6.88
Crawford's experiments reported by Feng *et al*. (1996)						
SC-3 (a)	26.8			0.0875	22.8 ± 0.5	3.0 ± 0.4
SC-4 (a)	39.6			0.1314	36.9 ± 1.1	2.0 ± 0.8
SC-3 (b)	28.5			0.0785	20.2 ± 0.4	6.2 ± 0.3
SC-4 (b)	40.8			0.1237	34.4 ± 1.0	4.8 ± 0.8
Grady and Kipp (1993)						
CE-4	27.6			0.075	19.2 ± 0.4	6.3 ± 0.3
CE-5	36.3			0.1087	29.4 ± 0.8	5.2 ± 0.6
CE-31	48.8			0.1534	45.0 ± 1.5	2.8 ± 1.1
Bourne *et al*. (1997)						
1	16.7	3.3	6.7			
2	21.2	4.1	8.6			
3	23.4	6.7	8.4			

Plate Impact Test Data

Grady and Moody (1996) performed plate impact tests on various silicon carbide materials, including SiC-B and SiC-N. Table E-6 contains the data for four of the materials tested by Grady and Moody (1996); the SiC-B material is represented by the data for Material No. 107, which is highlighted in yellow. The SiC-N material is represented by the data for Material No. 111, which is highlighted in blue. Figure E-3 contains the velocity profiles for the three SiC-B tests found in Table E-6. The velocity profiles reflect the uniaxial strain loading and unloading behavior of the material (Holmquist *et al.* 1999).

Table E-6. Summary of experimental plate impact initial conditions and results from Grady and Moody (1996).

Silicon Carbide														
		Initial Conditions									Hugoniot Results			
		Projectile					Target							
Test Number	Material Number		Backer		Impactor		Sample		Window		Elastic Regime (HEL)		Plastic Regime	
		V (m/s)	Material	L_B (mm)	Material	L_I (mm)	Density (kg/m³)	L_S (mm)	Material	L_W (mm)	σ_z (GPa)	ρ (kg/m³)	σ_z (GPa)	ρ (kg/m³)
1415	106	1542	PF320	6.0	SiC	3.987	3177	8.939	LiF	25.4	14.8	3272	27.6	3409
1416	106	2100	PF640	6.0	SiC	3.995	3177	8.940	LiF	25.4	15.3	3276	36.5	3519
1417	106	2118	PF640	6.0	Ta	1.516	3177	8.956	LiF	25.4	14.9	3273	48.7	3658
1418	106	612	PF320	6.0	SiC	4.958	3177	9.841	LiF	25.4				
1419	106	2206	Ta	1.510	LiF	3.297	3177	4.963	LiF	25.4				
1420	107	535	PMMA	6.35	Al	0.990	3221	4.035	LiF	9.196				
1421	107	1566	PF320	8.0	SiC	4.490	3220	9.014	LiF	25.4				
1422	107	2259	PF557	8.0	SiC	4.516	3220	8.993	LiF	25.4				
1423	111	485	PF640	8.04	Mg	0.5974	3227	4.512	PMMA	24.2				
1424	111	1596	PF328	8.0	SiC	4.503	3220	9.012	LiF	25.4				
1425	111	2352	PF640	8.0	SiC	4.504	3230	8.998	LiF	25.4				
1426	112	2385	PF640	8.0	SiC	4.527	3216	8.995	LiF	25.4				
1427	112	489	PMMA	6.35	Mg	0.60	3244	4.025	LiF	9.20				
1428	112	485	PF640	8.03	Al	1.042	3226	4.527	PMMA	24.2				
1429	112	1605	PF320	8.0	SiC	4.506	3220	9.013	LiF	25.4				

Test 1415-1429: the test data is from work by Grady. Material #106 is Silicon Carbide manufactured by Eagle Picher, having a nominal initial density = 3177kg/m³. Material #107 is Silicon Carbide manufactured by Cercom having an initial density = 3150kg/m³. The above table primarily provides the initial conditions for the plate impact experiments, although the elastic and plastic stress-density states are provided when available.

Test 1415-1417: the HEL and peak Hugoniot stress and density obtained from Grady 1994, 1995; Kipp and Grady, 1989; and Grady and Wise, 1993.

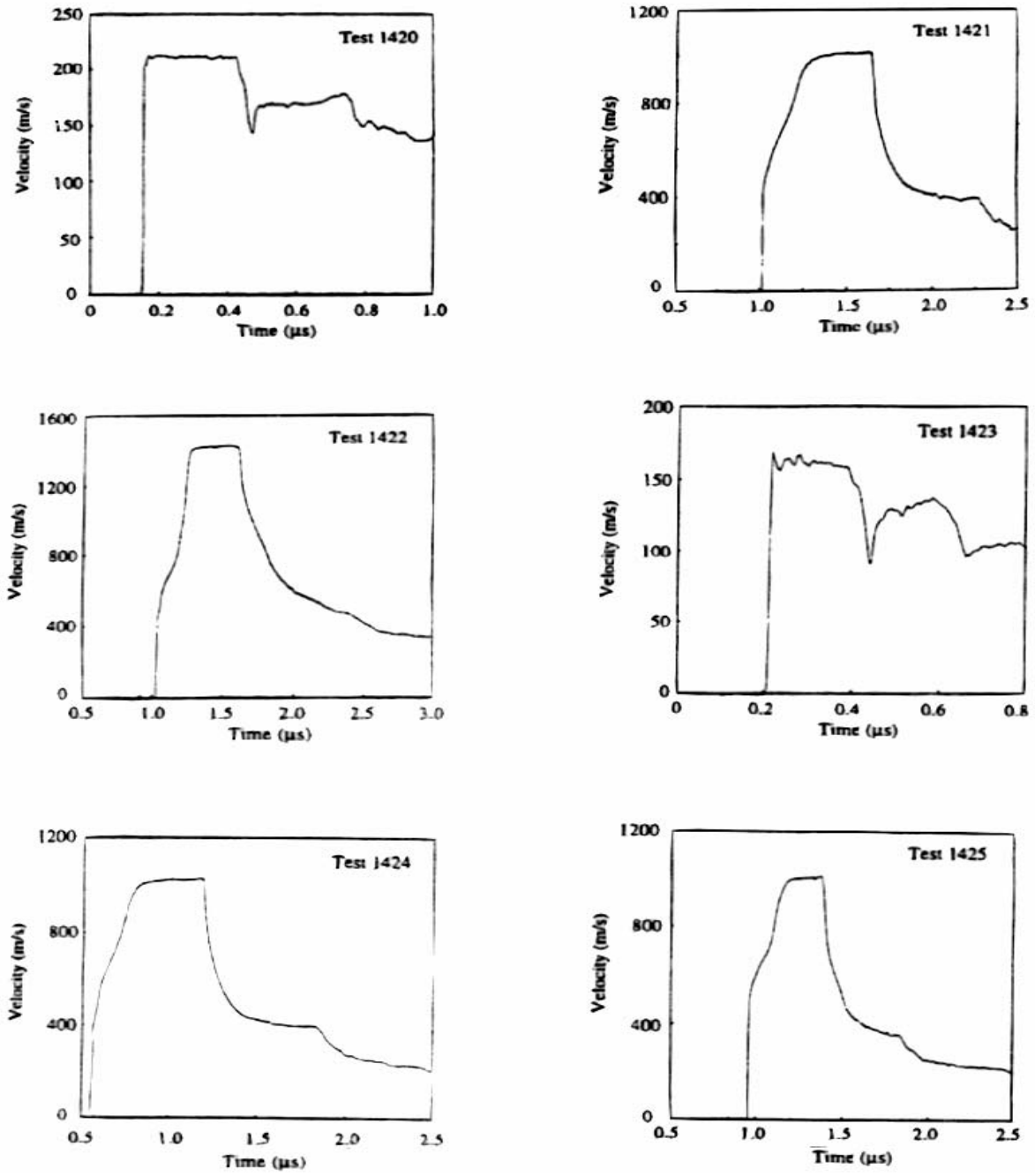

Figure E-3. Velocity profiles from Grady and Moody (1996) for tests 1420-1425.

Dandekar and Bartkowski (2001) performed spall experiments on the SiC-B and SiC-N materials. They used two experiment designs: one where the particle velocity profile was recorded at a stationary plate poly-methyl-meth-acrylate (PMMA) window interface and one where the free-surface velocity profile of the stationary plate is monitored and the velocity profiles were recorded by a 4-beam velocity interferometer system. Figure E-4 shows the velocity profiles from the experiments completed by Dandekar and Bartkowski (2001). These velocity profiles were used for the calculation of spall strengths. The results of the spall experiments for SiC-B and SiC-N are found in Tables E7-E10 and Figure E-5 shows the wave profiles for three of the spall strength experiments completed on SiC-N.

Table E-7. Results for the spall experiments for SiC-B from Dandekar and Bartkowski (2001).

Experiment	Thickness (mm)		Impact Velocity (km/s)	Pulse Width (μs)	Free-Surface Velocity (km/s)		
	Flyer	Target			Shock	Spall	Recompression
404[a]	3.890	7.950	0.6021	0.613	0.5383	0.4015	0.4272
413[a]	3.914	7.935	0.0826	0.630	0.0752	0.0243	0.0585
421[a]	3.915	7.926	0.2939	0.632	0.2725	0.1730	0.2270
423	3.934	7.957	0.1907	0.623	0.1923	0.1263	0.1925
433[a]	3.920	7.901	0.0804	0.628	0.0654	0.0125	0.0571
437	3.910	7.951	0.1330	0.636	0.1316	0.0859	0.1312
443	3.912	7.967	0.1483	0.643	0.1535	0.1073	0.1540
447	3.905	7.932	0.4956	0.613	0.5093	0.4593	0.5093
452	3.974	7.918	0.0804	0.642	0.0823	0.0307	0.0832
504	3.984	7.916	0.6130	0.633	0.6059	0.5615	0.6056
607	2.122	7.958	0.1311	0.334	0.1305	0.0872	0.1326

[a] In this experiment, a 6-mm-thick PMMA disk was bonded to the SiC target and particle velocity profile was monitored at the PMMA-SiC interface.

Table E-8. Summary of the results from the spall experiments for SiC-B from Dandekar and Bartkowski (2001).

Experiment	Impact Velocity (km/s)	Shock		Release Impedence (Gg/m^2s)	Spall Strength		
		Mass Velocity (km/s)	Stress (GPa)		1/2 Pull-Back Change (km/s)	Stress (1) (GPa)	Stress (2) (GPa)
404[a]	0.6021	0.3011	11.845	40.73	—	0.822	0.560
413[a]	0.0826	0.0413	1.625	40.04	—	0.823	0.732
421[a]	0.2939	0.1470	5.782	37.93	—	1.123	1.160
423	0.1907	0.0954	3.752	38.70	0.0330	1.294	1.299
433[a]	0.0804	0.0402	1.582	53.56	—	0.903	0.955
437	0.1330	0.0665	2.617	40.19	0.0228	0.894	0.890
443	0.1483	0.0742	2.918	36.77	0.0231	0.906	0.917
447	0.4956	0.2478	9.750	37.28	0.0250	0.980	0.982
452	0.0804	0.0402	1.582	37.57	0.0258	1.012	1.025
504	0.6130	0.3056	12.06	40.28	0.0222	0.871	—
607	0.1311	0.0656	2.57	39.6	0.0216	0.847	—

Table E-9. Summary of the results for the spall experiment for SiC-N as reported by Dandekar and Bartkowski (2001).

Experiment	Thickness (mm)		Impact Velocity (km/s)	Pulse Width (μs)	Free-Surface Velocity (km/s)		
	Flyer	Target			Shock	Spall	Recompression
519	3.987	8.009	0.1683	0.650	0.1748	0.1474	0.1711
520	3.985	7.992	0.6049	0.650	0.6062	0.5389	0.5895–0.6000
522	3.962	7.975	0.0809	0.646	0.0809	0.0352	0.0807
525	3.983	7.994	0.4014	0.650	0.3973	0.3638	0.3947
528	3.958	55.99	0.6098	0.646	0.6049	0.5383	0.6019
607	3.986	5.937	0.1311	0.713	0.1463	0.0931	0.1451
617 (Sapphire)	3.996	5.016	0.2903	0.715	0.3031	0.2681	0.3031
621	4.001	7.354	0.3912	0.653	0.4211	0.3533	0.4204
628	3.961	5.989	0.2889	0.646	0.2885	0.2478	0.2885–0.2854
636 (SiC-B)	2.108	4.008	0.1499	0.346	0.1498	0.1026	0.1509
824-2	4.022	5.983	0.3042	0.656	0.3069	0.2598	0.3071

Table E-10. Summary of the spall experiment results for SiC-N as reported by Dandekar and Bartkowski (2001).

Experiment	Impact Velocity (km/s)	Shock		Release Impedence ($Gg/m^2 \cdot s$)	Spall Strength	
		Mass Velocity (km/s)	Stress (GPa)		1/2 Pull-Back Change (km/s)	Stress (GPa)
519	0.1683	0.0842	3.330	36.73	0.0137	0.542
520	0.6049	0.3025	11.968	39.40	0.0337	1.334
522	0.0809	0.0405	1.601	39.57	0.0229	0.906
525	0.4014	0.2007	7.942	40.40	0.0168	0.665
528	0.6098	0.3049	12.065	40.22	0.0333	1.318
607 (Sapphire)	0.1311	0.0694	2.746	35.70	0.0266	1.052
617 (Sapphire)	0.2903	0.1537	6.080	30.78	0.0175	0.692
621	0.3912	0.1956	7.740	34.32	0.0339	1.341
628	0.2889	0.1445	5.716	39.68	0.0204	0.807
636 (SiC-B)	0.1499	0.0746	2.953	39.27	0.0236	0.934
824-2	0.3042	0.1521	6.019	38.88	0.0236	0.934

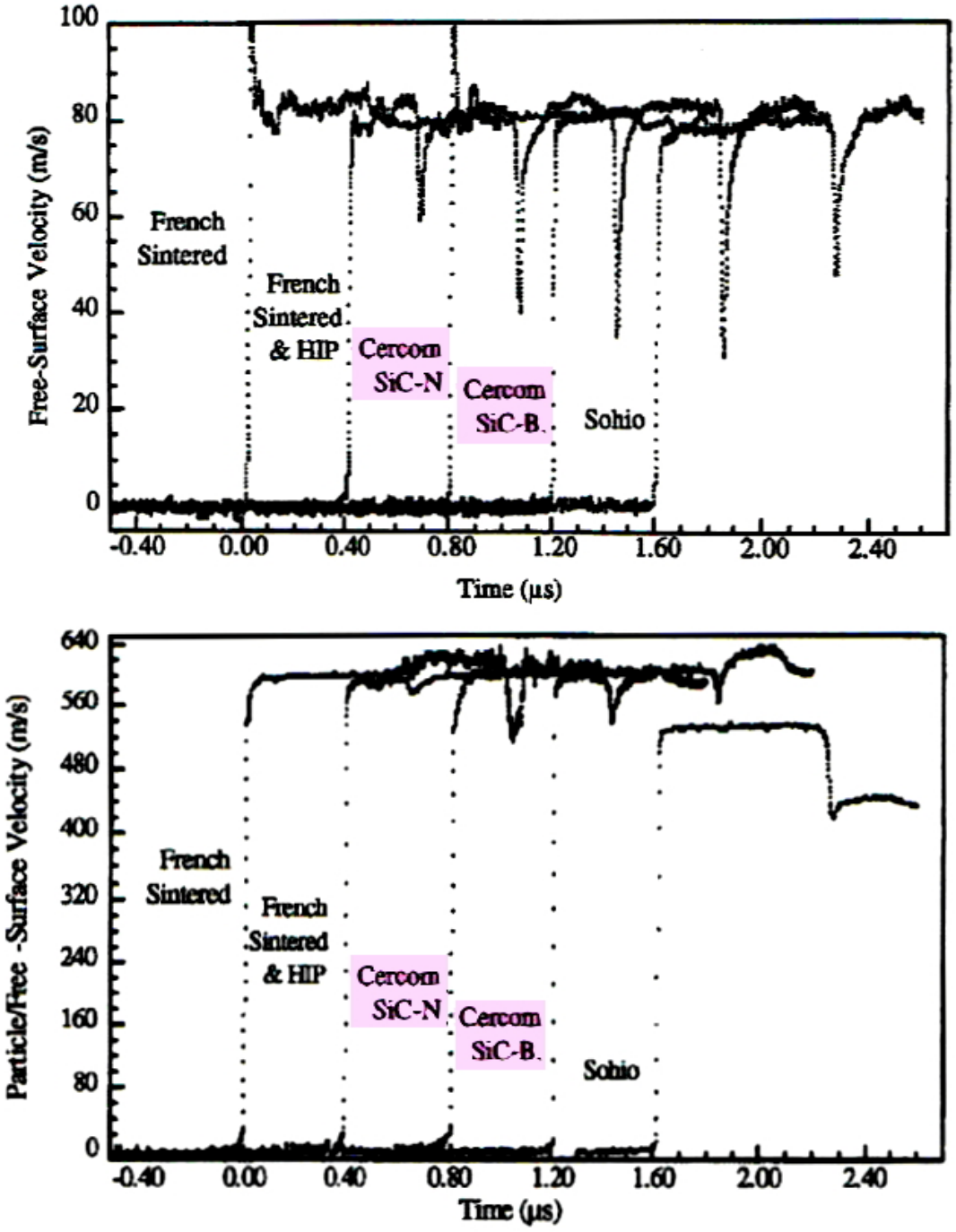

Figure E-4. Velocity profiles in SiC from Dandekar and Bartkowski (2001).

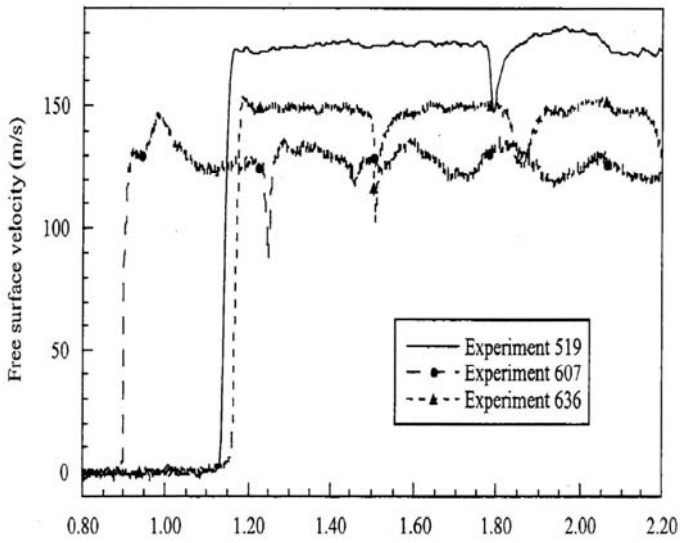

Figure E-5. Free-surface velocity profiles for SiC-N as reported by Dandekar and Bartkowski (2001).

Penetration Test Data

Table E-11 summarizes the penetration results from an experiment completed by Orphal and Franzen (1997). Information about the targets and penetrators can also be found in Table E-11. On the table, primary penetration is the depth penetrated when the penetrator is just consumed. The total penetration is the total depth penetrated when the penetration event is complete. The results of the study are also represented graphically, in Figure E-6. Material No. 4 is SiC-B, but it is a slightly different material from the SiC-B used in plate impact experiments.

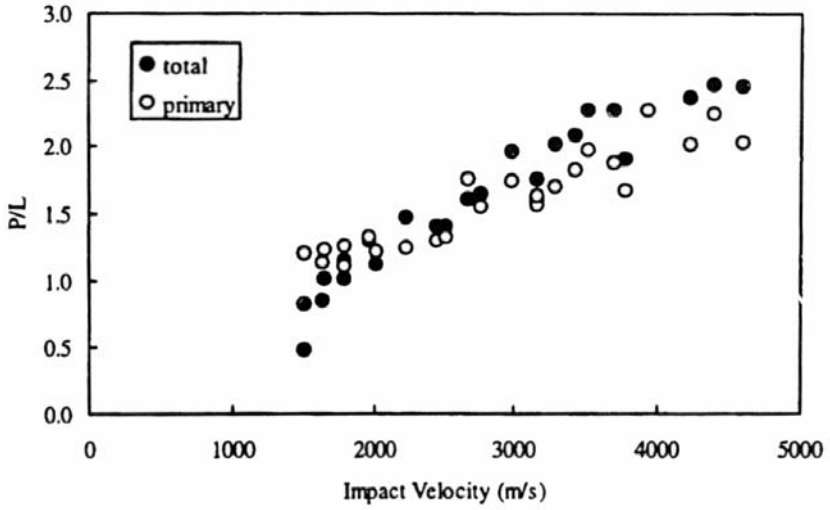

Figure E-6. Graphic representation of the penetration results. Primary penetration and Total Penetration vs. Impact Velocity for tungsten penetrators impacting confined SiC, Orphal and Franzen (1997).

Table E-11. Summary of the penetration results, Orphal and Franzen (1997).

Silicon Carbide							
Test Number	Material Number	Penetrator		Target Configuration	Impact Velocity (m/s)	$P_{primary}/L$	P_{total}/L
		D (mm)	L (mm)				
1501	104	0.762	15.24	Long	1520	1.19	0.80
1502	104	0.762	15.24	Long	1520		0.47
1503	104	0.762	15.24	Long	1650	1.12	0.83
1504	104	0.762	15.24	Long	1660	1.21	0.99
1505	104	0.762	15.24	Long	1800	1.09	0.99
1506	104	0.762	15.24	Long	1800	1.24	1.13
1507	104	0.762	15.24	Long	1980	1.31	1.28
1508	104	0.762	15.24	Long	2030	1.20	1.11
1509	104	0.762	15.24	Long	2250	1.23	1.46
1510	104	0.762	15.24	Long	2470	1.28	1.39
1511	104	0.762	15.24	Long	2530	1.31	1.39
1512	104	0.762	15.24	Long	2690	1.75	1.59
1513	104	0.762	15.24	Long	2780	1.54	1.63
1514	104	0.762	15.24	Long	3000	1.73	1.95
1515	104	0.762	15.24	Long	3170	1.56	1.59
1516	104	0.762	15.24	Long	3180	1.62	1.74
1517	104	0.762	15.24	Long	3300	1.69	2.01
1518	104	0.762	15.24	Long	3450	1.82	2.07
1519	104	0.762	15.24	Long	3540	1.96	2.26
1520	104	0.762	15.24	Long	3710	1.87	2.26
1521	104	0.762	15.24	Long	3790	1.66	1.90
1522	104	0.762	15.24	Long	3940	2.27	2.26
1523	104	0.762	11.43	Short	4240	2.01	2.36
1524	104	0.762	11.43	Short	4410	2.24	2.46
1525	104	0.762	11.43	Short	4610	2.02	2.44

Test 1501-1525: the test data is from work by Orphal and Franzen (1997). Two penetrator lengths and two target configurations were used. The penetration includes the 3.18mm cover. In some cases, at the lower velocities, the primary penetration exceeds the total penetration. This is not reality, but is a reflection of how the primary penetration is calculated. The penetration and erosion rates are determined from the x-rays. These rates are assumed to be constant and are used to determine when the penetrator is consumed, and at what depth. At the lower impact velocities the rates are not constant, thus larger primary penetration depths are calculated. A more in depth discussion of this is provided in Orphal and Franzen (1997).

Holmquist and Johnson (2002) also performed plate impact tests on the SiC-B material. Figure E-7 is a comparison of the calculated values and experimental results obtained by Holmquist and Johnson (2002) for two compressive plate impact tests and two tensile plate impact tests. The equations used for the calculations are not included in this report. The tests completed by Holmquist and Johnson involves the plate impact of a silicon carbide impactor on a silicon carbide target; in this study, the silicon carbide target is SiC-B from Cercom.

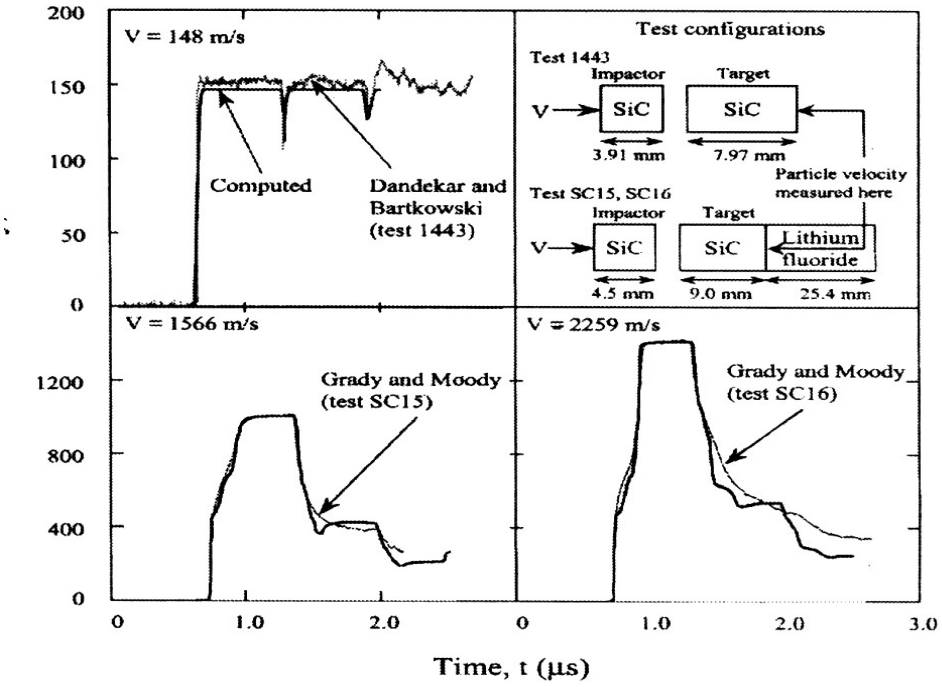

Figure E-7. A comparison of the computational and experimental results found by Holmquist and Johnson (2002).

Information in Table E-12 was taken from a report written by Pickup and Barker (2000). However, upon inspecting this report, the Pickup and Barker's source for the quasi-static compression data is unclear, since the paper only discusses the shock compression tests they performed on the SiC-B material. Pickup and Barker only studied the SiC-B material.

Table E-12. Physical properties of SiC-B as reported by Pickup and Barker (2000).

	Density (kg/m^3)	E (GPa)	G (GPa)	ν	Mean Grain Diameter	Compressive strength (GPa)	
						Quasi-static ($\dot{\varepsilon} \sim 10^{-3}/s$)	Split Hopkinson Bar ($\dot{\varepsilon} \sim 10^{3}/s$)
SiC-B	3238	456	196	0.16	2.90±2.4	5.15±0.25	8.17±0.16

Very little shock or quasistatic data are available for SiC-N. Relative to SiC-N, the SiC-B ceramic has been studied more extensively. Some of the papers cited in this appendix refer to other publications that purportedly include quasi-static testing data for SiC-B; however, in most cases, these papers only had additional information on plate impact testing. Hence, greater attention to quasistatic testing appears to be needed for both SiC-N and SiC-B. The SiC data summarized in this appendix have been drawn from existing journal publications and online research databases. A fair amount of recent work has been done on both SiC-B and SiC-N, but that the information is not yet available in the open literature.

APPENDIX E

List of Data and Supplemental Files Archived in Webfileshare System for SiC-N

List of files archived in the WEBFILESHARE system (https://wfsprod01.sandia.gov).

Folder Name	File Name	Description
/TARGET/SICN	SIC-N-SAND.doc	This SAND report
/TARGET/SICN	SIC-N-master.xls	Master data file consists of the following four worksheets: **Summary**: SiC-N constitutive testing results **Test Se-up**: Pictures of test set-up and specimen assembly **Uniaxial Compression**: Uniaxial compression test data for SICN-UC01, 02, and 03 consisting of time, axial stress, lateral strain, and volumetric strain **Triaxial Compression**: Triaxial compression test data for SICN-TA01, 02, 03, 04, 05, 06, 07, 08, and 09 consisting of time, confining pressure, axial stress, lateral strain, and volumetric strain
/TARGET/SICN	SIC-N-data-sheet.zip	Laboratory data sheets for the following tests: SICN-UC01, UC02, UC03, TA01, TA02, TA03, TA04, TA05, TA06, TA07, TA08, and TA09.

References

Aleksandrov, I. V., Goncharov, A. F., Yakovenko, E. V., and S. M. Stishov, High-Pressure Research: Application to Earth and Planetary Sciences, Edited by Y. Syono and M. H. Manghanani, TERRAPUB/American Geophysical Union, Tokyo, p.409, 1992.

ASTM D2938-95, Unconfined Compressive Strength of Intact Rock Core Specimens, American Society for Testing and Materials, 2002.

ASTM D4543, Standard Practice for Preparing Rock Core Specimens and Determining Dimensional and Shape Tolerances, American Society for Testing and Materials, 1995.

Bartkowski, P. and S. Spletzer, Porosity Effects on the Elastic Constants of Five Varieties of Silicon Carbide Ceramics, ARL-TR-2606, U.S. Army Research Laboratory, Aberdeen Proving Ground, MD, 2001.

Bassett, W. A., Weathers, M. S. and T. C. Wu, Compressibility of SiC up to 68.4 GPa, *Journal of Applied Physics*, Vol. 74, p.3824, 1993.

Bourne, N., Millett, J. and I. Pickup, Delayed Failure in Shocked Silicon Carbide, *Journal of Applied Physics*, Vol. 81, p.6019, 1997.

Budge, K. G. and J. S. Peery, RHALE: A MMALE Shock Physics Code Written in C++, International Journal of Impact Engineering, Vol. 14, pp. 107-120, 1993.

Cercom, Inc., PAD Silicon Carbide, Thomas Publishing Company. Vista, CA, 2003.

Dandekar, D. P., A Survey of Compression Studies of Silicon Carbide (SiC), ARL-TR-2695, U.S. Army Research Laboratory, Aberdeen Proving Ground, MD, 2002.

Dandekar, D. P. and P. T. Bartkowski, Tensile Strengths of Silicon Carbide under Shock Loading, ARL-TR-2430, U.S. Army Research Laboratory, Aberdeen Proving Ground, MD, 2001.

Feng, R., Raiser, G. F. and Y. M. Gupta, Shock Response of Polycrystalline Silicon Carbide Undergoing Inelastic Deformation, *Journal of Applied Physics*, Vol. 79(3), p. 1378, 1996.

Feng, R., Raiser, G. F. and Y. M. Gupta, Material Strength and Inelastic Deformation of Silicon Carbide Under Shock Wave Compression, *Journal of Applied Physics*, Vol. 83(1), p.79, 1998.

Fossum, A.F. and R. M. Brannon, The Sandia GeoModel: Theory and User's Guide. Sandia Report SAND2004-3226, 2004.

Fossum, A.F., Senseny P.E., Pfeifle T.W. and K.D. Mellegard, Experimental Determination of Probability Distributions for Parameters of a Salem Limestone Cap Plasticity Model, Mechanics of Materials, Vol. 21, pp. 119-137, 1995.

Furnish, M. D., Chhabildas, L. C. and R. S. Hixon, Shock Compression of Condensed Matter--1999, Parts 1 and 2. *AIP Conference Proceedings 505*, p.573, American Institute of Physics, New York, 2000.

Grady, D.E, Shock-Wave Strength Properties of Boron Carbide and Silicon Carbide, Journal De Physique IV, Colloque C8, Vol. 4, pp. 385-391, 1994.

Grady, D.E, Dynamic Properties of Ceramic Materials, Sandia Report No. SAND94-3266, Sandia National Laboratories, Albuquerque, NM, 1995.

Grady, D.E. and M. E. Kipp, Shock Compression Properties of Silicon Carbide, Sandia Report No. SAND92-1832, Sandia National Laboratories, Albuquerque, NM, 1993.

Grady D. E. and J. Lipkin, Fragmentation of Solids under Impulsive Stress Loading, Geophysical Research Letters, Vol. 7, pp. 255, 1980.

Grady, D.E. and R.L. Moody, Shock Compression Profiles in Ceramics, Sandia Report No. SAND96-0551, Sandia National Laboratories, Albuquerque, NM, 1996.

Grady D. E. and J. L. Wise, Dynamic Properties of Ceramic Materials, Sandia Report No. SAND93-0610, Sandia National Laboratories, Albuquerque, NM, 1993.

Hardy, R., Event Triggered Data Acquisition in the Rock Mechanics Laboratory, Sandia Report SAND93-0256, UC-403, Sandia National Laboratories, Albuquerque NM, 1993.

Holmquist, T.J. and G.R. Johnson, Response of Silicon Carbide to High Velocity Impact, *Journal of Applied Physics*. Vol. 91, no. 9, p.5858, 2002.

Holmquist, T. J., Rajendran, A. M., Templeton, D. W., and K. D. Bishnoi, A Ceramics Armor Material Database, TARDEC Technical Report. January, 1999.

Kipp, M. E. and D. E. Grady, Shock Compression and Release in High-Strength Ceramics, Sandia Report No. SAND89-1461, Sandia National Laboratories, Albuquerque, NM, 1989.

Orphal, D. L. and R. R. Franzen, Penetration of Confined Silicon Carbide Targets by Tungsten Long Rods at Impact Velocities From 1.5 to 4.6 km/s, International Journal of Impact Engineering. Vol. 19, No. 1, p.1, 1997.

Pickup, I. M. and A. K. Barker, Deviatoric Strength of Silicon Carbide Subject to Shock, *Shock Compression of Condensed Matter-1999*, edited by M. D. Furnish, L. C. Chhabildas, and R. S. Hixson, American Institute of Physics, 2000.

Sandler, I. S. and D. Rubin, An Algorithm and a Modular Subroutine for the Cap Model, Int. J. Numer. and Anal. Mech. Geomech., Vol. 3, pp. 173-186, 1979.

Sekine, T. and T. Kobayashi. Shock compression of 6H polytype SiC to 160 GPa, *Physical Review B.* Vol. 55, p.8034, 1997.

Sekine T. and T. Kobayashi. *Shock Compression of Condensed Matter-1997,* Edited by S.C. Schmidt, D. P. Dandekar, and J.W. Forbes, New York: American Institute of Physics, p.141, 1998.

Strössner, K., Cardona, M. and W. J. Choyke. High pressure X-ray investigations on 3C-SiC, *Solid State Communications*. Vol. 63, p. 113, 1987.

Summers, R. M., Peery, J. S., Wong, M. W., Hertel, E. S. Jr., Trucano, T. G. and L. C. Chhabildas, Recent Progress in ALEGRA Development and Application to Ballistic Impacts, International Journal of Impact Engineering, Vol. 20, pp. 779-788, 1997.

Vogler, T. J., Reinhart, W. D., Chhabildas, L. C. and D. P. Dandekar, Hugoniot and Strength Behavior of Silicon Carbide, Journal of Applied Physics (submitted), 2004.

Wang, H. and K. T. Ramesh, Dynamic Strength and Fragmentation of Hot-pressed Silicon Carbide Under Uniaxial Compression, Acta Materialia, Vol. 52, pp. 355-367, 2004.

Wong, M. K., Weatherby, J. R., Turner, C. D., Robinson, A. C., Haill, T. A., and D. E. Carroll, Physics Applications in the ALEGRA Framework, First MIT Conference on Computational Fluid and Solid Mechanics, June, 2001.

Yoshida, M. A., Ueno, A. M., Takemura, K., and O. Shimomura. Pressure-Induced Phase Transition in SiC, *Physical Review B.* Vol. 48, p.10587, 1993.

DISTRIBUTION

External:

1 Advanced Materials Laboratoy
National Institute for Materials Science
Attn: Toshimori Sekine
1-1 Namiki, Tsukuba, 305-0044
JAPAN

1 Applied Research Associates, Inc
Attn: D. E. Grady
4300 San Mateo Blvd. NE, Suite A-220
Albuquerque, NM 87110

1 Brown University
Division of Engineering
Attn: R. Clifton
L.B. Freund
Providence, RI 02912

1 William Bruchey
509 Jacob Tome Highway
Port Deposit, MD 21904-1763

4 California Institute of Technology
Graduate Aeronautical Laboratories
Associate Professor of Aeronautics
Attn: J. E. Shepherd
G. Ravichandran
N. Lapusto
A. Rosakis
MS 105-50
Pasadena, CA 91125

1 California Institute of Technology
Seismological Laboratory 252-21
Attn: Thomas J.Ahrens
Pasadena, CA 91125

2 Cavendish Laboratory
Physics and Chemistry of Solids
Attn: J.E. Field
W.G. Proud
Madingley Road
Cambridge CB3 0HE
UNITED KINGDOM

1 CERCOM, Inc.
Attn: R. Palicka
1960 Watson Way
P. O. Box 70
Vista, CA 92083

1 CIA/OSWR
Attn: John Walton
Washington, DC 20505

1 Colorado School of Mines
Metallurgical and Materials Engineering Department
Attn: Ivar E. Reimanis
Golden, CO 80401

1 Dominca
Attn: Nancy Winfree
12111 Ranchitos Rd NE
Albuquerque, NM 87122

1 Georgia Institue of Technology
School of Materials Science & Engineering
Attn: Naresh Thadhani
Atlanta, GA 30332-0245

1 Michael Greenfield
AMSRD-ARL-WM-TD
Aberdeen Proving Ground
Maryland, 21005-5069

1 International Research Associates
Attn: Dennis L. Orphal
4450 Black Ave., Suite E
Pleasanton, CA 94566

1 Kerley Technical Services
Attn: Gerald I. Kerley, Consultant
P.O. Box 709

Appomattox, VA 24522-0709

1 US Army Research Laboratory
AMSRD-ARL-WM-TA
Attn: Brian Leavy
Aberdeen Proving Ground, MD 21005- 5066

1 NASA Langley Research Center
Attn: Scott A. Hill
Mail Stop 431
Hampton, VA 23681-0001

2 Network Computing Services, Inc.
AHPCRC
Attn: G. R. Johnson
T. Holmquist
1200 Washington Avenue South
Minneapolis, MN 55415

1 US Army Research Laboratory
AMSRD-ARL-WM-TA
Attn: Dr. Michael J. Normandia
Aberdeen Proving Ground, MD 21005

1 RAFAEL
Ballistics Center
Attn: Zvi Rosenberg
P.O. Box 2250
Haifa
ISRAEL

1 Johns Hopkins University
Dept. of Mechanical Engineering
Attn: K. T. Ramesh
Latrobe Hall, Room #1
Baltimore, MD 21218

1 PM
Combat SysteMS
Attn: SFAE-GCS-CS (John Rowe)
65011 East Eleven Mile Road
Warren, MI 48397-5000

1 Royal Military College of Science
Cranefield University
Attn: Prof. N. Bourne

Shrivenham, Swindon
SN6 XLA
UNITED KINGDOM

1 Scott E. Schoenfeld
Chief, Impact Physics Branch
AMSRD-ARL-WM-TD
Aberdeen Proving Ground, MD 21005-5069

1 Shock Wave and Condensed Matter
Research Center
Attn: T. Mashimo
Kumamoto University
Kumamoto 860-8555
JAPAN

1 Bob Skaggs Consultant
79 County Rd. 117 South
Santa Fe, NM 87501

3 Southwest Research Institute
Attn: C. E. Anderson
J. Lankford
J. Walker
P. O. Drawer 28510
San Antonio, TX 78228-0510

1 Computational Mechanics Branch
Munitions Directorate
Attn: Dr. Yen Tu, P.E.
101 W. Eglin Blvd., Ste 337
Eglin AFB, FL 32542-6810

28 U.S. Army Research Laboratory
Weapons Technology Directorate
AMSRL-WT
Attn: W. J. Bruchey
G. Bulmash
D. Dandekar
J. Dehn
G. Filbey, Jr.
K. Frank
G. Gazonas
W. Gillich
W. Gooch
F. Gregory

D. Gupta
C. Hubbard
K. Kimsey
P. Kingman
J. LaSalvia
R. Lottero
J. McCauley
H. W. Meyer
M. Normandia
A. Prakash
G. Randers-Pehrson
E. Rapacki
D. Scheffler
M. Scheidler
S. Schoenfeld
S. Segletes
J. Starkenberg
T. Wright
P.O. Box 334, Main Station
Aberdeen Proving Ground, MD 21005-5066

3 U.S. Army Research Office
Attn: A. M. Rajendran,
J. A. Bailey
K. Iyer
P. O. Box 12211
Research Triangle Park, NC 27709

3 U.S. Army TARDEC
AMSRD-TAR-R, MS 263
Attn: D. P. Templeton
L. P. Franks
K. D. Bishnoi
Warren, MI 48397-5000

1 U.S. Army TACOM, AMSTA-CS-P
Attn: T. J. Holmquist
6501 E. 11 Mile Rd.
Warren, MI 48397-5000

3 Univ. of Calif. at San Diego
Dept. of Applied Mech. & Eng. Sciences
Attn: M. Meyer
S. Nemat-Nasser
V. Nesterenko
La Jolla, CA 92093

3 The University of Texas at Austin
Institute for Advanced Technology
Attn: S. J. Bless
H. Fair
D. Littlefield
3925 W. Braker Lane, Suite 400
Austin, TX 78759

1 Structure Ceramics Group
Div of Metals and Ceramics
Oak Ridge National Laboratory
Attn: Hong Wang, Post-doc research fellow
P.O. Box 2008, MS 6068
Oak Ridge, TN 37830

1 US Army Research Laboratory
AMSRL-WM-T
Attn: T. W. Wright
4600 Deer Creek Loop
Aberdeen Proving Ground
MD 21005-5069

2 Washington State University
Institute for Shock Physics
Attn: Y. M. Gupta
J. R. Asay
Box 642816
Pullman, WA 99164-2816

Internal: Sandia National Laboratories

1	MS0316	P. Yarrington, 9230
1	MS0321	W. J. Camp, 9200
1	MS0370	M. E. Kipp, 9232
1	MS0372	J. Jung, 9127
1	MS0376	P. A. Taylor, 9232
1	MS0376	R. M. Summers, 9232
1	MS0376	S. A. Silling, 9232
1	MS0376	T. Voth, 9231
1	MS0380	S. W. Key, 9142
1	MS0521	S. T. Montgomery, 2561
1	MS0701	J. A. Merson, 6110
1	MS0701	P. B. Davies, 6100
2	MS0731	823/Library, 6850

1	MS0751	A. F. Fossum, 6117
1	MS0751	D. J. Holcomb, 6117
1	MS0751	D. R. Bronowski, 6117
1	MS0751	E. O. Strack, 6117
1	MS0751	L. S. Costin, 6117
5	MS0751	M. Y. Lee, 6117
5	MS0751	R. M. Brannon, 6117
1	MS0751	S. R. Sobolik, 6117
1	MS0751	T. Pfeifle, 6117
1	MS0751	W. A. Olsson, 6117
1	MS0834	J. E. Johannes, 9114
1	MS0836	E. S. Hertel, 9116
1	MS0847	W. W. Attaway, 9134
1	MS0889	J. S. Glass, 1843
1	MS0893	J. Pott, 9123
1	MS0893	J. V. Cox, 9123
1	MS0893	W. M. Scherzinger, 9123
2	MS0899	Technical Library, 9616
1	MS1031	J. H. Hofer, 6117
1	MS1089	F. B. Nimick, 6101
1	MS1160	T. L. Warren, 15412
1	MS1168	C. A. Hall, 1646
1	MS1181	L. C. Chhabildas, 1647
1	MS1181	T. J. Vogler, 1647
1	MS1181	W. D. Reinhart, 1647
1	MS1395	B. Y. Park, 6821
1	MS9018	Central Technical Files, 8945-1
1	MS9161	E. P. Chen, 8763
1	MS9201	E. L. Hoffman, 9519